

Modelling, Analysis and Simulation of Multifrequency Induction Hardening

vorgelegt von
Herrn Dipl.-Math. Thomas Petzold
aus Königs-Wusterhausen

Von der Fakultät II - Mathematik und Naturwissenschaften
der Technischen Universität Berlin
zur Erlangung des akademischen Grades
Doktor der Naturwissenschaften
(Dr. rer. nat.)

genehmigte Dissertation

Promotionsausschuss:

Vorsitzender: Prof. Dr. Wolfgang König
Gutachter: Prof. Dr. Dietmar Hömberg
Gutachter: Prof. Dr. Alfred Schmidt

Tag der wissenschaftlichen Aussprache: 19.05.2014

Berlin 2014
D 83

Impressum:

Copyright: © 2014 Thomas Petzold

Verlag: epubli GmbH, Berlin, www.epubli.de

Zugl.: Berlin, Technische Universität, Dissertation, 2014

ISBN 978-3-7375-0087-6

Abstract

For nearly all workpieces made of steel a surface heat treatment to raise the hardness and the wear resistance is indispensable. A classic method for the heat treatment is induction hardening, where the heating is done by electromagnetic fields. Due to the induced eddy currents and the skin effect, the necessary heat to produce the high temperature phase austenite is generated directly in the workpiece. During the subsequent quenching, martensite forms in the boundary layer, which is characterized by its high hardness. The recently developed concept of multifrequency induction hardening uses two superimposed alternating currents with different frequencies to generate a hardening profile following the contour. This method is well suited to harden complex shaped workpieces such as gears, where the coupling distance to the inductor varies. The determination of optimal process parameters requires a lot of experience and validation by time-consuming and costly experiments. Therefore, there is a huge demand for numerical simulations of multifrequency induction hardening.

The present work describes the modelling and the simulation of inductive heating of workpieces made of steel using the multifrequency concept. The model consists of a coupled system of partial and ordinary differential equations to determine the temperature distribution in the workpiece, the electromagnetic fields as the source of the Joule heat and the distribution of the high temperature phase austenite, which provides information about the resulting hardening pattern. Nonlinearities resulting from temperature dependent material parameters and a magnetic permeability that depends on the magnetic field itself are of great importance for the performance of the simulation. The coupled PDE-system is solved by the finite element method, whereby the electromagnetic subproblem is discretized by curl-conforming edge elements. Since due to the skin effect, the boundary layer of the workpiece must be resolved very accurately, the grid is generated adaptively using residual based error estimators. With respect to the time discretization, the problem represents a multi scale problem. To obtain a solution of the system, the equations are decoupled by averaging methods and then solved on the respective time scales.

For a reduced model, where the material parameters depend on the phase fraction of austenite but not on the temperature, the existence of a unique weak solution is established.

The developed algorithms are tested and verified for the example of discs with varying diameters. A comparison with experimentally determined surface temperatures and case depths shows very good correspondence. Further computations for gear geometries are compared to experimental results. For gears hardened with the multifrequency concept, a very good correspondence between computed phase fractions and experimentally determined hardening profiles could be observed for cross section cuts as well as for longitudinal cuts through the tip and the root of a tooth. Concluding the results, the developed software is well suited to predict the expected hardening profile.

Zusammenfassung

Für nahezu alle Bauteile aus Stahl ist eine Oberflächenbehandlung zur Erhöhung der Härte und der Verschleißfestigkeit unerlässlich. Als klassisches Verfahren erfolgt beim Induktionshärten die Wärmebehandlung mittels elektromagnetischer Felder. Diese erzeugen aufgrund der induzierten Wirbelströme und des Skin-Effekts die zur Bildung von Austenit benötigte Wärme direkt im Bauteil. Im anschließenden Abschreckprozess bildet sich in der Randschicht Martensit, welcher sich durch seine hohe Festigkeit auszeichnet. Beim relativ neuen Verfahren des Mehrfrequenz-Induktionshärtens erzeugen Ströme mit unterschiedlichen Frequenzanteilen ein kontourtreues Härtebild. Dieses Verfahren eignet sich sehr gut für komplexe Bauteilgeometrien wie z. B. Zahnräder, bei denen der Kopplungsabstand zum Induktor variiert. Die Bestimmung optimaler Prozessparameter erfordert viel Erfahrung und Validierung mittels zeit- und kostenintensiver Experimente. Daher besteht großes Interesse an numerischer Simulation des Mehrfrequenz-Induktionshärtens.

Die vorliegende Arbeit beschreibt die Modellierung und die Simulation der induktiven Erwärmung von Bauteilen aus Stahl mit dem Mehrfrequenzverfahren. Das Modell besteht aus einem gekoppelten System von partiellen und gewöhnlichen Differentialgleichungen zur Bestimmung der Temperaturverteilung im Werkstück, der elektromagnetischen Felder als Ursache der Erwärmung sowie der Phasenverteilung der Hochtemperaturphase Austenit, welche Aufschluss über das zu erwartende Härtebild gibt. Dabei werden Nichtlinearitäten aufgrund von temperaturabhängigen Materialparametern sowie einer vom Magnetfeld selbst abhängigen magnetischen Permeabilität berücksichtigt. Die Lösung des gekoppelten DGL-Systems erfolgt mit der Methode der Finiten Elemente, wobei für das elektromagnetische Teilproblem curl-konforme Kantenelemente verwendet werden. Da aufgrund des Skin-Effekts die Randschicht des Werkstücks sehr fein aufzulösen ist, erfolgt eine adaptive Gittergenerierung mittels residualbasierten Fehlerschätzern. Bezüglich der Zeitdiskretisierung stellt das Problem ein Mehrskalenproblem dar. Zur Lösung des PDE-Systems werden die Gleichungen durch Mittelungsverfahren entkoppelt und auf der jeweiligen Zeitskala gelöst.

Für ein reduziertes Modell, bei dem die Materialparameter nur vom Phasenanteil, nicht aber von der Temperatur abhängig sind, werden Aussagen zur Existenz einer eindeutigen schwachen Lösung hergeleitet.

Die entwickelten Algorithmen werden anhand von Scheiben mit verschiedenen Durchmessern getestet und verifiziert. Ein Vergleich mit experimentell ermittelten Oberflächentemperaturen und Einhärtetiefen zeigt sehr gute Übereinstimmung. Weitere Rechnungen für Zahnradgeometrien werden mit experimentellen Ergebnissen verglichen. Auch hier zeigt sich eine sehr gute Übereinstimmung der berechneten Phasenverteilungen mit den experimentell ermittelten Härtebildern sowohl im Querschliff als auch in Längsschliffen in Zahnkopf und Zahnfuß für im Mehrfrequenzverfahren gehärtete Zahnräder. Damit eignet sich die entwickelte Software sehr gut zur Vorhersage des zu erwartenden Härteprofils.

Acknowledgements

The research presented in this thesis was conducted during my work at the Weierstrass Institute of Applied Analysis and Stochastics in the joint research project “MeFreSim” – Modeling, Simulation and Optimization of Multi-Frequency Induction Hardening as Part of Modern Production, funded by the German Federal Ministry of Education and Research (BMBF). I am grateful to a lot of colleagues who supported me during this work.

First of all I am obliged to my supervisor, Prof. Dr. Dietmar Hömberg, for his support during all the years and for giving me the opportunity to work on this research project. Furthermore, I want to thank Prof. Dr. Alfred Schmidt for the review of the thesis and the fruitful cooperation within the BMBF research project “MeFreSim” as well as the coworkers Dr. Oleg Boyarkin, Prof. Dr. Ronald Hoppe, Dr. Qinzhe Liu, Dr. Jonathan Montalvo-Urquizo, Dawid Nadolski and Dr. Alwin Schulz. Moreover, I want to express my gratitude to Dr. Hansjürg Stiele from EFD Induction for his patient explanations regarding induction hardening and to Prof. Dr. Elisabetta Rocca for her assistance with the mathematical analysis.

Special thanks go to the colleagues at Weierstrass Institute, Prof. Dr. Wolfgang Dreyer, Anke Giese, Clemens Guhlke, Dr. Daniela Kern, Dr. Oliver Rott and Natalya Togobitska. In particular I would like to mention Dr. Robert Huth for his moral support and the proofreading of the thesis, Timo Streckenbach and Dr. Wolf Weiss for patiently answering questions regarding `pdelib`, modelling and everything else. Furthermore, I would like to thank the members of the former Research Training Group “Analysis, Numerics and Optimization of Multiphase Problems”.

Finally, my thanks belong to my family, especially to my wife Kathrin for her support, her patience and her appreciation and to Lisa and Marie, who were motivation and inducement for the work on the thesis and provided balance and distraction at the same time.

Contents

1. Introduction	1
2. Physical background	7
2.1. Phase transitions in steel	7
2.1.1. Phases in steel	7
2.1.2. The austenite to ferrite phase transformation	9
2.1.3. The formation of pearlite	10
2.1.4. The formation of martensite	11
2.1.5. TTT-diagrams	11
2.2. The concept of multifrequency induction hardening	13
2.2.1. Description of induction hardening	13
2.2.2. Multifrequency induction hardening	14
3. The model	19
3.1. Electromagnetic effects	20
3.1.1. Maxwell's equations in differential form	20
3.1.2. Interface- and boundary conditions	21
3.1.3. Magnetic vector- and electric scalar potential	23
3.1.4. Characterization of electric sources	24
3.2. Phase fraction of austenite	26
3.3. Balance of energy	27
3.4. Characterization of the material parameters	29
3.5. Summary of the model	30
4. Analysis of a simplified model	33
4.1. Notation and preliminary assumptions	33
4.2. Hypotheses	36
4.3. Weak formulation and main theorem	37
4.4. Proof of the existence result	38
4.4.1. Existence of a (local in time) solution	38
4.4.2. Global a priori estimates	41
4.4.3. Stability estimate	45
5. Numerical solution of the induction hardening problem	49
5.1. Discretization in space by the Galerkin method	50
5.1.1. Introduction of the Galerkin method	50
5.1.2. The semi-discretized problem	52

5.2.	An overview of the finite element method	54
5.2.1.	The spatial decomposition of the computational domain	55
5.2.2.	An abstract definition of a finite element	55
5.2.3.	Finite elements for H^1	58
5.2.4.	Finite elements for $H(\text{curl})$	59
5.2.5.	About the spatial discretization of the phase fraction	62
5.3.	Discretization in time and nonlinear behaviour	63
5.3.1.	Discretization in time	63
5.3.2.	Nonlinearities	64
5.3.3.	Different time scales for heat diffusion and electromagnetic effects	66
5.3.4.	Time discretization of the coupled system	68
5.3.5.	On the existence of solutions for the discretized system	70
5.3.6.	Solution of the linearized systems	71
5.4.	Adaptive mesh generation	73
5.4.1.	A general adaptive algorithm	74
5.4.2.	A residual based error estimator for Maxwell's equation	75
5.4.3.	Strategies for the grid refinement	79
5.5.	Averaging of the magnetic permeability	81
5.6.	The complete algorithm to solve the induction hardening problem	83
6.	Simulation	85
6.1.	Test of the adaptive grid refinement	85
6.2.	Numerical simulations for discs	87
6.2.1.	Numerical simulations	87
6.2.2.	Experimental setup	92
6.2.3.	Experimental verification and discussion	94
6.3.	Numerical simulations for gears	96
6.3.1.	Numerical simulation	96
6.3.2.	Experimental verification	102
6.3.3.	Contour hardening of gears in an industrial setting	104
6.3.4.	Discussion	106
7.	Conclusion and Outlook	109
A.	Appendix	113
A.1.	Integral identities	113
A.2.	Material parameters for the steel 42CrMo4	114
A.2.1.	Specific heat capacity	114
A.2.2.	Heat conductivity	114
A.2.3.	Electrical conductivity	114
A.2.4.	Magnetic permeability	115
A.2.5.	Further parameters	116
A.3.	Averaging of the Joule heat	116

Chapter 1.

Introduction

For nearly all workpieces made of steel a surface heat treatment to raise the hardness and the wear resistance is indispensable. A classic method for the heat treatment of steel is induction hardening, where the heating is done by electromagnetic fields. Due to the induced eddy currents and the skin effect, the necessary heat to produce the high temperature phase austenite is generated directly in the workpiece. During the subsequent quenching, martensite forms in the boundary layer, which is characterized by its high hardness. Induction heating is a very fast and energy efficient process, since the heat is generated directly in the workpiece. Furthermore, in industrial applications, it can be integrated directly into the process chain. But due to the skin effect a contour hardening for gears is hardly possible using only a single frequency.

The recently developed concept of multifrequency induction hardening uses two superimposed alternating currents with different frequencies to generate a hardening profile following the contour. This method is well suited to harden complex workpieces such as gears, where the coupling distance to the inductor varies.

The determination of optimal process parameters requires a lot of experience and validation by time-consuming and costly experiments. Therefore, there is a huge demand for numerical simulations of multifrequency induction hardening. Though numerical simulations in 2D are commonly used by engineers, these can not reproduce complex shaped workpieces and inductor geometries. Especially at corners of workpieces a partial melting occurs first. This can only be resolved by 3D simulations. The computational time represents the biggest restriction in the professional application of simulation tools. In addition, there is only an insufficient support for complex 3D simulations in commercial software tools. Therefore, it is the aim of this thesis to develop an effective 3D simulation tool for multifrequency induction hardening of gears.

The main challenges for the design of a simulation tool for the multifrequency induction hardening process can be summarized as follows. For a correct reproduction of experimental results, the consideration of nonlinear material parameters is inevitable. In addition to temperature dependent material parameters, the magnetic permeability depends on the magnetic field itself, resulting from the magnetic saturation behaviour. These nonlinearities as well as the supply of a multifrequency inductor current generated by transistorized power converters require the solution of the model equations in the time domain instead of the easier to handle frequency domain. From an analytical point of view, the analysis of strongly coupled, nonlinear systems of partial differential equations resulting from the modelling of real world phenomena is always a challenge.

To make things worse, the coupled, nonlinear system represents a multiscale problem in time, since the typical time scales for heat conduction and electromagnetic processes differ by orders of magnitudes. In addition, due to the skin effect, different length scales must be considered as well. Compared to the overall workpiece dimensions, the induced eddy current density concentrates in a small boundary layer, which must be resolved by the space discretization. Therefore, the numerical solution requires the use of graduated grids, which can be generated adaptively.

While the modelling and the numerical simulation of induction hardening for axis symmetric workpieces in 2D is standard in commercial software, the effective simulation of the coupled system in 3D is a challenge itself. In 3D, the spatial discretization of Maxwell's equations requires the use of suitable methods, e.g. the finite element method using so-called edge elements.

The simulation of induction hardening gains much interest in the literature. In the following, an overview of the state of research regarding the modelling, analysis and the simulation of induction hardening is given. There are numerous articles regarding the simulation of induction hardening using a single frequency. In most cases, axial symmetric parts are considered. The simulations are usually done in the frequency domain, e.g. [16, 43]. The latter one considers the induction hardening of axial symmetric parts using a mixed finite element and boundary element method to solve the electromagnetic problem. A model combining electromagnetic, thermal and mechanical phenomena for axisymmetric induction heating processes is for example considered in [6]. Often, commercial software packages are used, e.g. [52], where a numerical and experimental study of the induction heat treatment of steel bars is carried out.

New requirements for numerical simulations appeared with the development of the multifrequency concept, [53]. There, multiple currents with frequencies that differ by more than a power of ten are supplied to one common inductor coil. With this concept it is possible to obtain a surface hardened region that follows the contour of complex shaped workpieces such as gears.

Finite element simulations in 3D using the multifrequency approach are done by Wrona [85]. There, the system is solved in the frequency domain using commercial finite element software. Since the software does not support the use of multiple frequencies directly, the different frequency powers are computed stepwise and separately at different time steps on a fixed grid. The stepwise calculation results in an oscillatory behaviour of the temperature, which is not desirable and the consideration of the equations in the frequency domain allows only the use of a constant magnetic permeability. In the present thesis, the consideration of nonlinear material data, especially the nonlinear magnetization curve, is essential to reproduce the experimentally obtained hardening profiles.

In order to judge the expected hardening profile, isothermal lines for the transformation temperature are compared to experimental hardening results. Phase transition kinetics are not considered. This can produce misleading results, since due to the extremely short heating times, a shift of the transformation temperature can occur and in addition, heat conduction effects after switching off the inductive heating might affect the transformed phase fraction.

A recent work considers the complete process of multifrequency induction hardening including the quenching stage and the computation of internal stresses, [72]. The computations are carried out in 2D for radial symmetric parts such as shafts. The magnetic field is computed in the frequency domain. Adaptive grid generation is not considered. An experimental validation shows good agreement with computational results in the case of multifrequency induction hardening, but only for radial symmetric workpieces. 3D simulations for multifrequency induction hardening of gears are considered in [68]. The magnetic saturation behaviour is taken into account by an iteration procedure, which results in a high increase of computational time.

For the analysis of induction heating problems there are results for the situation of Joule heating that consider the equations in the simpler frequency domain, [23, 31]. The equations in the time domain are considered in [38], where existence of a weak solution is shown, and in [40], where a stability estimate is given for the situation of constant material parameters.

Regarding the numerical solution of the induction hardening problem, adaptive finite element methods and corresponding error estimates are state of mathematical technology for the single components of the model such as heat conduction phenomena [69, 83, 88], and computational electromagnetics [7, 15, 70], only to mention some. We use these techniques to create adaptive grids that resolve the eddy current region with sufficient accuracy.

For solving Maxwell's equations by the finite element method, edge elements of Nédélec type are quite popular, [57, 58]. Based on this fundamental work, higher order methods were developed in the recent years [71, 86], introducing hierarchical finite element basis functions. Typically, the equations are considered in the frequency domain, which has limitations regarding nonlinear problems. In [3, 4] the so-called multiharmonic approach is investigated, which allows the solution of nonlinear problems in the frequency domain by considering truncated Fourier-expansions. If N denotes the number of Fourier coefficients, the advantage of avoiding a time-stepping scheme is compensated by an increase in dimension by a factor of $2N$. In addition, in the case of nonlinear problems, the resulting linear system for the Fourier coefficients is fully coupled. An efficient algorithm to solve linear systems of equations is the multigrid method [37]. The application of multigrid methods to induction heating problems is considered e. g. in [41]. Though the performance is indisputable, the implementation of these methods is quite involved.

The subject of this thesis is the modelling, the analysis and the simulation of multifrequency induction hardening in 3D. Using modern mathematical techniques, it is the aim to develop a high performance simulation tool, which is able to predict the hardening pattern with high accuracy. With the availability of effective algorithms, the numerical simulation of the process is not only a supplement, but can even become a replacement for time consuming experiments, such that the effectivity of multifrequency induction hardening as a cost- and energy efficient alternative to classic case hardening by carburization can be further increased.

The main contributions of this thesis are the following. A model is derived that reflects the different physical aspects of the induction hardening process. The tem-

perature evolution is determined by heat conduction effects, whereby the heat source is realized by electromagnetic fields. The phase transition kinetics to determine the expected hardening profile is modelled by rate laws that are based on experimental measurements.

For a realistic description, the consideration of nonlinear material parameters, especially the nonlinear magnetization curve, is essential. Furthermore, due to the arising nonlinearities and the periodic, but not necessarily harmonic source currents, the electromagnetic fields are considered in the time domain.

Regarding the respective model components, analytical results regarding the existence and uniqueness of solutions are known. For coupled, nonlinear PDE systems, these represent a challenge. Due to the high complexity, analytical investigations for a reduced model are considered, where the material parameters depend on the phase fraction but not on the temperature. The existence of a unique weak solution is established.

The numerical simulation is considered for the full nonlinear model. For the solution of the coupled system of partial differential equations in 3D the finite element method is applied, where for the electromagnetic subproblem curl-conforming finite elements are implemented. The efficient algorithmic realization is of great significance. With the mathematical optimization of the process in mind, where a repeated solution of the equations is necessary, the computational time is an important factor. For the simulation, modern mathematical techniques such as adaptivity and parallelization are utilized in order to account for the demands of a modern simulation software for the contour hardening of complex shaped workpieces.

The experimental verification of the simulation results for the inductive heating of discs and gears confirms the good performance of the solution algorithm. It is possible to resolve the contour hardened boundary layer for gears, where in addition to the profile in the cross section of the tooth also the lateral profile in the tip and the root of a tooth is reproduced.

The thesis is organized as follows. In the next chapter, we introduce the physical background. We describe the different phases in steel and the occurring phase transition mechanisms. Furthermore, a description of multifrequency induction hardening is given.

Chapter 3 is devoted to the modelling of the process. The equations describing the electromagnetic phenomena, the heat conduction effects and the transformation kinetics for the formation of the high temperature phase austenite are derived. Furthermore, thermodynamic consistency of the model is shown by applying the second law of thermodynamics.

In Chapter 4 the existence and uniqueness of solutions for a simplified model is investigated, where the material parameters depend only on space and the volume fraction of austenite, but are independent of the temperature.

The main part of the thesis is devoted to the numerical simulation of the induction heating process, see Chapter 5. The finite element method to solve the system of partial differential equations is introduced. The different aspects arising from nonlinearities, different time scales and other physical properties of the process, which need to be

considered in the simulation, are addressed and the overall algorithm to solve the induction hardening problem is given.

Finally, numerical simulations for disc and gear geometries are presented. The results are compared to experiments that were conducted by Institut für Werkstofftechnik (IWT), Bremen and EFD Induction, Freiburg. A summary of the thesis and an outlook for further developments is given in Chapter 7. In an Appendix, supplementary material and the material data used in the simulations is presented.

Chapter 2.

Physical background

Introduction

In general, the aim of any surface hardening process is to transform the boundary layer to a martensitic microstructure, which is characterized by an increased hardness. This improves the wear resistance. The essential feature is to create the martensitic structure only within a given depth, leaving the remaining part of the workpiece in its initial microstructure to reduce the chance of cracks by fatigue effects. The principal procedure for any surface hardening consists of the following steps:

- (i) Heating of the workpiece, respectively the surface area to the required austenitization temperature,
- (ii) holding of the process temperature in order to ensure a complete austenitization,
- (iii) rapid cooling to room temperature such that the hard phase martensite forms.

Knowledge of the different phases in steel and the occurring phase transition mechanisms is necessary to understand the process of induction hardening. In the next section, the different phases in steel are introduced. Then, the process of induction hardening using the multifrequency concept is explained.

2.1. Phase transitions in steel

2.1.1. Phases in steel

Steel mainly consists of iron and carbon. Industrial steels contain a large number of further alloying elements such as chromium, manganese, silicon or nickel that affect the properties and hardness of the steel but the most important alloying element is carbon.

We start with the description of pure iron. Pure iron is very soft and ductile. Therefore, it is not used as construction material. But due to the high magnetic permeability it is an important material in electronics. The cooling and heating curve of pure iron is depicted in Figure 2.1. Below the melting temperature of 1536 °C iron crystalizes as δ -iron with a body centred cubic structure (bcc). On further cooling, the iron transforms into the face centred cubic γ -iron at a temperature of 1392 °C. This modification and also the solid solutions with an fcc-crystal structure in steel are denoted as *austenite*. At a temperature of 906 °C, the point Ar₃, the iron transforms

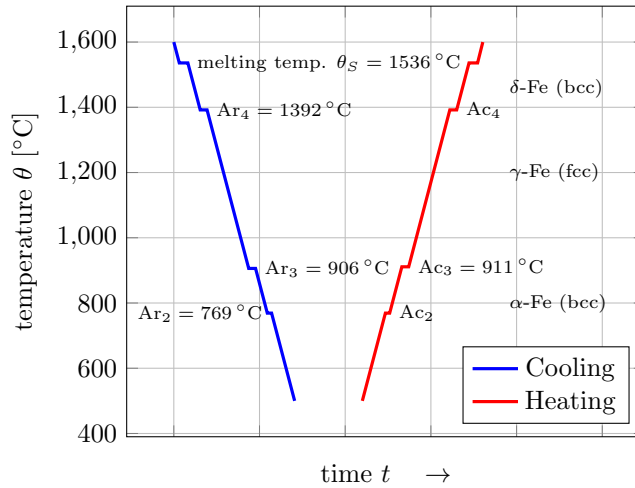


Figure 2.1.: Cooling and heating curve of pure iron, adapted from [5]

again into a bcc crystal, the α -iron. This structure and also the corresponding phase in steel, which is stable at room temperature, are denoted as *ferrite*, [5]. The two lattice structures, bcc and fcc, are depicted in Figure 2.2. The fourth holding point (Ar_2) at

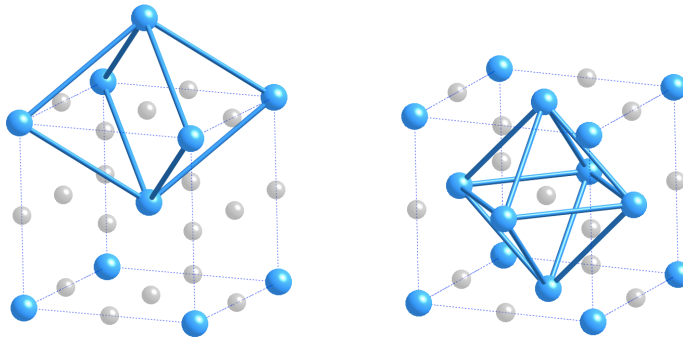


Figure 2.2.: BCC- and FCC-unit cell of ferrite and austenite

a temperature of 769°C is denoted as the *Curie-temperature*. This point is not related to a lattice transformation. At the Curie-temperature the magnetic properties change from paramagnetic at high temperatures to ferromagnetic. As indicated in Figure 2.1, the temperatures at which the phase transition occur can be different for heating and cooling (thermal hysteresis). Therefore, one has to clearly distinguish between the holding points on heating, denoted by Ac (*arrêt chauffage*) and cooling, Ar (*arrêt refroidissement*). The effect of thermal hysteresis increases with an increase of the heating and cooling rates. Especially in induction hardening very high heating and

cooling rates occur. This influences the temperatures at which the phase transitions take place. In addition, the effect of thermal hysteresis increases with the addition of alloying elements.

There are two different possibilities to dissolve alloying elements, either as substitutional or interstitial solid solution. Usually, metallic alloying elements such as nickel, chromium, manganese and many others are dissolved as substitutional solution, the alloy atoms replace an iron atom in the corresponding bcc- or fcc-lattice. The lattice structure stays the same.

This is different for carbon. Carbon is dissolved on interstitial lattice sites and forms an *interstitial solution*. The bcc- and fcc-iron crystals form interstitial lattices consisting of tetrahedral and octahedral sub-lattice sites. Carbon is dissolved on octahedral lattice sites. These are smaller than the atomic diameter of carbon, which results in a distortion of the parent bcc- or fcc-lattice, see also Table 2.1. This distortion is even

	size of interstices	size ratio interstices/carbon atom
octahedral site bcc	$0.154 \cdot r_{\text{Fe}}$	25.6 %
tetrahedral site bcc	$0.291 \cdot r_{\text{Fe}}$	48.5 %
octahedral site fcc	$0.41 \cdot r_{\text{Fe}}$	68.3 %

Table 2.1.: Sizes of interstices in bcc- and fcc-iron ($r_{\text{Fe}} = 1.28 \text{ \AA}$, $r_{\text{C}} = 0.77 \text{ \AA}$, diameter of iron/carbon atom)

larger for the bcc-lattice, which results in different maximum solubilities of carbon in ferrite and austenite. The maximum solubility of carbon in γ -iron is 2% per mass while in α -iron it is only 0.02%. Despite the larger diameter of the tetrahedral sub-lattice site in bcc-iron, carbon is dissolved on octahedral sites since a dissolved carbon atom on tetrahedral interstices causes a larger lattice deformation, cf. [5].

Alloying elements, especially carbon, have a huge influence on the lattice transformation from fcc to bcc and consequently on the phase transition kinetics. In the following, the most important phase transformation mechanisms in steel are described.

2.1.2. The austenite to ferrite phase transformation

In steel, one distinguishes between reconstructive and displacive transformations, [10]. An example for the latter one is the formation of martensite by rapid quenching, see Section 2.1.4, while the decomposition of austenite into ferrite at high temperatures can be characterized as reconstructive transformation. The movement of atoms is thermally activated. Therefore, diffusion effects are significant at high temperatures and control the phase transition from austenite to ferrite.

When cooling the steel below the A_{r3} -temperature, it is more favourable from an energetic point of view that the iron atoms arrange in a bcc-crystal instead of the fcc-structure of austenite. This process usually starts by nucleation of an α -nucleus at an austenitic grain boundary. Since the carbon solubility in ferrite is much smaller than in austenite, carbon has to diffuse into the parent austenite and is accumulated

at the α/γ -interface. The iron atoms are able to cross the interface immediately and change their crystallographic orientation. The ferrite nucleus grows by movement of the α/γ -interface at the expense of the austenite. If the atoms are attached to the ferrite nucleus randomly, the interface can propagate readily in all directions, [24]. The excess carbon that accumulates at the interface forms a barrier for further carbon atoms that are rejected from the ferrite. The pile up of carbon at the interface has to be balanced by diffusion. Therefore, the carbon diffusion determines the kinetics of the phase transition process. At high temperatures, the movement is rapid, while a reduction in temperature lowers the mobility of the atoms and consequently the velocity of the transformation front.

If the carbon concentration in austenite is too high such that it can not be balanced by diffusion, the carbon enriched compound cementite precipitates from the parent austenite. At the eutectoid concentration of 0.8 %, ferrite and cementite crystallize by an alternating process and pearlite forms.

2.1.3. The formation of pearlite

Pearlite is a lamellar mixture of the phases ferrite and the metastable compound cementite with the structural formula Fe_3C . The first step of the formation of pearlite is the nucleation of one of the components, either ferrite or cementite at grain boundaries of the parent austenite. Though the formation of pearlite has been described in considerably detail in the literature and is subject of many investigations, some aspects are still not fully understood. One of them is e. g. the role of the active nucleus, [87]. The following description of the formation of pearlite follows [63].

It is assumed that cementite is the active nucleus. Since cementite has a high carbon concentration (6.66 %), the surrounding of the nucleus depletes in carbon, which favours the formation of ferrite. Ferrite forms adjacent to the cementite and carbon is rejected into the austenite matrix. The enrichment in carbon favours the formation of cementite. This process repeats and the pearlite colony grows sidewise along the grain boundary.

In addition to the sidewise growth, the colony also grows edgewise into the austenite grain. The rate of the edgewise growth is controlled by the diffusion of carbon from the tips of the ferrite lamella to the tips of the cementite lamella. Therefore, the diffusion of the rejected carbon through the austenite affects the morphology of pearlite. At higher undercooling the mobility of the carbon atoms is more and more limited, which results in a smaller distance of the lamellas and therefore a finer structure of pearlite.

If the alloy composition does not correspond to the eutectoid composition of 0.8 % first, ferrite or cementite nucleates and covers the grain boundaries as pro-eutectoid ferrite (in hypoeutectoid steel) or pro-eutectoid cementite (in hypereutectoid steel) until the remaining parental austenite reaches the composition of 0.8 %. Then, the transformation takes place as described above.

2.1.4. The formation of martensite

Martensite forms by a diffusionless phase transformation from the austenite in the case of rapid cooling below the martensite start temperature M_s . Due to the rapid cooling, diffusion processes are suppressed, the transformation is characterized as displacive and happens by a diffusionless shear transformation of the iron lattice. The iron atoms move only marginal by a fraction of the atomic diameter. The carbon atoms, which are dissolved in the fcc-crystal of austenite, are forced to their interstitial sites. This results in a supersaturated, tetragonal distorted bcc-lattice. These lattice distortions are the reason for the high hardness of martensite.

The fraction of martensite $z_{\alpha'}$ that is produced can be estimated by the equation of Koistinen and Marburger, [47]

$$1 - z_{\alpha'} = \exp(-\beta(M_s - \theta)),$$

where $\beta > 0$ is a parameter to be determined by experiments and θ denotes the quench temperature. As one can see, there is no time dependence in the equation above. The martensite formation is considered as a-thermal due to a very rapid nucleation and growth. Therefore, the time dependence can be ignored. The driving force is the undercooling below the martensite start temperature M_s . There is always a fraction of retained austenite, which can also be estimated by the relation above, it corresponds to the fraction $1 - z_{\alpha'}$.

The temperature at which no more martensite forms on further cooling is denoted as the martensite finish temperature, M_f . In the relation above, there is no martensite finish temperature, in applications it is defined as the temperature that corresponds to a martensite fraction of $z_{\alpha'} = 0.95$.

In order to produce as much martensite as possible, a rapid cooling is necessary. The cooling rate, at which no additional phases such as ferrite, pearlite or bainite are produced, is called the critical cooling rate. The martensite start and finish temperatures M_s and M_f as well as the critical cooling rate depend essentially on the alloying elements and the carbon content. They are different for the various types of steel. Therefore, not every steel is suitable to produce high amounts of martensite and consequently not suitable for induction hardening.

In the past decades further approaches to describe the formation of martensite were developed. We refer to [80] for a survey and a comparison of different model equations to describe the temporal evolution of martensite.

2.1.5. TTT-diagrams

The microstructure and the distribution of the different phases such as ferrite, pearlite or martensite is crucial for the mechanical properties of the steel. An important tool characterizing the temperature and carbon-concentration dependent state of the phases is the iron-carbon phase diagram. It shows the stable phases at a given temperature and a given mean carbon concentration and provides insight in the occurring phase transitions. With the help of the iron-carbon diagram it is for example possible to determine the carbon concentration and the volume fraction of the pure phases in a

phase mixture using the so called lever rule, cf. [34]. Unfortunately, the diagram provides no information on the transformation rates, the distribution of the phases or the microstructure. The validity of the phase diagram is limited to processes that occur at conditions close to equilibrium, i. e. at extremely slow cooling rates, and involve no mechanical effects or the occurrence of phase like martensite, which develop through displacive transformations far from diffusional equilibrium.

Most of the steels used in practical applications contain in addition to carbon further alloying elements such as chromium, manganese, silicon or nickel. These substitutional alloying elements have a huge influence on the material properties. The temperature at which a phase transition occurs can change or even the occurrence of a phase is skipped at all. This is also not reflected in the iron-carbon diagram and its application is limited. Further tools are required to describe the temporal transformation behaviour of the formation of pearlite or the formation of martensite.

The temporal transformation process involves nucleation and growth and is conventionally represented by *time-temperature-transformation (TTT)-diagrams*. The degree of transformation is indicated over time, usually on a logarithmic scale. These diagrams must be interpreted exclusively at constant temperatures. The determination of these diagrams is carried out by isothermal experiments for a multitude of specimens of a single type of steel in order to determine the time that is necessary to obtain a given pearlitic fraction. This diagram is then valid only for the specific steel with the corresponding composition.

Isothermal transformations have in general only little relevance for industrial applications. Usually in the manufacturing process, the temperature is not constant. The transformation kinetics under non-isothermal conditions is depicted in continuous cooling transformation (CCT)-diagrams. There, the state of the phase transition is indicated along given cooling profiles, see Figure 2.3. The different lines indicate the beginning and the end of the transformation along the temperature curve for a given cooling rate. In addition, the martensite start and finish temperatures are indicated and the critical cooling rate, at which only martensite forms, can be obtained. The knowledge of the critical cooling rate is essential for the induction hardening process, since the formation of any undesired phase such as ferrite, pearlite or bainite during the quenching, must be suppressed. On the other hand, the cooling rate is restricted by technical limitations and the critical cooling rate is an indicator if the steel is suitable for induction hardening.

The reverse process, the formation of austenite from a ferritic and pearlitic matrix during the heating is represented by *time-temperature austenitization (TTA)-diagrams*, see Figure 2.4. Due to the thermal hysteresis, the Ac_3 temperature at which austenite forms is shifted to higher temperatures with increasing heating rate. This has to be taken into account in the induction heating process with its short heating times. It is necessary to heat the specimen to higher temperatures to achieve a complete austenitization.

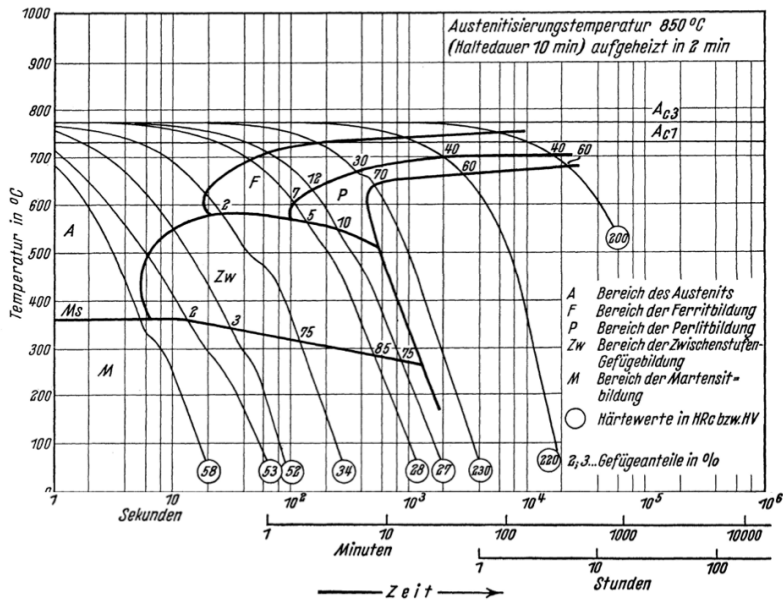


Figure 2.3.: Continuous cooling diagram for the steel 42CrMo4, [84]

2.2. The concept of multifrequency induction hardening

2.2.1. Description of induction hardening

In induction hardening as a method for the heat treatment of steel, the necessary heat to transform the boundary layer to austenite is generated by induced electric currents. The principle is the following. A coil that is connected to an alternating current source (converter) generates a periodically changing electromagnetic field. The temporal changing magnetic flux induces a current in the workpiece that is enclosed by the induction coil. Due to the resistance of the workpiece, some part of the power is transformed into eddy current losses and a heating of the workpiece results (Joule heating).

The induced current itself generates a magnetic field, which opposes the inductor current. The electric fields superimpose each other. This results in a decrease of the magnetic field and consequently of the electric field in radial direction. As a consequence, the eddy currents are concentrated in the surface layer of the workpiece. This is called the *skin effect*.

The penetration or skin depth of the electric current is defined as the depth δ at which the current density reduces to 37% of its maximum value, [8]. The penetration depth depends on the electric and magnetic properties of the workpiece, but mainly on the frequency of the alternating current. Simplified, there holds the following relation

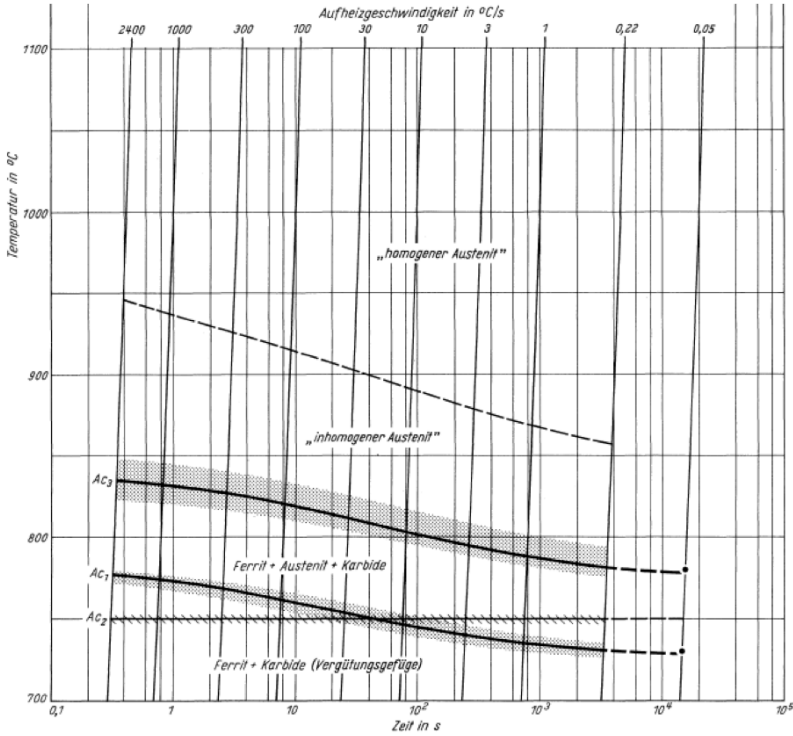


Figure 2.4.: Time-temperature-austenitization diagram for the steel 42CrMo4, [59]

$$\delta = \frac{1}{\sqrt{\pi \sigma \mu f}}, \quad (2.1)$$

where σ [$\text{A mm}^2/\text{Vm}$] denotes the electric conductivity, μ [Vs/Am] the magnetic permeability and f [$1/\text{s}$] the frequency. One has to note that the material parameters are temperature dependent. Consequently, the penetration depth changes during the heating. In addition, the relative permeability depends on the magnetic field intensity. However, the frequency is the most significant parameter to control the penetration depth, see also Figure 2.5, where the penetration depth is depicted for different temperatures and materials.

2.2.2. Multifrequency induction hardening

Since the penetration depth depends on the frequency of the inductor current, it is difficult to obtain a uniform contour hardened surface area for complex workpiece geometries such as gears using a current with only one fixed frequency. If for example, a high frequency (HF) is applied, then the penetration depth is small and it is possible to harden only the tip of the tooth. With a medium frequency (MF) it is possible to

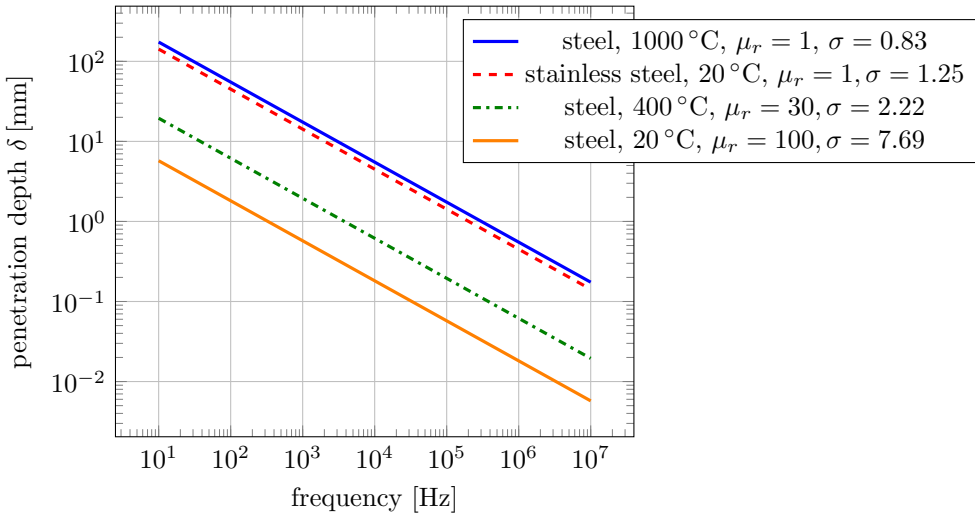


Figure 2.5.: Penetration depth δ in dependence on the frequency of the inductor current, [51]

heat the root of the tooth, but not the tip. With a single frequency, a hardening of the whole tooth can only be achieved by increasing the heating time. But then, the complete tooth is heated beyond the austenitization temperature, which results in a complete martensitic structure of the tooth after quenching. This is also not desirable, since the chance of material failure increases.

The recently developed approach is to supply both frequency powers simultaneously. This concept is called *multifrequency induction hardening*, see also Figure 2.6. In order

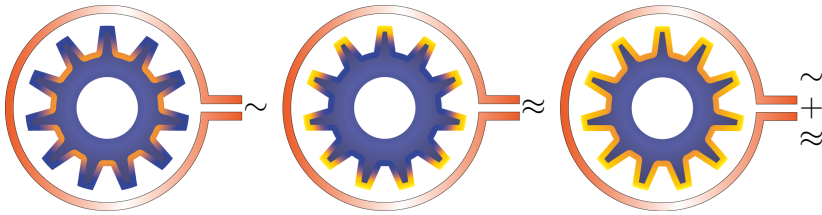


Figure 2.6.: The effect of medium-, high- and multifrequency induction heating; MF (left): only the root of the tooth is heated, HF (middle): only the tip of the tooth is heated, MF+HF (right): tip and root of the tooth are heated (adapted from [73])

to achieve a hardening profile that follows the contour of the gear, very short heating times are necessary in order to avoid heat diffusion into the workpiece. In the past, multifrequency hardening was performed by subsequent heating of gearwheels in two separate inductors that are fed by power supplies with different frequencies. With

short heating times of below 500 ms [62], which is typical for the application to gears, the transfer of the workpiece from one inductor to the other leads to a break in the heating and to a degradation of the temperature field [26].

Newer developments in dual-frequency induction hardening do not require a frequency changeover. MF and HF energy are supplied simultaneously to one inductor. The inductor current consists of a medium frequency fundamental oscillation superimposed by a high frequency oscillation. The amplitudes of both frequencies are independently controllable, which allows separate regulation of the respective shares of the output power of both frequencies according to the requirements of the workpiece. This provides the ability to control the depth of hardening at the root and the tip of the tooth, [74].

The principal construction of an induction hardening machine is depicted in Figure 2.7 for the single frequency case. It consists of an energy source (converter), the inductor and a quenching device.

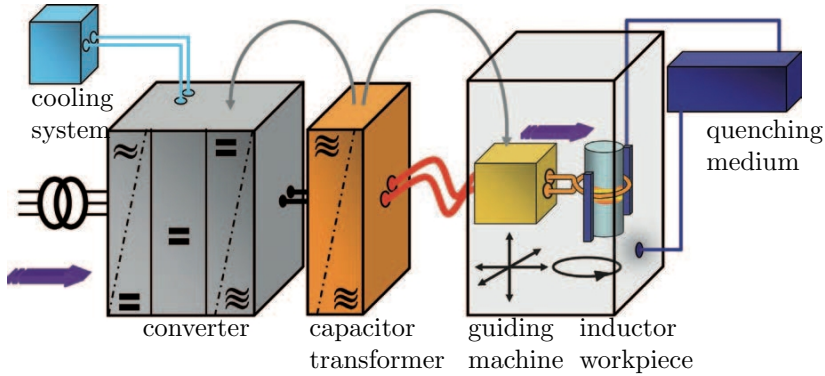


Figure 2.7.: Schematic picture of an induction hardening machine, [51]

The induction coil is in general made of copper. To reduce the costs, hollow profile bars are used. Water flows through the interior of the coil for cooling purpose. The form of the inductor has to be adapted to the workpiece geometry.

The power supply is usually realized by transistorized MF and HF converters. Together with the induction coil, the MF and HF circuits form oscillating circuits. In order to compensate the reactive power, additional capacitors for the MF and HF loops are necessary. To prevent the HF power entering the MF circuit, an HF filter is used in the MF resonant circuit. The MF and HF converters are designed in such a way that they work at the resonance frequency of the oscillating circuits consisting of the induction coil, the workpiece and additional filters and compensation capacitors. The frequency lies in a range of approximately 10 – 25 kHz for medium frequency and 100 – 400 kHz for high frequency. There are different possibilities to design the MF and HF circuit, either as serial or parallel resonant circuit, [26]. Typically, the MF

and HF circuit are connected to the induction coil by an inductive coupling, i. e. by a transformer.

The energy of the medium- and high-frequency converter can be regulated variable, typically the power is adjusted as relative value between 1 and 99 %. From a technical point, the regulation of the energy is done by a pulse-width modulation for the medium frequency converter and by pulse package control for high frequency, see also [28, 85] for examples of the time-dependent current and voltage at the output of the MF and HF converter.

The inductor voltage or the current, which is required in 3D simulations of the induction hardening process as input parameter, can be determined by a simulation of the resonant circuits. The oscillating circuits for each frequency can be represented by an equivalent circuit diagram that consists of capacitors, inductances and resistors, which are unknown and have to be determined by a parameter identification. The inductor itself can be represented by an inductance and a resistance that are the common parts of each of the both resonant circuits. The parameters of the equivalent circuit of the inductor are temperature dependent and have to be determined from the 3D simulation, [26, 27].

In order to solve for the inductor current, a system of ordinary differential equations has to be solved. The resulting current in the inductor will be periodic, but not necessarily harmonic. This is one of the reasons why the computation of the electromagnetic fields is considered in the time domain instead of the typically used frequency domain. A further reason will be the nonlinear behaviour of material parameters such as the magnetic permeability. Due to the high complexity of the MF- and HF-converter, the simulation of the converter by an equivalent circuit is not considered in this work. The input parameters for the simulation are taken from accessible quantities at the machine, e. g. measurements of the inverter current and knowledge of the transmission ratio.

In induction heating, the heat is generated directly in the workpiece and affects only the desired regions, which makes the process very energy efficient. Furthermore, due to the short heating times, mechanical distortion is reduced and it is possible to integrate induction hardening machines directly into the process chain. With the concept of multifrequency induction hardening a contour hardening of gears is possible, such that for industrial applications induction hardening has become a cost- and energy efficient alternative to classic case hardening by carburization, [8, 74].

Chapter 3.

The model

Introduction

In order to simulate induction heating processes we need to determine the distribution of the temperature θ and the high temperature phase austenite z in the workpiece. It is assumed that during the quenching process that follows the inductive heating, austenite transforms completely into martensite and is therefore an indicator of the hardening profile. The austenitization behaviour is directly linked to the temperature distribution by the transformation kinetics.

The heat is generated by the Joule effect: An alternating current flows through the inductor, which generates a temporal changing magnetic field. This magnetic field induces a voltage and consequently generates eddy currents in the workpiece. Due to resistive losses, heat is generated directly in the workpiece. The interdependence between the afore mentioned physical quantities is depicted in Figure 3.1.

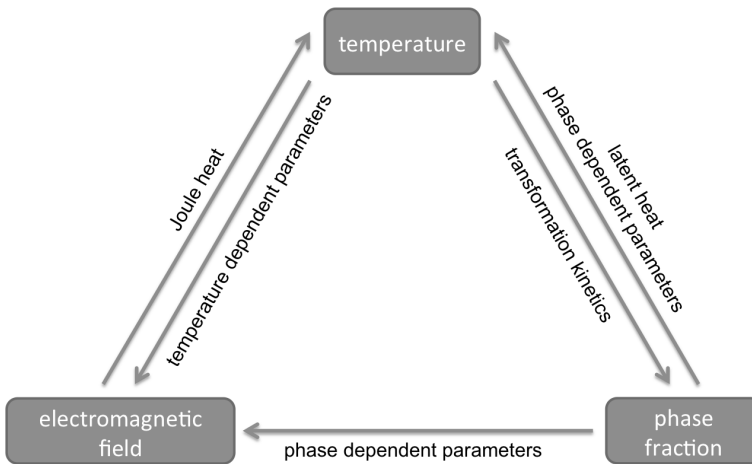


Figure 3.1.: Schematic representation of the model

The physical effects during the induction heating process can be described by a coupled system of partial and ordinary differential equations. It comprises of the heat equation describing the temperature distribution, an ordinary differential equa-

tion (ODE) to simulate the phase evolution and Maxwell's equations to describe the electromagnetic processes. This system is derived in the following.

For the geometric setting, we consider a domain $D \subset \mathbb{R}^3$ that consists of the inductor Ω , the workpiece Σ , and the surrounding air, see Figure 3.2. The connection to the

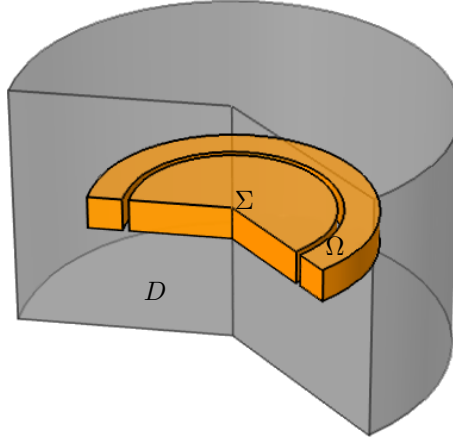


Figure 3.2.: Domain D consisting of the inductor Ω , the workpiece Σ and the surrounding air

converter is modelled by an idealized interface condition on a cross section of the inductor, cf. Section 3.1.4. The derivation of the partial differential equations requires integral identities that are given in Appendix A.1. Having introduced the geometric setting, we start with the explanation of Maxwell's equations.

3.1. Electromagnetic effects

3.1.1. Maxwell's equations in differential form

The electromagnetic effects are described by Maxwell's equations, which are presented in their differential form [50]. They consist of a system of partial differential equations connecting the magnetic field \mathbf{H} [A/m], the magnetic induction \mathbf{B} [Vs/m²], the electric field \mathbf{E} [V/m] and the electric displacement field \mathbf{D} [As/m²]

$$\begin{aligned}
 \operatorname{curl} \mathbf{E} &= -\frac{\partial \mathbf{B}}{\partial t} \\
 \operatorname{div} \mathbf{B} &= 0 \\
 \operatorname{curl} \mathbf{H} &= \mathbf{J} + \frac{\partial \mathbf{D}}{\partial t} \\
 \operatorname{div} \mathbf{D} &= \rho.
 \end{aligned} \tag{3.1}$$

The quantities on the right hand side are the current density \mathbf{J} [A/m²] and the charge density ρ [As/m³]. The first equation is also denoted as Faradays law of induction.

It states that a time varying magnetic field is accompanied by an electric field. The equation $\operatorname{div} \mathbf{B} = 0$ states that there are no magnetic sources, the magnetic flux density \mathbf{B} is a solenoidal field. Ampere's law, the third equation in (3.1), describes the fact that moving electric charges or electric currents generate a magnetic field. Finally, Gauss' law relates the distribution of electric charges to the resulting electric displacement field.

Maxwell's equations are completed by constitutive laws

$$\mathbf{D} = \varepsilon \mathbf{E} \quad \text{and} \quad \mathbf{B} = \mu \mathbf{H} \quad (3.2)$$

with material dependent parameters ε and μ , the electrical permittivity and the magnetic permeability. The current density and the electric field are related by Fourier's law

$$\mathbf{J} = \sigma \mathbf{E}, \quad (3.3)$$

where σ denotes the electrical conductivity.

The conservation of charge demands that the following compatibility condition holds. Taking the divergence of the third equation in (3.1) together with $\operatorname{div} \operatorname{curl} \mathbf{H} = 0$ yields

$$\operatorname{div} \mathbf{J} + \frac{\partial \rho}{\partial t} = 0. \quad (3.4)$$

Since the total charge is conserved, a change of the charge in a volume must be balanced by a flow of charge, i. e. an electric current, through the surface of the volume, [42].

3.1.2. Interface- and boundary conditions

For the electromagnetic fields, there hold certain continuity conditions at interfaces, where material properties change. These can be derived from Maxwell's equations (3.1) with the help of Gauss' and Stokes' theorems, Thm. 3 and 4 in Appendix A.1. We denote by V an arbitrary volume element in space and by A an arbitrary surface element. Then there holds

$$\int_V \operatorname{div} \mathbf{B} \, dx = \int_{\partial V} \mathbf{B} \cdot \mathbf{n} \, da \quad \text{and} \quad \int_A \operatorname{curl} \mathbf{E} \cdot \mathbf{n} \, da = \int_{\partial A} \mathbf{E} \cdot \boldsymbol{\tau} \, ds,$$

where \mathbf{n} is the outward normal vector of the surface ∂V respectively A and $\boldsymbol{\tau}$ denotes the tangential vector of the line element ∂A .

We consider a volume element $V = V_1 \cup V_2$ that is separated by an interface $\Gamma = V_1 \cap V_2$. Integration of $\operatorname{div} \mathbf{B} = 0$ over V and V_i , $i = 1, 2$, together with Gauss' theorem (Thm. 3) yields

$$\begin{aligned} 0 &= \int_{\partial V} \mathbf{B} \cdot \mathbf{n} \, da - \int_{\partial V_1} \mathbf{B}_1 \cdot \mathbf{n} \, da - \int_{\partial V_2} \mathbf{B}_2 \cdot \mathbf{n} \, da \\ &= \int_{\Gamma} \mathbf{B}_1 \cdot \mathbf{n}_{\Gamma} \, da - \int_{\Gamma} \mathbf{B}_2 \cdot \mathbf{n}_{\Gamma} \, da = - \int_{\Gamma} \llbracket \mathbf{B} \cdot \mathbf{n}_{\Gamma} \rrbracket \, da, \end{aligned}$$

where \mathbf{n}_Γ denotes the unit normal vector of the interface Γ , pointing from V_2 into V_1 , $\mathbf{B}_i = \mathbf{B}|_{V_i}$, $i = 1, 2$, and $[[\mathbf{B}]] = \mathbf{B}_2 - \mathbf{B}_1$ denotes the jump of the magnetic induction across the interface Γ . Since the volume element V can be chosen arbitrary, there holds

$$[[\mathbf{B} \cdot \mathbf{n}_\Gamma]] = 0, \quad (3.5)$$

i. e. the normal component of the magnetic induction is continuous at interfaces.

Now, we consider a surface A that intersects the interface Γ in a line L . Applying Stokes' theorem (Thm. 4), we finally derive by similar arguments the relation

$$[[\mathbf{E} \times \mathbf{n}_\Gamma]] = 0, \quad (3.6)$$

i. e. the tangential components of the electric field \mathbf{E} are continuous. By analogous considerations, one obtains the relations

$$[[\mathbf{H} \times \mathbf{n}_\Gamma]] = \mathbf{J}_\Gamma \quad \text{and} \quad [[\mathbf{D} \cdot \mathbf{n}_\Gamma]] = \rho_\Gamma \quad (3.7)$$

with a surface current density \mathbf{J}_Γ and a surface charge density ρ_Γ , see e. g. [42].

From these relations and the material laws (3.2) one obtains that the normal or the tangential components of the electromagnetic fields exhibit discontinuities across material interfaces. For simplicity, it is assumed that $\mathbf{J}_\Gamma = 0$ and $\rho_\Gamma = 0$. Then in the case of jumping parameters μ and ε across the interface Γ there holds

$$[[\mathbf{B} \times \mathbf{n}_\Gamma]] \neq 0, \quad [[\mathbf{H} \cdot \mathbf{n}_\Gamma]] \neq 0, \quad [[\mathbf{E} \cdot \mathbf{n}_\Gamma]] \neq 0 \quad \text{and} \quad [[\mathbf{D} \times \mathbf{n}_\Gamma]] \neq 0. \quad (3.8)$$

From the jump conditions (3.6) and (3.7) it is possible to derive boundary conditions if the material on one side of the interface can be modelled as a perfect electric or magnetic conductor. Then, the following boundary conditions are imposed in the case of a

perfect electric conductor (PEC):

$$\mathbf{E} \times \mathbf{n} = 0 \quad \text{on} \quad \partial D,$$

perfect magnetic conductor (PMC):

$$\mathbf{H} \times \mathbf{n} = 0 \quad \text{on} \quad \partial D,$$

prescribed surface current:

$$\mathbf{H} \times \mathbf{n} = \mathbf{J}_\Gamma \quad \text{on} \quad \partial D$$

with the surface current density \mathbf{J}_Γ . Further boundary conditions, e. g. the impedance boundary condition [55], are not considered in this work.

3.1.3. Magnetic vector- and electric scalar potential

To reduce the system consisting of four partial differential equations plus material laws, the vector potential formulation of Maxwell's equations is usually derived using the relations $\text{curl } \nabla f = 0$ and $\text{div } \text{curl } \mathbf{v} = 0$, where $f : D \rightarrow \mathbb{R}$ denotes a scalar valued and $\mathbf{v} : D \rightarrow \mathbb{R}^3$ a vector valued function over D . From the relation $\text{div } \mathbf{B} = 0$, cf. equation (3.1)₂, we have the existence of the magnetic vector potential \mathbf{A} such that

$$\mathbf{B} = \text{curl } \mathbf{A}.$$

Using (3.1)₁, there holds

$$\text{curl} \left(\mathbf{E} + \frac{\partial \mathbf{A}}{\partial t} \right) = 0.$$

As a consequence, we have the existence of the electric scalar potential ϕ such that

$$\mathbf{E} = -\nabla \phi - \frac{\partial \mathbf{A}}{\partial t}.$$

The magnetic vector potential \mathbf{A} is not unique. The addition of an arbitrary gradient field $\nabla \psi$ yields the same magnetic induction \mathbf{B} . Therefore, certain gauging conditions need to be defined to ensure uniqueness. For induction phenomena, usually the Coulomb-gauging is used:

$$\text{div } \mathbf{A} = 0. \quad (3.9)$$

A typical assumption for the modelling of induction phenomena is that the term $\partial \mathbf{D} / \partial t$ is small compared to the current density \mathbf{J} and can be neglected. Therefore, there is a coupling between the magnetic and the electric field only in conductive regions, the dielectric displacement has no influence on the description of eddy current effects. The electric field and the current density are linked by Fourier's law $\mathbf{J} = \sigma \mathbf{E}$, cf. (3.3). Therefore, the total current density is given by

$$\mathbf{J} = -\sigma \frac{\partial \mathbf{A}}{\partial t} - \sigma \nabla \phi \quad \text{in } D \quad (3.10)$$

with $\sigma = 0$ in nonconducting regions $D \setminus (\Sigma \cup \Omega)$. Introducing this relation into (3.1) together with the compatibility condition $\text{div } \mathbf{J} = 0$, equation (3.4), and the gauging condition (3.9) yields the vector potential formulation of Maxwell's equations

$$\begin{aligned} \sigma \frac{\partial \mathbf{A}}{\partial t} + \text{curl } \frac{1}{\mu} \text{curl } \mathbf{A} + \sigma \nabla \phi &= 0 \quad \text{on } D \\ -\text{div } \sigma \nabla \phi &= 0 \quad \text{on } \Omega. \end{aligned} \quad (3.11)$$

Please note that the inductor Ω is the only region with a prescribed source current or source voltage. Therefore, the electric scalar potential vanishes everywhere except for the domain Ω .

If we transform the boundary conditions introduced above to the vector potential \mathbf{A} , there holds

$$\mathbf{A} \times \mathbf{n} = 0 \quad (\text{PEC}), \quad \mu^{-1} \text{curl } \mathbf{A} \times \mathbf{n} = 0 \quad (\text{PMC}). \quad (3.12)$$

These conditions can be considered as analogue to standard Dirichlet- and Neumann-boundary conditions, respectively. At material interfaces there holds in analogy to (3.6)

$$\llbracket \mathbf{A} \times \mathbf{n} \rrbracket = 0, \quad (3.13)$$

i. e. the tangential components of the magnetic vector potential \mathbf{A} are continuous.

In general, Maxwell's equations are defined on an infinite domain. Since the magnetic field decreases to zero with exponential decay in the absence of electric currents, we set the magnetic vector potential \mathbf{A} to zero if we are sufficiently away from the region of interest, i. e. the workpiece and the inductor. Therefore, the surrounding air has to be considered and we impose the boundary condition

$$\mathbf{A} \times \mathbf{n} = 0 \quad \text{on} \quad \partial D. \quad (3.14)$$

The electric scalar potential is only different from zero in the inductor Ω . The inductor itself is represented by a torus. The connection clamps are ignored, they are modelled by an interface condition on a cross section area of the inductor denoted as Γ . The normal derivative $\sigma \nabla \phi \cdot \mathbf{n}$ represents the current. Since there is no current flowing perpendicular to the surface of the inductor the following boundary condition is imposed for the electric scalar potential

$$\sigma \nabla \phi \cdot \mathbf{n} = 0 \quad \text{on} \quad \partial \Omega. \quad (3.15)$$

A prescribed current or voltage source is realized by an interface condition on Γ . The electric current through the cross section Γ is always continuous. The voltage is defined as a potential difference between the connection pins. In our model this is realized by a jump condition for the potential ϕ , i. e.

$$\llbracket \sigma \nabla \phi \rrbracket \cdot \mathbf{n} = 0 \quad \text{and} \quad \llbracket \phi \rrbracket = u(t) \quad \text{on} \quad \Gamma, \quad (3.16)$$

where $\llbracket \cdot \rrbracket$ denotes the jump of a quantity across Γ and $u(t)$ denotes the voltage. The characterization of the scalar potential given above is due to [55].

3.1.4. Characterization of electric sources

In order to characterize the electric sources in terms of a given voltage or an electric current in the inductor we introduce the source current density as

$$\mathbf{J}_{\text{src}} = -\sigma \nabla \phi, \quad (3.17)$$

which has to satisfy $\text{div} \mathbf{J}_{\text{src}} = 0$. Then, for the total current density (3.10) there holds

$$\mathbf{J} = -\sigma \partial_t \mathbf{A} + \mathbf{J}_{\text{src}}. \quad (3.18)$$

In the case of a rotational symmetric inductor Ω as e. g. in Figure 3.2 it is possible to obtain an analytic expression for the electric scalar potential ϕ . In order to do this, we solve equation (3.11)₂ with respect to cylindrical coordinates (r, φ, z) and assume

that the current in r - and z -direction is equal to zero. The equation $-\operatorname{div} \sigma \nabla \phi = 0$ simplifies to

$$-\frac{1}{r^2} \frac{\partial}{\partial \varphi} \left(\sigma \frac{\partial \phi}{\partial \varphi} \right) = 0 \quad \text{on } \Omega.$$

As a solution we obtain

$$\phi = C_1 \varphi \quad \text{and} \quad \nabla \phi = \frac{C_1}{r} \mathbf{e}_\varphi, \quad (3.19)$$

where the constant C_1 is chosen to satisfy the boundary condition (3.16), i. e. $C_1 = u(t)/2\pi$. The prescribed voltage in the inductor is denoted by a time dependent function $u(t)$. If for example the voltage is harmonic with a fixed single frequency f , then $u(t) = u_{\max} \cos(2\pi f t)$. Transforming the solution (3.19) back to cartesian coordinates, the following expression for the source current density $\mathbf{J}_{\text{src}} = -\sigma \nabla \phi$ is obtained

$$\mathbf{J}_{\text{src}}(x, t) = \sigma \frac{u(t)}{2\pi} \mathbf{J}_0(x) \quad (3.20)$$

with a geometric form function

$$\mathbf{J}_0(x) = - \begin{pmatrix} \frac{-y}{x^2+y^2} \\ \frac{x}{x^2+y^2} \\ 0 \end{pmatrix} \quad \text{on } \Omega \quad (3.21)$$

and equal to zero on $D \setminus \Omega$.

In technical applications, usually the current is controlled. Therefore, also the case of a prescribed inductor current $i(t)$ is considered. The current through a cross section Γ of any conductor is determined as the integral of the current density in normal direction, i. e.

$$i(t) = \int_{\Gamma} \mathbf{J} \cdot \mathbf{n} \, da = \int_{\Gamma} \sigma \nabla \phi \cdot \mathbf{n} \, da. \quad (3.22)$$

With this condition it is possible to determine the current density $\mathbf{J} = -\sigma \nabla \phi$ in the inductor from the solution of (3.19) also in the case of a given inductor current (that combines the impressed and the self-induced current). For this we assume that the inductor has a rectangular cross section with inner radius r_i , outer radius r_a and height h . Then by equations (3.19) and (3.22) there holds

$$\mathbf{J}(x, t) = i(t) \frac{\log(r_i/r_a)}{h} \mathbf{J}_0(x) \quad \text{in } \Omega \quad (3.23)$$

with $\mathbf{J}_0(x)$ given by (3.21).

As we have seen from the considerations above, in both cases, voltage or current control, the source current density can be written in the form

$$\mathbf{J}_{\text{src}}(x, t) = j(t) \mathbf{J}_0(x) \quad (3.24)$$

with a time dependent function $j(t)$.

In the case of multifrequency induction hardening with a prescribed inductor current, the current density \mathbf{J} consists of the superimposed medium and high frequency parts of the source current. Assume for simplicity a harmonic source current, then

$$\mathbf{J}(x, t) = (p_{\text{mf}}(t)I_{\text{mf}} \cos(2\pi f_{\text{mf}}t) + p_{\text{hf}}(t)I_{\text{hf}} \cos(2\pi f_{\text{hf}}t)) \frac{\log(r_i/r_a)}{h} \mathbf{J}_0(x) \quad (3.25)$$

in the inductor, where $I_{\text{mf/hf}}$ denote the maximum amplitudes of the MF and HF current. By $p_{\text{mf/hf}}(t) \in [0, 1]$ we denote a relative fraction of the medium and high frequency current, that corresponds to the relative power that is used as a control parameter for the induction hardening machine. In general, the inductor current is periodic but not necessarily harmonic. We account for this fact by considering the vector potential equation in the time domain instead of the usually used harmonic approach that is limited to harmonic excitations.

3.2. Phase fraction of austenite

During the heating process only the formation of the high temperature phase austenite is of interest. The volume fraction of austenite is given by the variable $z(x, t)$ with $z \in [0, 1]$. The initial microstructure is in general not known. It might be a phase mixture consisting of ferrite, martensite, pearlite or bainite. Its volume fraction is denoted by $z_0(x, t)$. The initial state and austenite always sum up to one such that $z_0 = 1 - z$. It is assumed that the transformation kinetics can be described by a rate law in the form of a Leblond-Devaux-law [49], which we use in the following generalized form [38],

$$\begin{aligned} \partial_t z(t) &= \frac{z^{r(\theta)}}{\tau(\theta)} [z_{\text{eq}}(\theta) - z]^+ \\ z(0) &= 0. \end{aligned} \quad (3.26)$$

With $[\cdot]^+$ the positive part of a function is denoted. The parameters $r(\theta)$, $z_{\text{eq}}(\theta)$ and $\tau(\theta)$ denote material dependent functions, that have to be determined from experimental measurements or fits to TTT/TTA diagrams like Figure 2.3 and 2.4. In order to reduce the complexity, the temperature dependence of r might be ignored. The rate law (3.26) does not depend explicitly on the space coordinate x . The spatial dependence of the phase fraction of austenite is only introduced by the spatial dependence of the temperature θ .

In the case of induction hardening, one has to deal with very short heating times and consequently, very high heating rates. Referring to literature, measurements for short time austenitization were performed by Miokovic, [54]. Their approach to model the phase transformation behaviour is based on a generalized Johnson-Mehl-Avrami equation [2, 44], which is given in the form

$$\partial_t z(t) = nC \exp\left(-\frac{\Delta H}{k\theta}\right) \ln\left(\frac{1}{1-z}\right)^{\frac{n-1}{n}} (1-z).$$

The constant $k = 8.617 \cdot 10^{-5}$ eV/K denotes the Boltzmann constant. Further parameters were determined as $n = 1.525$, $C = 2.84 \cdot 10^{20} \text{ s}^{-1}$ and $\Delta H = 4.185$ eV.

Introducing a linearization of the logarithm, i. e. $-\ln(1-z) \approx z$, the rate law above fits into the general form of equation (3.26).

3.3. Balance of energy

In order to determine the temperature distribution in the workpiece Σ we consider the balance of energy. The temperature distribution in the surrounding air and in the induction coil is not considered. In practical applications, the inductor is cooled. Simulating the cooling process is a complicated task and out of scope of this thesis.

The balance of internal energy is given by the following equation

$$\rho \frac{\partial e}{\partial t} + \operatorname{div} \mathbf{q} = Q \quad \text{in } \Sigma, \quad (3.27)$$

where ρ denotes the constant density¹, e the specific internal energy of the system, \mathbf{q} the heat flux and Q the heat source, which results as the Joule heat

$$Q = \mathbf{J} \cdot \mathbf{E} = \sigma |\partial_t \mathbf{A}|^2.$$

In order to ensure thermodynamic consistency of the model, we assume that the Second Law of Thermodynamics (2nd law) is satisfied. It states the existence of a pair of quantities, the specific entropy s and the entropy flux φ , that are connected by a balance equation

$$\rho \frac{\partial s}{\partial t} + \operatorname{div} \varphi = \zeta,$$

where ζ denotes the entropy production [56]. The statement of the 2nd law is that the entropy production is nonnegative for every thermodynamic process, i. e. for every solution of the underlying partial differential equations,

$$\zeta \geq 0.$$

In order to evaluate the 2nd law, we introduce the Helmholtz free energy as thermodynamic potential

$$\psi = e - \theta s.$$

The temperature θ and the volume fraction of austenite z are the unknown fields of interest. It is assumed that the free energy depends on these quantities such that there exists a representation $\psi = \psi(\theta, z)$. The time derivative of ψ is given by

$$\partial_t \psi = \partial_t e - s \partial_t \theta - \theta \partial_t s \quad \text{and} \quad \partial_t \psi = \frac{\partial \psi}{\partial \theta} \partial_t \theta + \frac{\partial \psi}{\partial z} \partial_t z. \quad (3.28)$$

Introducing the entropy balance into (3.28)₁ yields

$$\theta \zeta = \rho \partial_t e - \rho \partial_t \psi - \rho s \partial_t \theta + \theta \operatorname{div} \varphi.$$

¹The workpiece Σ is modelled as an incompressible rigid body, mechanical displacements and stresses resulting from thermal expansion, transformation induced plasticity or external forces are ignored. Therefore, the density is constant.

With the balance of internal energy and (3.28)₂ we obtain the following expression for the entropy inequality

$$\theta\zeta = \sigma |\partial_t \mathbf{A}|^2 - \frac{\mathbf{q}}{\theta} \nabla \theta - \rho \frac{\partial \psi}{\partial \theta} \partial_t \theta - \rho \frac{\partial \psi}{\partial z} \partial_t z - \rho s \partial_t \theta - \theta \operatorname{div} \frac{\mathbf{q}}{\theta} + \theta \operatorname{div} \boldsymbol{\varphi} \geq 0. \quad (3.29)$$

For simple, incompressible bodies, the entropy flux is given as

$$\boldsymbol{\varphi} = \frac{\mathbf{q}}{\theta}.$$

Then, the last two terms drop out of expression (3.29). The remaining inequality has to hold for every thermodynamic process, i. e. for all solutions of the underlying partial differential equations. Assume we have a solution with homogeneous temperature, constant phase fraction z and vanishing magnetic potential but arbitrary $\partial_t \theta$. Then in order to not violate inequality (3.29), there has to hold the following relation, which is standard in literature,

$$s = - \frac{\partial \psi}{\partial \theta}. \quad (3.30)$$

With this relation, inequality (3.29) has the form

$$\theta\zeta = \sigma |\partial_t \mathbf{A}|^2 - \frac{\mathbf{q}}{\theta} \nabla \theta - \rho \frac{\partial \psi}{\partial z} \partial_t z \geq 0.$$

The Joule heat is a nonnegative quantity. The remaining terms have a product structure. In order to not violate the entropy inequality, we assume that the heat flux is given by Fourier's law

$$\mathbf{q} = -\kappa \nabla \theta \quad (3.31)$$

with $\kappa > 0$ denoting the positive heat conductivity. Furthermore, we assume that there exists a quantity $\Xi > 0$ such that

$$\partial_t z = -\Xi \frac{\partial \psi}{\partial z}. \quad (3.32)$$

With the definition of the specific heat at constant volume, $c_V = \theta \partial s / \partial \theta$, and the definition of the latent heat, $\mathcal{L} = \partial e / \partial z$, we compute for the time derivative of the internal energy

$$\partial_t e = c_V \partial_t \theta + \mathcal{L} \partial_t z.$$

The balance of internal energy becomes finally

$$\rho c_V \partial_t \theta - \operatorname{div} \kappa \nabla \theta = \sigma |\partial_t \mathbf{A}|^2 - \rho \mathcal{L} \partial_t z \quad \text{in } \Sigma \quad \text{and } t \in (0, T). \quad (3.33)$$

Remark 3.1. *In the energy balance above, the specific heat at constant volume, c_V , appears. From a practical point of view, this quantity is hard to measure. Experiments are usually carried out at constant pressure, such that the specific heat at constant pressure, c_p , is an accessible quantity. The specific heat capacity denotes the energy that is necessary to heat up a material by 1 K. In the case of constant pressure,*

energy is also required for the volumetric change of the body due to thermal expansion. Therefore, there holds $c_p > c_V$. For solid materials, the difference $c_p - c_V$ is small. In addition, we model the workpiece as incompressible body and ignore deformations due to thermal expansion and volumetric changes due to the phase transition. In this case it is assumed that $c_V = c_p$.

Remark 3.2. With $e = \psi - \theta s$ and (3.30) the latent heat can be related directly to the free energy ψ by

$$\mathcal{L}(\theta, z) = \frac{\partial e}{\partial z} = \frac{\partial \psi}{\partial z} - \theta \frac{\partial s}{\partial z} = \frac{\partial \psi}{\partial z} - \theta \frac{\partial^2 \psi}{\partial \theta \partial z}. \quad (3.34)$$

Using relation (3.32) it is possible to get an explicit formulation for the latent heat, that is related to the evolution equation for the volume fraction z . The positive quantity Ξ can be used to adapt the in general nonlinear expression for the latent heat

$$\mathcal{L}(\theta, z) = \frac{\partial \psi}{\partial z} - \theta \frac{\partial^2 \psi}{\partial \theta \partial z} = -\Xi^{-1} \frac{z^r}{\tau} [z_{eq} - z]^+ + \Xi^{-1} \frac{\partial}{\partial \theta} \left(\frac{z^r}{\tau} [z_{eq} - z]^+ \right)$$

to thermodynamic measurements.

Next, we consider the boundary conditions for the temperature. In general, at the boundary of the workpiece $\partial\Sigma$ there occur heat losses due to radiation and convection. This can be described by the following general boundary condition

$$-\kappa \nabla \theta \cdot \mathbf{n} = \alpha(\theta^4 - \theta_0^4) + \eta(\theta - \theta_0) \quad \text{on} \quad \partial\Sigma.$$

Here, α denotes the radiation coefficient, η the heat transfer coefficient and θ_0 the ambient temperature. To be precise, α is the product of the Stefan Boltzmann constant $\sigma = 5.6710^{-8} \text{ W/m}^2\text{K}^4$ and the material emissivity coefficient $\epsilon \in [0, 1]$.

If we compare the energy of the heat radiation to the heat energy that is generated in the workpiece due to the eddy currents, we observe that the radiation energy is by magnitudes smaller. Typically, in applications of induction hardening the necessary surface energy density lies in the range of about $0.5 - 15 \text{ kW/cm}^2$. Estimating the losses due to radiation with a surface temperature of $\theta = 1073 \text{ K}$ and $\epsilon = 1$, which is an overestimation, since the surface is not black, gives an approximate loss of 7.5 W/cm^2 . Consequently, it is justified to neglect losses due to radiation. Finally, we assume a Robin type boundary condition for the temperature at the surface of the workpiece $\partial\Sigma$ in the following form

$$\kappa \nabla \theta \cdot \mathbf{n} + \eta \theta = g \quad \text{on} \quad \partial\Sigma, \quad (3.35)$$

where $g = \eta \theta_0$ denotes a given function.

3.4. Characterization of the material parameters

In general, the material parameters are temperature dependent and they are different for each material and also for each phase. Therefore, they depend on the space x , the

phase z and on the temperature θ . In addition, in ferromagnetic materials such as steel, the magnetic permeability admits a nonlinear behaviour with respect to the magnetic field \mathbf{H} . This nonlinear dependence is expressed by the nonlinear magnetization curve $\mathbf{B} = f(\mathbf{H})$, see e. g. Figure A.4. The magnetic permeability μ [Vs/Am] is then defined by the relation

$$\mathbf{B} = f(\mathbf{H}, \theta) = \mu(|\mathbf{H}|, \theta)\mathbf{H} \quad \text{such that} \quad \mu(|\mathbf{H}|, \theta) = \frac{f(|\mathbf{H}|, \theta)}{|\mathbf{H}|}.$$

The material parameters are characterized as follows. For the electrical conductivity σ [Am/Vmm²] we assume

$$\sigma(x, \theta, z) = \begin{cases} \sigma_{\text{wp}}(\theta, z) & x \in \Sigma \\ \sigma_{\text{Cu}} & x \in \Omega \\ 0 & x \in D \setminus (\Omega \cup \Sigma) \end{cases} \quad (3.36)$$

with σ_{wp} the electrical conductivity of the workpiece and σ_{Cu} denoting the conductivity of the inductor. The magnetic permeability μ is characterized by

$$\mu(x, \theta, z) = \begin{cases} \mu_0 \mu_r(|\mathbf{H}|, \theta, z) & x \in \Sigma \\ \mu_0 & x \in D \setminus \Sigma, \end{cases} \quad (3.37)$$

where $\mu_0 = 4\pi \cdot 10^{-7}$ Vs/Am denotes the permeability of vacuum and μ_r the relative permeability. It is assumed that the magnetization curve $f(\mathbf{H}, \theta)$ is strictly monotone with respect to \mathbf{H} , such that it is possible to express μ_r also as a function of $|\mathbf{B}|$.

The specific heat capacity c_p [J/kgK] as well as the heat conductivity κ [W/mK] are only defined in the workpiece Σ . In general there holds

$$c_p = c_p(\theta, z) \quad \text{and} \quad \kappa = \kappa(\theta, z). \quad (3.38)$$

The material parameters are given in Appendix A.2.

3.5. Summary of the model

We summarize the model describing the induction heating of workpieces made of steel. We search for the fields $\mathbf{A}(x, t)$, $\theta(x, t)$ and $z(x, t)$ such that the following differential equations are satisfied

$$\begin{aligned} \sigma \frac{\partial \mathbf{A}}{\partial t} + \text{curl} \frac{1}{\mu} \text{curl} \mathbf{A} &= \mathbf{J}_{\text{src}} && \text{in } D \times (0, T) \\ \rho c_p \frac{\partial \theta}{\partial t} - \text{div} \kappa \nabla \theta &= \sigma \left| \frac{\partial \mathbf{A}}{\partial t} \right|^2 - \rho \mathcal{L} \frac{\partial z}{\partial t} && \text{in } \Sigma \times (0, T) \\ \frac{\partial z}{\partial t} &= \frac{z^{r(\theta)}}{\tau(\theta)} [z_{\text{eq}}(\theta) - z]^+ && \text{in } \Sigma \times (0, T). \end{aligned} \quad (3.39)$$

As boundary conditions, we impose

$$\begin{aligned} \mathbf{A} \times \mathbf{n} &= 0 & \text{on } \partial D \\ \kappa \nabla \theta \cdot \mathbf{n} + \eta \theta &= g & \text{on } \partial \Sigma. \end{aligned} \tag{3.40}$$

The model is completed by initial conditions

$$\begin{aligned} \mathbf{A}(x, 0) &= \mathbf{A}_0(x) & \text{in } D \\ \theta(x, 0) &= \theta_0(x) & \text{in } \Sigma \\ z(0) &= 0 & \text{in } \Sigma. \end{aligned} \tag{3.41}$$

In the next chapter, analytical investigations to show existence and uniqueness of a simplified model are carried out. In contrast to (3.39–3.41) it is assumed that the material parameters depend only on the space x and the phase z , but not on the temperature θ . The numerical simulation algorithm for the full model (3.39–3.41) together with various examples of induction hardening of discs and gears is presented in Chapters 5 and 6.

Chapter 4.

Analysis of a simplified model

Introduction

In this chapter, the analysis of a simplified model is considered. We show well-posedness of the problem and derive regularity results for solutions of a weak formulation of system (3.39) with modified material parameters. For simplicity it will be assumed that all material parameters are independent of the temperature θ such that they only depend on the space x and the phase fraction of austenite z . Furthermore, the nonlinearity in the magnetic permeability μ is ignored. Within this chapter, partial derivatives will be denoted by a subscript index to simplify the notation, e. g. $\partial \mathbf{A} / \partial t = \mathbf{A}_t$. The main part of this chapter has been published in [39].

4.1. Notation and preliminary assumptions

We consider the geometric setting as introduced in Chapter 3, cf. Figure 3.2, with $D \subset \mathbb{R}^3$ denoting the hold all domain containing the inductor coil Ω and the workpiece Σ . It is assumed that $\bar{\Omega} \subset D$, $\bar{\Sigma} \subset D$, $\bar{\Omega} \cap \bar{\Sigma} = \emptyset$ and $\partial\Omega$, $\partial\Sigma$, ∂D are of class $C^{1,1}$. We call $G = \Omega \cup \Sigma$ the set of conductors and define the space-time domain as $Q = \Sigma \times (0, T)$.

The simplified material parameters are characterized as follows. It is assumed that the electrical conductivity σ and the magnetic permeability μ are sufficiently regular and bounded from below and above. They may depend both on the spatial variables and also on the phase parameter z but not on the temperature θ as in the general setting:

$$\sigma(x, z) = \begin{cases} \sigma_{\text{wp}}(z), & x \in \Sigma, \\ \sigma_{\text{Cu}}, & x \in \Omega, \\ 0, & x \in D \setminus G, \end{cases} \quad (4.1)$$

with its derivative with respect to the z -variable

$$\sigma_z(x, z) = \begin{cases} \sigma'_{\text{wp}}(z), & x \in \Sigma, \\ 0, & x \in D \setminus \Sigma, \end{cases} \quad (4.2)$$

and

$$\mu(x, z) = \begin{cases} \mu_{\text{wp}}(z), & x \in \Sigma, \\ \mu_0, & x \in D \setminus \Sigma. \end{cases} \quad (4.3)$$

with

$$\mu_z(x, z) = \begin{cases} \mu'_{\text{wp}}(z), & x \in \Sigma, \\ 0, & x \in D \setminus \Sigma. \end{cases} \quad (4.4)$$

The specific heat and the heat conductivity are assumed to be constant. For simplicity, we take $r = 0$ in the rate law describing the evolution of the phase fraction.

In the following sections we will study the well-posedness for the Cauchy system associated to a suitable variational formulation of the simplified model to describe the induction heating process. For completeness, we repeat the system of partial differential equations of the reduced problem

$$\begin{aligned} \sigma \mathbf{A}_t + \operatorname{curl} \mu^{-1} \operatorname{curl} \mathbf{A} &= \mathbf{J}_{\text{src}} && \text{in } D \times (0, T) \\ \rho c_p \theta_t - \operatorname{div} \kappa \nabla \theta &= \sigma |\mathbf{A}_t|^2 - \rho \mathcal{L} z_t && \text{in } \Sigma \times (0, T) \\ z_t &= \frac{1}{\tau(\theta)} [z_{\text{eq}}(\theta) - z]^+ && \text{in } \Sigma \times (0, T) \end{aligned} \quad (4.5)$$

supplemented with boundary and initial conditions

$$\begin{aligned} \mathbf{A} \times \mathbf{n} &= 0 && \text{on } \partial D \\ \kappa \nabla \theta \cdot \mathbf{n} + \eta \theta &= g && \text{on } \partial \Sigma \\ \mathbf{A}(x, 0) &= \mathbf{A}_0(x) && \text{in } D \\ \theta(x, 0) &= \theta_0(x) && \text{in } \Sigma \\ z(0) &= 0 && \text{in } \Sigma. \end{aligned} \quad (4.6)$$

In order to derive the weak formulation of the Cauchy problem, we recall the definitions of the generalized curl and div operators. For this, we introduce the following notation. Let us denote with the symbol \mathbb{W} the vector-valued counterpart of the Banach space W . We use the symbol $\mathbb{L}^q(U \times (0, t))$ for the space $L^q(0, t; \mathbb{L}^q(U))$, for every $q \in [1, +\infty)$, $t \in (0, T]$ and $U \subset \mathbb{R}^3$ a bounded domain of class $C^{1,1}$. Let $p \in (1, +\infty)$ and $\boldsymbol{\psi} \in \mathbb{L}^p(D)$, then, we write $\operatorname{curl} \boldsymbol{\psi} \in \mathbb{L}^p(D)$ if there exists $\boldsymbol{\xi} \in \mathbb{L}^p(D)$ such that

$$\int_D \boldsymbol{\psi} \operatorname{curl} \phi \, dx = \int_D \boldsymbol{\xi} \phi \, dx \quad \text{for all } \phi \in C_c^\infty(D).$$

We define $\operatorname{curl} \boldsymbol{\psi} := \boldsymbol{\xi}$ as the uniquely determined vector $\boldsymbol{\xi}$. Analogously, we write $\operatorname{div} \boldsymbol{\psi} \in L^p(D)$ if there exists $\zeta \in L^p(D)$ such that

$$\int_D \boldsymbol{\psi} \cdot \nabla \eta \, dx = - \int_D \zeta \eta \, dx \quad \text{for all } \eta \in C_c^\infty(D).$$

We define $\operatorname{div} \boldsymbol{\psi} := \zeta$ as the uniquely determined element ζ . Then, we introduce the Banach spaces (with the graph norms)

$$\mathbb{L}_{\operatorname{curl}}^p(D) = \{\boldsymbol{\psi} \in \mathbb{L}^p(D) : \operatorname{curl} \boldsymbol{\psi} \in \mathbb{L}^p(D)\}$$

and

$$\mathbb{L}_{\text{div}}^p(D) = \{\boldsymbol{\psi} \in \mathbb{L}^p(D) : \text{div } \boldsymbol{\psi} \in L^p(D)\}.$$

For $\boldsymbol{\psi} \in \mathbb{L}_{\text{curl}}^2(D)$ we define the linear bounded trace operator $\gamma_\tau(\boldsymbol{\psi})$ using the well-known Green's formula (cf. e. g. [25])

$$\int_D \boldsymbol{\psi} \cdot \text{curl } \phi \, dx - \int_D \text{curl } \boldsymbol{\psi} \cdot \phi \, dx = - \int_{\partial D} (\mathbf{n} \times \boldsymbol{\psi}) \cdot \phi \, ds =: \langle \gamma_\tau(\boldsymbol{\psi}), \phi \rangle, \quad (4.7)$$

for all $\phi \in \mathbb{H}^1(D)$, where (with an abuse of notation) the integral over ∂D has to be understood as the duality between $\mathbb{H}^{-1/2}(\partial D)$ and $\mathbb{H}^{1/2}(\partial D)$ and \mathbf{n} denotes the outward unit normal vector to ∂D . Similarly, for $\boldsymbol{\psi} \in \mathbb{L}_{\text{div}}^2(D)$ we introduce the linear bounded trace operator $\gamma_n(\boldsymbol{\psi})$ by the Green's formula

$$\int_D \boldsymbol{\psi} \cdot \nabla \phi \, dx + \int_D \text{div } \boldsymbol{\psi} \phi \, dx = \int_{\partial D} (\mathbf{n} \cdot \boldsymbol{\psi}) \phi \, ds =: \langle \gamma_n(\boldsymbol{\psi}), \phi \rangle, \quad (4.8)$$

for all $\phi \in H^1(D)$, where (with an abuse of notation) the integral over ∂D has to be understood as the duality between $H^{-1/2}(\partial D)$ and $H^{1/2}(\partial D)$. Finally, we introduce the Hilbert space

$$\mathbb{X} = \{\mathbf{v} \in \mathbb{L}_{\text{curl}}^2(D) : \text{div } \mathbf{v} = 0 \quad \text{and} \quad \gamma_\tau(\mathbf{v}) = 0\}.$$

Notice that, since $\partial D \in C^{1,1}$ the space \mathbb{X} equipped with the norm

$$\|\mathbf{v}\|_{\mathbb{X}} = \|\text{curl } \mathbf{v}\|_{\mathbb{L}^2(D)}$$

is a closed subspace of $\mathbb{H}^1(D)$. Moreover, let us notice that, from the Green's formula it follows that: if $\mathbf{A} \in \mathbb{X}$, then $\gamma_n(\mathbf{A}) = 0$. Indeed, if we denote by $\mathbf{w} = \text{curl } \mathbf{A} \in \mathbb{L}^2(D)$, then $\text{div } \mathbf{w} = 0$ and $\gamma_n(\mathbf{w}) \in H^{-1/2}(\partial D)$. Moreover the following Green's formulas hold true for every test function $\phi \in H^1(D)$:

$$\begin{aligned} \langle \gamma_n(\mathbf{w}), \phi \rangle &= \int_D (\text{div } \mathbf{w} \phi + \mathbf{w} \cdot \nabla \phi) \, dx = \int_D \text{curl } \mathbf{A} \cdot \nabla \phi \, dx \\ &= \int_D \text{curl } \mathbf{A} \cdot \nabla \phi - \mathbf{A} \cdot \text{curl } \nabla \phi \, dx \\ &= \langle \gamma_\tau(\mathbf{A}), \nabla \phi \rangle. \end{aligned} \quad (4.9)$$

Hence, if $\mathbf{A} \in \mathbb{X}$, then $\gamma_n(\text{curl } \mathbf{A}) = 0$ (cf. e. g. [30, Chapter 2]).

The following results are necessary to obtain the regularity results. The first one is an embedding result that is a consequence of [32, Thm. 3.3]. The complete proof of a more general result can be found in [22, Prop. 2.2].

Lemma 4.1. *Let $U \subset \mathbb{R}^3$ be a bounded C^1 domain, then the space*

$$\mathcal{W}^{p,\alpha}(U) = \{\mathbf{u} \in \mathbb{L}_{\text{curl}}^p(U) \cap \mathbb{L}_{\text{div}}^p(U) : \gamma_n(\mathbf{u}) \in L^\alpha(\partial U)\}$$

continuously embeds in the space $\mathbb{L}^\xi(U)$ for $\xi := \min\{\frac{3\alpha}{2}, p^\}$, where p^* is the Sobolev embedding exponent*

$$p^* := \begin{cases} \frac{3p}{3-p} & \text{if } 1 \leq p < 3, \\ s \in [1, +\infty) & \text{if } p = 3, \\ +\infty & \text{if } p > 3. \end{cases}$$

Moreover, we recall the following interpolation inequality, holding true for $p, q, r \in [1, +\infty]$, with $p < r < q$, $1/r = \alpha/p + (1 - \alpha)/q$, $\alpha \in (0, 1)$, and $\mathbf{v} \in \mathbb{L}^q(D)$:

$$\|\mathbf{v}\|_{\mathbb{L}^r(D)} \leq \|\mathbf{v}\|_{\mathbb{L}^p(D)}^\alpha \|\mathbf{v}\|_{\mathbb{L}^q(D)}^{1-\alpha}. \quad (4.10)$$

Now, we precisely state the assumptions on the data.

4.2. Hypotheses

We list here our basic assumptions on the functions σ , μ , \mathbf{J}_0 , j , τ , and z_{eq} in (4.5), where we take the constants c_p , κ and η equal to 1, for simplicity.

Hypothesis (H). *Assume that*

- (i) $\sigma(x, z) : \overline{D} \times [0, 1] \rightarrow \mathbb{R}$ is a piecewise continuous and Lipschitz continuous (w.r.t. z for almost all $x \in D$) function defined in (4.1) and (4.2), where $\sigma_{\text{wp}} \in C^{1,1}([0, 1])$, $\sigma_{\text{Cu}} \in \mathbb{R}^+$. Assume moreover that there exist two constants $0 < \underline{\sigma} \leq \overline{\sigma}$ such that

$$\underline{\sigma} \leq \sigma(x, z) \leq \overline{\sigma} \quad \text{in } \overline{D} \times [0, 1];$$

- (ii) $\mu(x, z) : \overline{D} \times [0, 1] \rightarrow \mathbb{R}$ is a piecewise continuous and Lipschitz continuous (w.r.t. z for almost all $x \in D$) function defined in (4.3), (4.4), where $\mu_{\text{wp}} \in C^{1,1}([0, 1])$, $\mu_0 \in \mathbb{R}^+$. Assume moreover that there exist two constants $0 < \underline{\mu} \leq \overline{\mu}$ such that

$$\underline{\mu} \leq \mu(x, z) \leq \overline{\mu} \quad \text{in } \overline{D} \times [0, 1];$$

- (iii) $j \in H^1(0, T)$, $\mathbf{J}_0 : D \rightarrow \mathbb{R}^3$ is an $\mathbb{L}_{\text{curl}}^2(D)$ -function defined in (3.21);

- (iv) $\tau, z_{\text{eq}} \in C^2(\mathbb{R})$, $\mathcal{L} \in C^{0,1}(\mathbb{R} \times [0, 1])$ and there exist positive constants $0 < \tau_* \leq \tau^*$, $M > 0$ and $C_L > 0$ such that

$$\begin{aligned} \tau_* \leq \tau(\theta) \leq \tau^*, \quad 0 \leq z_{\text{eq}}(\theta) \leq 1 \quad \text{for all } \theta \in \mathbb{R}, \quad \|\tau\|_{C^2(\mathbb{R})} \leq M, \quad \|z_{\text{eq}}\|_{C^2(\mathbb{R})} \leq M, \\ \text{and } |\mathcal{L}(\theta, z)| \leq C_L \quad \text{for all } (\theta, z) \in \mathbb{R} \times [0, 1]; \end{aligned}$$

- (v) $g \in L^\infty(0, T; L^\infty(\partial\Sigma))$;

(vi) $\mathbf{A}_0 \in \mathbb{X} \cap \mathbb{H}^3(D)$, $\theta_0 \in W^{2,5/3}(\Sigma)$.

With these preliminary assumptions we are now able to derive the weak formulation for problem (4.5) and state the main result on the well-posedness and the stability estimates. The analytical results are presented in Section 4.3. The proofs are carried out in Section 4.4.

4.3. Weak formulation and main theorem

We will now state the weak formulation of the Cauchy problem (4.5), (4.6), (3.24) and (3.34).

Problem (P). *Find a triple (\mathbf{A}, θ, z) with the regularity properties*

$$\mathbf{A} \in H^2(0, T; \mathbb{L}^2(D)) \cap W^{1,\infty}(0, T; \mathbb{X}), \quad \text{curl } \mathbf{A} \in L^\infty(0, T; \mathbb{L}^6(D)), \quad (4.11)$$

$$\theta \in W^{1,5/3}(0, T; L^{5/3}(\Sigma)) \cap L^{5/3}(0, T; W^{2,5/3}(\Sigma)) \cap L^2(0, T; H^1(\Sigma)) \cap L^\infty(Q), \quad (4.12)$$

$$z \in W^{1,\infty}(0, T; W^{1,\infty}(\Sigma)), \quad 0 \leq z < 1 \text{ a.e. in } Q, \quad (4.13)$$

solving the following system

$$\int_G \sigma(x, z) \mathbf{A}_t \cdot \mathbf{v} \, dx + \int_D \frac{1}{\mu(x, z)} \text{curl } \mathbf{A} \cdot \text{curl } \mathbf{v} \, dx = \int_\Omega j(t) \mathbf{J}_0(x) \cdot \mathbf{v} \, dx \quad (4.14)$$

for all $\mathbf{v} \in \mathbb{X}$, a.e. in $(0, T)$,

$$\theta_t - \Delta \theta = -\mathcal{L}(\theta, z) z_t + \sigma(x, z) |\mathbf{A}_t|^2 \quad \text{a.e. in } Q, \quad (4.15)$$

$$z_t = \frac{1}{\tau(\theta)} [z_{eq}(\theta) - z]^+ \quad \text{a.e. in } Q, \quad (4.16)$$

$$\mathbf{A} \times \mathbf{n} = 0 \quad \text{a.e. on } \partial D \times (0, T), \quad \nabla \theta \cdot \mathbf{n} + \theta = g \quad \text{a.e. on } \partial \Sigma \times (0, T), \quad (4.17)$$

$$\mathbf{A}(0) = \mathbf{A}_0 \quad \text{a.e. in } D, \quad \theta(0) = \theta_0, \quad z(0) = 0 \quad \text{a.e. in } \Sigma \quad (4.18)$$

and satisfying the following estimate

$$\begin{aligned} & \|\mathbf{A}\|_{H^2(0, T; \mathbb{L}^2(D)) \cap W^{1,\infty}(0, T; \mathbb{X})} + \|\text{curl } \mathbf{A}\|_{L^\infty(0, T; \mathbb{L}^6(D))} \\ & + \|\theta\|_{W^{1,5/3}(0, T; L^{5/3}(\Sigma)) \cap L^{5/3}(0, T; W^{2,5/3}(\Sigma)) \cap L^2(0, T; H^1(\Sigma)) \cap L^\infty(Q)} \\ & + \|z\|_{W^{1,\infty}(0, T; W^{1,\infty}(\Sigma))} \leq S, \end{aligned} \quad (4.19)$$

where the constant S depends on the data of the problem.

The main result is stated in the following theorem.

Theorem 1. *Let Hypothesis (H) hold true. Then, there exists a unique solution to Problem (P). Moreover, if we denote by $(\mathbf{A}_i, \theta_i, z_i)$, $i = 1, 2$, two triples of solutions corresponding to data $(\mathbf{A}_{0,i}, \theta_{0,i}, j_i)$, then, there exists a positive constant $C = C(S)$ (cf. estimate (4.19)) such that the following stability estimate holds true*

$$\begin{aligned}
& \|(\mathbf{A}_1 - \mathbf{A}_2)(t)\|_{\mathbb{L}^2(D)}^2 + \|\operatorname{curl}(\mathbf{A}_1 - \mathbf{A}_2)\|_{\mathbb{L}^2(D \times (0,T))}^2 \\
& + \|\partial_t(\mathbf{A}_1 - \mathbf{A}_2)(t)\|_{\mathbb{L}^2(D)}^2 + \|\operatorname{curl}(\partial_t(\mathbf{A}_1 - \mathbf{A}_2))\|_{\mathbb{L}^2(D \times (0,T))}^2 \\
& + \|(\theta_1 - \theta_2)(t)\|_{L^2(\Sigma)}^2 + \|\theta_1 - \theta_2\|_{L^2(0,T;H^1(\Sigma))}^2 \\
& + \|(z_1 - z_2)(t)\|_{H^1(\Sigma)}^2 + \|\partial_t(z_1 - z_2)\|_{L^2(0,T;H^1(\Sigma))}^2 \\
& \leq C \left(\|\mathbf{A}_{0,1} - \mathbf{A}_{0,2}\|_{\mathbb{X}}^2 + \|(\partial_t(\mathbf{A}_1 - \mathbf{A}_2))(0)\|_{\mathbb{L}^2(D)}^2 + \|\theta_{0,1} - \theta_{0,2}\|_{L^2(\Sigma)}^2 \right. \\
& \left. + \|j_1 \mathbf{J}_0 - j_2 \mathbf{J}_0\|_{L^2(0,T)}^2 + \|j'_1 \mathbf{J}_0 - j'_2 \mathbf{J}_0\|_{L^2(0,T)}^2 \right) \quad \text{for all } t \in [0, T].
\end{aligned} \tag{4.20}$$

4.4. Proof of the existence result

In this section we prove Theorem 1 in three steps: first, we prove local existence of solutions by means of Schauder fixed point argument. Secondly, we prove the global a priori estimates necessary in order to extend the solution to the whole time interval $[0, T]$. Finally, we prove the stability estimate (4.20) entailing, in particular, uniqueness of the solution to Problem (P).

4.4.1. Existence of a (local in time) solution

We start the proof by solving (locally in time) Problem (P) by means of a standard fixed point argument of Schauder type.

For a fixed $T_0 \in (0, T]$ (which shall be specified later on) and a fixed constant $R > 0$, let us introduce the space

$$\mathbb{O} = \{\theta \in L^2(0, T_0; L^2(\Sigma)) : \|\theta\|_{L^2(0, T_0; L^2(\Sigma))} \leq R\}.$$

In the following, we shall construct an operator \mathcal{T} , which maps \mathbb{O} onto itself for a suitable time $0 < T_0 \leq T$, in such a way that any fixed point of \mathcal{T} yields a solution to Problem (P). We shall prove that \mathcal{T} is compact and continuous w.r.t. the topology of $L^2(0, T_0; L^2(\Sigma))$. Hence, by the Schauder theorem \mathcal{T} admits (at least) a fixed point θ in \mathbb{O} , whence the existence of a solution (\mathbf{A}, θ, z) to the Cauchy Problem (P) on the interval $[0, T_0]$. Finally, the (local) uniqueness result will be a consequence of the stability estimate (4.44) below.

Definition of the fixed point map \mathcal{T} . We construct the operator \mathcal{T} in this way: given $\bar{\theta} \in \mathbb{O}$, the operator

$$\begin{aligned}
\mathcal{T} : \mathbb{O} & \rightarrow L^{5/3}(0, T; W^{2,5/3}(\Sigma)) \cap W^{1,5/3}(0, T; L^{5/3}(\Sigma)) \\
\mathcal{T} : \bar{\theta} & \mapsto \theta \quad \text{where } \theta \text{ solves}
\end{aligned}$$

$$\theta_t - \Delta\theta = -\mathcal{L}(\bar{\theta}, z)z_t + \sigma(x, z)|\mathbf{A}_t|^2 \quad \text{a.e. in } Q, \quad (4.21)$$

$$\nabla\theta \cdot \mathbf{n} + \theta = g \quad \text{a.e. on } \partial\Sigma \times (0, T), \quad (4.22)$$

$$\theta(0) = \theta_0, \quad \text{a.e. in } \Sigma, \quad (4.23)$$

and $z \in W^{1,\infty}(0, T; L^\infty(\Sigma))$, $\mathbf{A} \in H^1(0, T; \mathbb{X}) \cap W^{1,\infty}(0, T; \mathbb{L}^2(D))$ solve

$$z_t = \frac{1}{\tau(\bar{\theta})} [z_{\text{eq}}(\bar{\theta}) - z]^+ \quad \text{a.e. in } Q, \quad z(0) = 0 \quad \text{a.e. in } \Sigma, \quad (4.24)$$

$$\int_G \sigma(x, z)\mathbf{A}_t \cdot \mathbf{v} \, dx + \int_D \frac{1}{\mu(x, z)} \operatorname{curl} \mathbf{A} \cdot \operatorname{curl} \mathbf{v} \, dx = \int_\Omega j(t)\mathbf{J}_0(x) \cdot \mathbf{v} \, dx \quad (4.25)$$

for all $\mathbf{v} \in \mathbb{X}$, a.e. in $(0, T)$, $\mathbf{A}(0) = \mathbf{A}_0$, a.e. in D .

\mathcal{T} maps \mathbb{O} in itself. Notice that, given $\bar{\theta} \in \mathbb{O}$, [40, Lemma 2.5] ensures that there exists a unique solution $z \in W^{1,\infty}(0, T_0; L^\infty(\Sigma))$ to (4.24) such that

$$\|z\|_{W^{1,\infty}(0, T_0; L^\infty(\Sigma))} \leq C_1,$$

with C_1 independent of $\bar{\theta}$, and $0 \leq z < 1$ a.e. in Σ .

Then, given $z \in W^{1,\infty}(0, T_0; L^\infty(\Sigma))$, it is possible to find a unique solution $\mathbf{A} \in H^1(0, T_0; \mathbb{X}) \cap W^{1,\infty}(0, T_0; \mathbb{L}^2(D))$ to (4.25) by means of a standard implicit time discretization scheme (cf. e.g. the monograph [45]). The basic estimates are the discrete versions of the ones which follow from taking $\mathbf{v} = \mathbf{A}_t$ in (4.25) (cf. also the following *Second estimate*) and taking the time derivative of (4.25) with $\mathbf{v} = \mathbf{A}_t$ (cf. also the following and *Third estimate*). These give the bound

$$\|\mathbf{A}\|_{H^1(0, T_0; \mathbb{X}) \cap W^{1,\infty}(0, T_0; \mathbb{L}^2(D))} \leq C_2,$$

with C_2 independent of $\bar{\theta}$. Then, using the fact that $\mathbf{A}_t \in L^\infty(0, T_0; \mathbb{L}^2(D))$, $\mathbf{A}_t \in L^2(0, T_0; \mathbb{X}) \hookrightarrow L^2(0, T_0; \mathbb{L}^6(D))$ (due to the continuous embedding of $\mathbb{H}^1(D)$ into $\mathbb{L}^6(D)$) and employing the interpolation inequality (4.10) with $q = 6$, $p = 2$ and $r = 10/3$, we get $\mathbf{A}_t \in \mathbb{L}^{10/3}(D \times (0, T_0))$. This implies that $|\mathbf{A}_t|^2 \in L^{5/3}(D \times (0, T_0))$ on the right hand side of (4.21) and

$$\|\mathbf{A}_t\|_{\mathbb{L}^{10/3}(D \times (0, T_0))} \leq C_3.$$

Applying now the standard maximal regularity results in L^p -spaces (cf. e.g. [64, Thm. 3.1, Prop. 3.3]) to (4.21–4.23), and Hyp. (H) (iv), we can conclude that there exists a unique $\theta \in L^{5/3}(0, T_0; W^{2,5/3}(\Sigma)) \cap W^{1,5/3}(0, T_0; L^{5/3}(\Sigma))$ solving (4.21–4.23) satisfying

$$\|\theta\|_{L^{5/3}(0, T_0; W^{2,5/3}(\Sigma)) \cap W^{1,5/3}(0, T_0; L^{5/3}(\Sigma))} \leq C_4,$$

with C_4 independent of $\bar{\theta}$. Moreover, testing equation (4.21) by θ , we get

$$\|\theta\|_{L^2(0, T_0; H^1(\Sigma)) \cap L^\infty(0, T_0; L^2(\Sigma))} \leq C_5,$$

with C_5 independent of $\bar{\theta}$. This implies in particular

$$\|\theta\|_{L^2(0,t;L^2(\Sigma))} \leq t^{1/2}\|\theta\|_{L^\infty(0,T_0;L^2(\Sigma))} \leq t^{1/2}C_5 \quad \text{for every } t \in [0, T_0].$$

If we choose T_0 such that $T_0^{1/2}C_5 \leq R$, then the map \mathcal{T} maps \mathbb{O} into itself.

\mathcal{T} is compact. The map \mathcal{T} is compact due to the compact embedding

$$\begin{aligned} L^{5/3}(0, T_0; W^{2,5/3}(\Sigma)) \cap L^2(0, T_0; H^1(\Sigma)) \cap W^{1,5/3}(0, T_0; L^{5/3}(\Sigma)) \\ \hookrightarrow L^2(0, T_0; L^2(\Sigma)) \end{aligned} \quad (4.26)$$

(cf. [78, Thm. 4, Cor. 5]).

\mathcal{T} is continuous. The continuity of \mathcal{T} follows from these facts:

1. From [40, Lemma 2.5] we have that, if $\bar{\theta}_k \rightarrow \bar{\theta}$ strongly in $L^2(0, T_0; L^2(\Sigma))$, for $k \rightarrow +\infty$, then $z_k \rightarrow z$ strongly in $W^{1,p}(0, T_0; L^p(\Sigma))$ for every $p \in [1, +\infty)$, where z_k and z are the solutions to (4.24) corresponding to $\bar{\theta}_k$ and $\bar{\theta}$, respectively.
2. From the compact embedding of $H^1(0, T_0; \mathbb{X}) \cap W^{1,\infty}(0, T_0; \mathbb{L}^2(D))$ into $\mathbb{L}^q(D \times (0, T_0))$ (for $q \in [1, 10/3)$), we get that $\partial_t \mathbf{A}_k \rightarrow \partial_t \mathbf{A}$ strongly in $\mathbb{L}^q(D \times (0, T_0))$ for every $q \in [1, 10/3)$, and $\text{curl } \mathbf{A}_k \rightarrow \text{curl } \mathbf{A}$ weakly in $H^1(0, T_0; \mathbb{L}^2(D))$ (at least for a subsequence of k), where \mathbf{A}_k are the solutions to (4.25) corresponding to z_k . There remains to show that the limit \mathbf{A} is the solution of (4.25) corresponding to z . Then, the convergence will hold true for the whole sequence \mathbf{A}_k . Indeed, from the strong convergence of z_k and using Hyp. ((H)) (i), (ii), we get that $\sigma(x, z_k) \rightarrow \sigma(x, z)$ and $\mu(x, z_k) \rightarrow \mu(x, z)$ strongly in $L^p(0, T_0; L^p(\Sigma))$ for every $p \in [1, +\infty)$. This implies that we can pass to the limit for $k \rightarrow +\infty$ and the limit \mathbf{A} solves (4.25).
3. Finally, we can come back to equation (4.21) and we have that $|\partial_t \mathbf{A}_k|^2 \rightarrow |\partial_t \mathbf{A}|^2$ in $L^s(\Sigma \times (0, T_0))$ for some $s \in [1, 5/3)$ because $\partial_t \mathbf{A}_k \rightarrow \partial_t \mathbf{A}$ strongly in $\mathbb{L}^q(D \times (0, T_0))$ for every $q \in [1, 10/3)$ and $\partial_t \mathbf{A}_k, \partial_t \mathbf{A}$ are bounded (uniformly in k) in $\mathbb{L}^2(D \times (0, T_0))$. This fact, together with the strong convergence $\partial_t z_k \rightarrow \partial_t z$ strongly in $L^p(0, T_0; L^p(\Sigma))$ for every $p \in [1, +\infty)$ and $\mathcal{L}(\bar{\theta}_k, z_k) \rightarrow \mathcal{L}(\bar{\theta}, z)$ strongly in $L^2(0, T_0; L^2(\Sigma))$ (cf. Hyp. (H) (iv)), imply that also $\theta_k \rightarrow \theta$ strongly in $L^2(\Sigma \times (0, T_0))$ for $k \rightarrow +\infty$, where θ_k (and θ) are the solutions to (4.21) corresponding to z_k, \mathbf{A}_k (and z, \mathbf{A}), respectively.

Hence, by the Schauder theorem \mathcal{T} admits (at least) one fixed point θ in \mathbb{O} , whence the existence of a solution (\mathbf{A}, θ, z) to (4.11)–(4.18) on the interval $[0, T_0]$ with

$$\begin{aligned} \mathbf{A} &\in H^2(0, T; \mathbb{L}^2(D)) \cap W^{1,\infty}(0, T; \mathbb{X}), \quad \text{curl } \mathbf{A} \in L^\infty(0, T; \mathbb{L}^6(D)), \\ \theta &\in W^{1,5/3}(0, T; L^{5/3}(\Sigma)) \cap L^{5/3}(0, T; W^{2,5/3}(\Sigma)) \cap L^2(0, T; H^1(\Sigma)) \cap L^\infty(Q), \\ z &\in W^{1,\infty}(0, T; L^\infty(\Sigma)), \quad 0 \leq z < 1 \text{ a.e. in } Q. \end{aligned}$$

4.4.2. Global a priori estimates

In order to extend the solution to the whole time interval $[0, T]$ we need to prove suitable global a priori estimates that are independent of T_0 . In what follows the positive constants are denoted by the same symbol C even if they are different from line to line. They may depend on $\sigma, \mu, \tau, z_{\text{eq}}, \mathbf{A}_0, \theta_0, g, j, \mathbf{J}_0$, and T , but not on T_0 .

First estimate. First of all, we can apply [40, Lemma 2.5] to the equation (4.16) entailing the following estimate:

$$\|z\|_{W^{1,\infty}(0,T_0;L^\infty(\Sigma))} \leq C, \quad 0 \leq z(x, t) < 1 \quad \text{a.e. in } Q. \quad (4.27)$$

Second estimate. Take $t \in (0, T_0)$ and $\mathbf{v} = \mathbf{A}_t$ in (4.14). Using Hyp. (H) (i), (ii) (cf. also (4.4)), we get (using the symbol s for the time variable and x for the space variable inside the integrals, but making the dependence on x and s explicit only when it is necessary):

$$\begin{aligned} \frac{\sigma}{2} \int_0^t \int_G |\mathbf{A}_s|^2 dx ds + \int_0^t \int_D \frac{1}{\mu(x, z)} \operatorname{curl} \mathbf{A} \cdot \operatorname{curl} \mathbf{A}_s dx ds \\ \leq \int_0^t \int_\Omega j(s) \mathbf{J}_0(x) \cdot \mathbf{A}_s dx ds. \end{aligned} \quad (4.28)$$

Now, integrating by parts in time the second term in (4.28), we get

$$\begin{aligned} \int_0^t \int_D \frac{1}{\mu(x, z)} \operatorname{curl} \mathbf{A} \cdot \operatorname{curl} \mathbf{A}_s dx ds &= \frac{1}{2} \int_0^t \int_\Sigma \frac{\mu'_{\text{wp}}(z) z_s}{\mu^2(x, z)} |\operatorname{curl} \mathbf{A}|^2 dx ds \\ &\quad + \int_D \frac{1}{2\mu(x, z(t))} |\operatorname{curl} \mathbf{A}|^2(t) dx \\ &\quad - \frac{1}{2} \int_D \frac{1}{\mu(x, 0)} |\operatorname{curl} \mathbf{A}_0|^2 dx. \end{aligned}$$

Then, using estimate (4.27) and Hyp. (H) (ii), we get

$$\begin{aligned} \frac{\sigma}{2} \int_0^t \int_G |\mathbf{A}_s|^2 dx ds + \frac{1}{2\bar{\mu}} \int_D |\operatorname{curl} \mathbf{A}|^2(t) dx &\leq \frac{1}{2\bar{\mu}} \int_D |\operatorname{curl} \mathbf{A}_0|^2 dx \\ &\quad + C \left(\int_0^t \int_D |\operatorname{curl} \mathbf{A}|^2 dx ds + \int_0^t \int_\Omega |j(s)|^2 |\mathbf{J}_0|^2 dx ds \right). \end{aligned}$$

Using now a standard Gronwall lemma together with Hyp (H) (vi), we obtain

$$\int_0^t \int_G |\mathbf{A}_s|^2 dx ds + \int_D |\operatorname{curl} \mathbf{A}|^2(t) dx \leq C \left(1 + \int_0^t \int_\Omega |j(s)|^2 |\mathbf{J}_0(x)|^2 dx ds \right). \quad (4.29)$$

Third estimate. We can now formally (in order to make it rigorous one should perform the estimate e. g. on a time discrete scheme) differentiate (4.14) with respect to t and take $\mathbf{v} = \mathbf{A}_t$ as test function. Integrating over $(0, t)$, using Hyp (H) (i), (ii), as well as the integration by parts in time in the second summand, gives (cf. also (4.2), (4.4)):

$$\begin{aligned} \frac{\sigma}{2} \int_G |\mathbf{A}_t|^2(t) dx + \frac{1}{2\mu} \int_0^t \int_D |\operatorname{curl} \mathbf{A}_s|^2 dx ds &\leq \bar{\sigma} \int_D |\mathbf{A}_t(0)|^2 dx \\ &- \frac{1}{2} \int_0^t \int_\Sigma \sigma'_{\text{wp}}(z) z_s |\mathbf{A}_s|^2 dx ds + \int_0^t \int_\Sigma \frac{\mu'_{\text{wp}}(z) z_s}{\mu^2(x, z)} \operatorname{curl} \mathbf{A} \cdot \operatorname{curl} \mathbf{A}_s dx ds \\ &+ \int_0^t \int_\Omega |j'(s)|^2 |\mathbf{J}_0(x)|^2 dx ds. \end{aligned}$$

Using now estimates (4.27), (4.29), and Hyp. (H) (i), (ii), (vi), we obtain

$$\begin{aligned} \int_G |\mathbf{A}_t|^2(t) dx + \int_0^t \int_D |\operatorname{curl} \mathbf{A}_s|^2 dx ds \\ \leq C \left(1 + \int_0^t \int_\Omega (|j'(s)|^2 + |j(s)|^2 + |j(0)|^2) |\mathbf{J}_0(x)|^2 dx ds \right), \quad (4.30) \end{aligned}$$

where the inequality $\|\mathbf{A}_t(0)\|_{\mathbb{L}^2(D)}^2 \leq C(\|\mathbf{A}_0\|_{\mathbb{H}^2(D)}^2 + \int_\Omega |j(0)|^2 |\mathbf{J}_0(x)|^2 dx)$ has been used.

Fourth estimate. Collecting (4.29) and (4.30) and using the continuous embedding of $\mathbb{H}^1(D)$ into $\mathbb{L}^6(D)$ and employing the interpolation inequality (4.10) with $q = 6$, $p = 2$ and $r = 10/3$, and Hyp. (H) (iii), we get

$$\|\mathbf{A}\|_{H^1(0, T_0; \mathbb{X}) \cap W^{1, \infty}(0, T_0; \mathbb{L}^2(D))} + \|\mathbf{A}_t\|_{\mathbb{L}^{10/3}(D \times (0, T_0))} \leq C. \quad (4.31)$$

This implies that $|\mathbf{A}_t|^2 \in L^{5/3}(Q)$ on the right hand side of (4.15). Applying now the standard maximal regularity results in L^q -spaces (cf. e. g. [64, Thm. 3.1, Prop. 3.3]) to (4.15), (4.17–4.18), together with Hyp. (H) (iv), (v), (vi) we can deduce the estimate

$$\|\theta\|_{L^{5/3}(0, T_0; W^{2, 5/3}(\Sigma)) \cap W^{1, 5/3}(0, T_0; L^{5/3}(\Sigma))} \leq C. \quad (4.32)$$

Moreover, we can test (4.15) by θ obtaining, in particular, the estimate

$$\|\theta\|_{L^2(0, T_0; H^1(\Sigma)) \cap L^\infty(0, T_0; L^2(\Sigma))} \leq C. \quad (4.33)$$

From the non-negativity of the r.h.s in (4.15) and of the initial and boundary conditions we also get $\theta \geq 0$ a.e. More generally, from (4.31), using the interpolation inequality (4.10), we also get

$$\|\mathbf{A}_t\|_{L^{\frac{4p}{3(p-2)}}(0, T_0; L^p(\Sigma))} \leq C$$

for all $p \in (0, 6]$. Hence, due to (4.27) and Hyp. (H) (iv), the right hand side of (4.15) is in $L^{\frac{2p}{3(p-2)}}(0, T_0; L^{\frac{p}{2}}(\Sigma))$ and so we can apply the standard maximal regularity results in L^q -spaces for parabolic equations to (4.15) (cf. e. g. [64, Thm. 3.1, Prop. 3.3]), obtaining

$$\|\theta\|_{L^{\frac{2p}{3(p-2)}}(0, T_0; W^{2, \frac{p}{2}}(\Sigma)) \cap W^{1, \frac{2p}{3(p-2)}}(0, T_0; L^{\frac{p}{2}}(\Sigma))} \leq C, \quad (4.34)$$

for all $p \in (2, 6]$.

Fifth estimate. By comparison in the ODE (4.16), by taking then the time derivative of eqrefeqzw, and using (4.34) and Hyp. (H) (iv), we get, for all $p \in (2, 6]$

$$\|z_t\|_{L^2(0, T_0; W^{2, p/2}(\Sigma))} + \|z_{tt}\|_{L^{\frac{2p}{3(p-2)}}(0, T_0; L^{p/2}(\Sigma))} \leq C, \quad (4.35)$$

implying

$$\|\nabla z\|_{L^\infty(0, T_0; W^{1, p/2}(\Sigma))} \leq C,$$

and so, using the Sobolev embedding of $W^{1,3}(\Sigma)$ into $L^\infty(\Sigma)$, we get

$$\|\nabla z\|_{L^\infty(\Sigma \times (0, T_0))} \leq C. \quad (4.36)$$

Sixth estimate. Using the $L^\infty(0, T_0; \mathbb{L}^2(D))$ -regularity of \mathbf{A}_t (compare (4.31)) and Hyp. (H) (iii) on j and \mathbf{J}_0 , by comparison in (4.14), we get

$$\left\| \operatorname{curl} \left(\frac{1}{\mu(x, z)} \operatorname{curl} \mathbf{A} \right) \right\|_{L^\infty(0, T_0; \mathbb{L}^2(D))} \leq C.$$

Moreover, we can formally compute the divergence operator of $\frac{1}{\mu(x, z)} \operatorname{curl} \mathbf{A}$ and we get by applying Hyp. (H) (ii)

$$\operatorname{div} \left(\frac{1}{\mu(x, z)} \operatorname{curl} \mathbf{A} \right) = \frac{\mu'_{\text{wp}}(z) \nabla z}{\mu^2(x, z)} \operatorname{curl} \mathbf{A} \in L^\infty(0, T_0; \mathbb{L}^2(\Sigma)),$$

because $\operatorname{curl} \mathbf{A} \in L^\infty(0, T_0; \mathbb{L}^2(D))$ and $\nabla z \in L^\infty(0, T; L^\infty(\Sigma))$ due to (4.36). Thus, applying Lemma 4.1 with $p = 2$, $U = D$, $\xi = 6$, we obtain

$$\|\operatorname{curl} \mathbf{A}\|_{L^\infty(0, T_0; \mathbb{L}^6(D))} \leq C. \quad (4.37)$$

Notice that we can apply Lemma 4.1 with every exponent α (hence $\xi = p^* = 6$) because, due to formula (4.9) and to the fact that $\mathbf{A} \in L^\infty(0, T; \mathbb{X})$, we have that $\gamma_n(\operatorname{curl} \mathbf{A}) = 0$.

Seventh estimate. We can now formally (in order to make it rigorous one should perform the estimate e.g. on a time discrete scheme) differentiate (4.14) with respect to t and take $\mathbf{v} = \mathbf{A}_{tt}$ as test function. Integrating over $(0, t)$ and using Hyp (H) (i), (ii) (cf. (4.2), (4.4)) we get

$$\begin{aligned}
\sigma \int_0^t \int_D |\mathbf{A}_{ss}|^2 dx ds + \frac{1}{2\bar{\mu}} \int_D |\operatorname{curl} \mathbf{A}_t|^2(t) dx &\leq \frac{1}{2\bar{\mu}} \int_D |\operatorname{curl} \mathbf{A}_t(0)|^2 dx \\
&- \int_0^t \int_{\Sigma} \frac{\mu'_{\text{wp}}(z)}{\mu^2(x, z)} z_s |\operatorname{curl} \mathbf{A}_s|^2 dx ds \\
&- \int_0^t \int_{\Sigma} \sigma'_{\text{wp}}(z) z_s \mathbf{A}_s \mathbf{A}_{ss} dx ds \\
&- \int_0^t \int_{\Sigma} \frac{\mu'_{\text{wp}}(z)}{\mu^2(x, z)} z_s \operatorname{curl} \mathbf{A}_{ss} \operatorname{curl} \mathbf{A} dx ds \\
&+ \int_0^t \int_{\Omega} \mathbf{J}_0(x) j'(s) dx ds.
\end{aligned}$$

We start estimating the second integral in the r.h.s using Hyp (H) (ii) and estimates (4.27), (4.31) as follows:

$$- \int_0^t \int_{\Sigma} \frac{\mu'_{\text{wp}}(z)}{\mu^2(x, z)} z_s |\operatorname{curl} \mathbf{A}_s|^2 dx ds \leq C \|\operatorname{curl} \mathbf{A}_t\|_{L^2(0, T_0; \mathbb{L}^2(D))} \leq C.$$

In order to bound the third integral we use Hyp. (H) (i) and again estimates (4.27), (4.31) as follows:

$$\begin{aligned}
- \int_0^t \int_{\Sigma} \sigma'_{\text{wp}}(z) z_s \mathbf{A}_s \mathbf{A}_{ss} dx ds &\leq C \|\mathbf{A}_t\|_{L^2(0, T_0; \mathbb{L}^2(D))}^2 + \frac{1}{2\bar{\sigma}} \int_0^t \int_D |\mathbf{A}_{ss}|^2 dx ds \\
&\leq C + \frac{\sigma}{2} \int_0^t \int_D |\mathbf{A}_{ss}|^2 dx ds.
\end{aligned}$$

In the fourth integral we need to use the integration by parts formula, Hyp. (H) (ii), and estimates (4.27), (4.31), and (4.37):

$$\begin{aligned}
& \int_0^t \int_{\Sigma} \frac{\mu'_{\text{wp}}(z)}{\mu^2(x, z)} z_s \operatorname{curl} \mathbf{A}_{ss} \operatorname{curl} \mathbf{A} \, dx \, ds \\
& \leq C \int_0^t \|\operatorname{curl} \mathbf{A}_s\|_{\mathbb{L}^2(D)} \|\operatorname{curl} \mathbf{A}\|_{\mathbb{L}^6(D)} \|z_{ss}\|_{L^3(\Sigma)} \, ds + C \int_0^t \|\operatorname{curl} \mathbf{A}_s\|_{\mathbb{L}^2(D)}^2 \, ds \\
& \leq C \int_0^t \|\operatorname{curl} \mathbf{A}_s\|_{\mathbb{L}^2(D)} \|z_{ss}\|_{L^3(\Sigma)} \, ds + C \int_0^t \|\operatorname{curl} \mathbf{A}_s\|_{\mathbb{L}^2(D)}^2 \, ds.
\end{aligned}$$

Now, we use Hyp. (H) (iii), (vi), estimate (4.35) with $p = 3$, and apply a standard Gronwall lemma to the following inequality

$$\frac{\sigma}{2} \int_0^t \int_D |\mathbf{A}_{ss}|^2 \, dx \, ds + \frac{1}{2\bar{\mu}} \int_D |\operatorname{curl} \mathbf{A}_t|^2(t) \, dx \leq C + C \int_0^t \|\operatorname{curl} \mathbf{A}_s\|_{\mathbb{L}^2(D)} \|z_{ss}\|_{L^3(\Sigma)} \, ds,$$

getting the desired estimate

$$\|\mathbf{A}_{tt}\|_{L^2(0, T_0; \mathbb{L}^2(D))} + \|\operatorname{curl} \mathbf{A}_t\|_{L^\infty(0, T_0; \mathbb{L}^2(D))} \leq C. \quad (4.38)$$

and so, since $|\mathbf{A}_t|^2 \in L^\infty(0, T_0; \mathbb{L}^3(D))$, using [46], we get

$$\|\theta\|_{L^\infty(\Sigma \times (0, T_0))} \leq C. \quad (4.39)$$

Collecting estimates (4.27), (4.31), (4.32), (4.36)–(4.39), we can now extend the solution we found on $[0, T_0]$ to the whole time interval $[0, T]$. Finally, notice that testing (4.15) by $-\theta^-$, where $[\cdot]^-$ denotes the negative part, and using the assumptions on \mathcal{L} , Hyp. (H) (vi) together with Hyp. (H) (v), (vi), we gain the non-negativity of θ . This concludes the proof of existence of solutions to Problem (P).

4.4.3. Stability estimate

In this section we prove the stability estimate (4.20), entailing, in particular, uniqueness of solutions to Problem (P). Consider the time derivative of equation (4.14) and rewrite it in the following form

$$\begin{aligned}
& \int_G (h(x, z, z_t) \mathbf{A}_t + \sigma(x, z) \mathbf{A}_{tt}) \cdot \mathbf{v} \, dx \\
& + \int_D \left(\frac{1}{\mu(x, z)} \operatorname{curl} \mathbf{A}_t + \ell(x, z, z_t) \operatorname{curl} \mathbf{A} \right) \cdot \operatorname{curl} \mathbf{v} \, dx = \int_\Omega \mathbf{j}'(t) J_0(x) \cdot \mathbf{v} \, dx,
\end{aligned} \quad (4.40)$$

for all $\mathbf{v} \in \mathbb{X}$ and a.e. in $(0, T)$, where

$$h(x, z, z_t) := \sigma'(x, z)z_t, \quad \ell(x, z, z_t) := \frac{\mu_z(x, z)z_t}{\mu^2(x, z)}.$$

Let $(\mathbf{A}_i, \theta_i, z_i)$, $i = 1, 2$, denote two triples of solutions corresponding to the data $(\mathbf{A}_{0,i}, \theta_{0,i}, j_i)$. Take the difference of (4.40) for the two triples $i = 1, 2$ and take the test function $\mathbf{v} = \bar{\mathbf{A}}_t := (\mathbf{A}_1 - \mathbf{A}_2)_t$. Then, denoting by $\bar{z} := z_1 - z_2$, we get, integrating over $(0, t)$

$$\begin{aligned} & \frac{\sigma}{2} \int_G |\bar{\mathbf{A}}_t(t)|^2 dx + \frac{1}{\bar{\mu}} \int_0^t \int_D |\operatorname{curl} \bar{\mathbf{A}}_s|^2 dx ds \\ & \leq \frac{\sigma}{2} \int_G |\bar{\mathbf{A}}_t(0)|^2 dx + C_\sigma \int_0^t (\|\bar{z}\|_{L^\infty(\Sigma)} + \|\bar{z}_s\|_{L^\infty(\Sigma)}) \|\bar{\mathbf{A}}_s\|_{\mathbb{L}^2(D)}^2 ds \\ & \quad + C_\sigma \int_0^t \left(\|\bar{\mathbf{A}}_s\|_{\mathbb{L}^2(D)}^2 + \|\bar{z}\|_{L^\infty(\Sigma)} \|\mathbf{A}_{1,ss}\|_{\mathbb{L}^2(D)} \|\bar{\mathbf{A}}_s\|_{L^2(D)} \right) ds \\ & \quad + C_\mu \int_0^t (\|\bar{z}\|_{L^\infty(\Sigma)} + \|\bar{z}_s\|_{L^\infty(\Sigma)}) \|\bar{\mathbf{A}}_s\|_{\mathbb{L}^2(D)}^2 ds \\ & \quad + C_\mu \int_0^t (\|\operatorname{curl} \bar{\mathbf{A}}\|_{\mathbb{L}^2(D)} \|\bar{\mathbf{A}}_s\|_{\mathbb{L}^2(D)} + \|\bar{z}\|_{L^\infty(\Sigma)} \|\operatorname{curl} \bar{\mathbf{A}}_s\|_{\mathbb{L}^2(D)}) ds \\ & \quad + C \int_0^t |j'_1 - j'_2| \|\bar{\mathbf{A}}_s\|_{\mathbb{L}^2(D)} ds, \end{aligned} \tag{4.41}$$

where we have used the following inequalities (holding true for a.e. x) due to Hyp. (H) (i), (ii):

$$\begin{aligned} |h(x, z_1, z_{1,t}) - h(x, z_2, z_{2,t})| & \leq C_\sigma (|z_{1,t}| |z_1 - z_2| + |z_{1,t} - z_{2,t}|), \\ |h(x, z_2, z_{2,t})| & \leq C_\sigma |z_{2,t}|, \\ |\ell(x, z_1, z_{1,t}) - \ell(x, z_2, z_{2,t})| & \leq C_\mu (|z_1 - z_2| |z_{1,t}| + |(z_1 - z_2)_t|), \\ |\ell(x, z_2, z_{2,t})| & \leq C_\mu |z_{2,t}|. \end{aligned}$$

Test now the difference of (4.15) for $i = 1, 2$ by $\bar{\theta} := \theta_1 - \theta_2$, integrate over $(0, t)$, and use the following inequalities

$$\begin{aligned} \|\bar{z}\|_{L^\infty(\Sigma)} + \int_0^t \|\bar{z}_s\|_{L^\infty(\Sigma)} \, ds &\leq C \int_0^t \|\bar{\theta}\|_{L^\infty(\Sigma)} \, ds \leq C \int_0^t \|\bar{\theta}\|_{W^{2,3/2}(\Sigma)} \, ds \quad (4.42) \\ &\leq C \int_0^t (\|\mathbf{A}_{1,s}\|^2 - \|\mathbf{A}_{2,s}\|^2\|_{\mathbb{L}^{3/2}(D)} + \|\bar{z}_s\|_{L^2(\Sigma)}) \, ds \\ &\leq C \int_0^t (\|\mathbf{A}_{1,s}\|_{\mathbb{L}^6(D)} + \|\mathbf{A}_{2,s}\|_{\mathbb{L}^6(D)}) \|\bar{\mathbf{A}}_s\|_{\mathbb{L}^2(D)} + \|\bar{\theta}\|_{L^2(\Sigma)} \, ds, \end{aligned}$$

obtaining (for all positive δ)

$$\begin{aligned} \|\bar{\theta}(t)\|_{L^2(\Sigma)}^2 + \int_0^t \|\nabla \bar{\theta}\|_{L^2(\Sigma)}^2 \, ds &\leq C \|\bar{\theta}(0)\|_{L^2(\Sigma)}^2 \\ + \delta \int_0^t \|\bar{\theta}\|_{L^6(\Sigma)}^2 \, ds + C_\delta \int_0^t &\left(\|\bar{\theta}\|_{L^2(\Sigma)}^2 + (\|\mathbf{A}_{1,s}\|_{\mathbb{L}^6(D)} + \|\mathbf{A}_{2,s}\|_{\mathbb{L}^6(D)}) \|\bar{\mathbf{A}}_s\|_{\mathbb{L}^2(D)} \right) \, ds. \end{aligned} \quad (4.43)$$

Add now the term $\int_0^t \|\bar{\theta}\|_{L^2(\Sigma)}^2$ to both sides of (4.43), choose δ sufficiently small and add the result up to (4.41), one obtains (for all positive constant η)

$$\begin{aligned} \|\bar{\mathbf{A}}_t(t)\|_{\mathbb{L}^2(D)}^2 + \int_0^t \|\operatorname{curl} \bar{\mathbf{A}}_s\|_{\mathbb{L}^2(D)}^2 \, ds + \|\bar{\theta}(t)\|_{L^2(\Sigma)}^2 + \int_0^t \|\bar{\theta}\|_{H^1(\Sigma)}^2 \, ds &\quad (4.44) \\ \leq C \|\bar{\mathbf{A}}_t(0)\|_{\mathbb{L}^2(D)}^2 + C \|\operatorname{curl} \bar{\mathbf{A}}(0)\|_{\mathbb{L}^2(D)}^2 + C \|\bar{\theta}(0)\|_{L^2(\Sigma)}^2 + C \int_0^t |j_1(s) - j_2(s)|^2 \, ds \\ + \eta \int_0^t \|\operatorname{curl} \bar{\mathbf{A}}_s\|_{\mathbb{L}^2(D)}^2 \, ds + C_\eta \int_0^t \|\bar{\theta}\|_{L^2(\Sigma)}^2 \, ds \\ + C_\eta \int_0^t \left(\|\mathbf{A}_{1,s}\|_{\mathbb{L}^6(D)}^2 + \|\mathbf{A}_{2,s}\|_{\mathbb{L}^6(D)}^2 + \|\mathbf{A}_{1,ss}\|_{\mathbb{L}^2(D)}^2 \right) \|\bar{\mathbf{A}}_s\|_{\mathbb{L}^2(D)}^2 \, ds, \end{aligned}$$

where once more (4.42) has been used. Choosing now η sufficiently small in (4.44) and applying a standard Gronwall lemma together with the regularity properties (4.11) of the solution, we obtain the desired stability estimate (4.20). This concludes the proof of Theorem 1.

Chapter 5.

Numerical solution of the induction hardening problem

Introduction

In Chapter 4 the existence and uniqueness of solutions for a simplified induction hardening problem was established, where the material parameters depend only on the phase fraction z . In this chapter, the numerical solution of the full nonlinear problem is considered. Summarizing again, the induction hardening problem consists of finding functions $\mathbf{A}(x, t)$, $\theta(x, t)$ and $z(x, t)$ that satisfy the following system of partial and ordinary differential equations

$$\begin{aligned} \sigma \frac{\partial \mathbf{A}}{\partial t} + \operatorname{curl} \frac{1}{\mu} \operatorname{curl} \mathbf{A} &= \mathbf{J}_{\text{src}} && \text{in } D \\ \rho c_p \frac{\partial \theta}{\partial t} - \operatorname{div} \kappa \nabla \theta &= \sigma \left| \frac{\partial \mathbf{A}}{\partial t} \right|^2 - \rho \mathcal{L} \frac{\partial z}{\partial t} && \text{in } \Sigma \\ \frac{\partial z}{\partial t} &= \frac{z^{\tau(\theta)}}{\tau(\theta)} [z_{\text{eq}}(\theta) - z]^+ && \text{in } \Sigma \end{aligned} \quad (5.1)$$

for $t \in (0, T)$, where \mathbf{J}_{src} and \mathcal{L} denote the source current and the latent heat as introduced in (3.17) and (3.34). As initial and boundary conditions we impose

$$\begin{aligned} \mathbf{A} \times \mathbf{n} &= 0 \quad \text{on } \partial D, & \kappa \nabla \theta \cdot \mathbf{n} + \eta \theta &= g \quad \text{on } \partial \Sigma, \\ \mathbf{A}(x, 0) &= \mathbf{A}_0(x) \quad \text{in } D, & \theta(x, 0) = \theta_0(x) \quad \text{and } z(0) &= 0 \quad \text{in } \Sigma. \end{aligned} \quad (5.2)$$

The numerical solution process poses different challenges. The problem comprises of nonlinear, coupled equations in the time domain that exhibit different time scales. Furthermore, due to the skin effect, the eddy current density concentrates in a small boundary layer of the workpiece, which has to be resolved by the spatial discretization. Consequently, the problem also exhibits different length scales that will be resolved by adaptively generated grids using residual based error estimators.

The electromagnetic fields satisfy certain continuity conditions, they possess only tangential continuity. This must be reproduced by the numerical scheme. For the discretization of the curl-curl equation, the finite element method using edge elements is utilized.

The induction heating model represent an evolutionary problem. The common approach is to discretize the equations with respect to space and with respect to time separately. At first, the equations are discretized in space by a Galerkin method. This is presented in Section 5.1 and 5.2. As a result one obtains a system of ordinary differential equations, which is continuous in time. The discretization with respect to time is considered in Section 5.3.

5.1. Discretization in space by the Galerkin method

The basic concept of the Galerkin method can be summarized as follows. Independent of the specific problem to solve, it consist of the following steps:

- (i) The equations are considered as a variational problem.
- (ii) One searches for the solution on a finite dimensional domain V_h that is equipped with a basis $\{\varphi_1, \dots, \varphi_N\}$. The fields of interest, e. g. the temperature $\theta(x, t)$, are expressed by a linear combination of the basis functions by the ansatz

$$\theta(x, t) = \sum_{i=1}^N \theta_i(t) \varphi_i(x).$$

- (iii) For the Galerkin method, the test functions for the variational formulation are chosen as the basis functions. There results a system of equations that has to be solved by suitable methods to determine the unknown coefficients θ_i .

The finite element method represents a special case of the Galerkin method, where the computational domain is decomposed into small subdomains K_j , e. g. triangles in 2D or tetrahedrons in 3D. The basis functions are defined locally on the triangulation $\mathcal{T}_h = \{K_j\}_{j \in \mathcal{I}}$ and have to satisfy certain conditions. The finite element method as a special Galerkin method will be explained in more detail in Section 5.2.

5.1.1. Introduction of the Galerkin method

The Galerkin method describes a procedure to solve the variational formulation corresponding to equation (5.1). It is assumed that for fixed time $t \in (0, T)$, the variational formulation of the continuous problem (5.1) possesses a solution $\mathbf{A}(t)$ in some space \mathbb{W} , $\theta(t)$ in V and $z(t)$ in Z . Then it is the fundamental approach to find approximate solutions $\mathbf{A}_h(t)$ in \mathbb{W}_h , $\theta_h(t)$ in V_h and $z_h(t)$ in Z_h with finite dimensional spaces consisting of vector valued functions \mathbb{W}_h to discretize the magnetic vector potential and scalar valued functions V_h and Z_h to discretize the temperature and the volume fraction of austenite with respect to space. For simplicity we will approximate θ_h and z_h with the same set of functions, i. e. $V_h = Z_h$.

Since the spaces V_h and \mathbb{W}_h are finite dimensional, there exist basis functions such that

$$V_h = Z_h = \text{span}\{\varphi_1, \dots, \varphi_N\} \quad \text{and} \quad \mathbb{W}_h = \text{span}\{\psi_1, \dots, \psi_N\}. \quad (5.3)$$

The unknown discrete solutions for the fields of interest are then expressed by the basis in terms of the following ansatz

$$\theta_h(x, t) = \sum_{i=1}^N \theta_i(t) \varphi_i(x), \quad z_h(x, t) = \sum_{i=1}^N z_i(t) \varphi_i(x) \quad \text{and} \quad \mathbf{A}_h = \sum_{i=1}^{\tilde{N}} A_i(t) \boldsymbol{\psi}_i(x) \quad (5.4)$$

with time dependent coefficients $\theta_i(t), z_i(t), i = 1, \dots, N$ and $A_i(t), i = 1, \dots, \tilde{N}$.

In order to determine a discrete solution, the weak formulation corresponding to equation (5.1) is considered on the spaces V_h and \mathbb{W}_h . In addition to the ansatz functions, the test functions for the weak formulation are also taken from the spaces V_h and \mathbb{W}_h , respectively.

In Chapter 4, the weak formulation of the vector potential equation was introduced, which is now adapted to the discrete setting. For a fixed time $t \in (0, T)$ we regard the function $x \mapsto \mathbf{A}_h(x, t)$ as an element of \mathbb{W}_h and write $\mathbf{A}_h(t) \in \mathbb{W}_h$. For variable t , we obtain a function $t \mapsto \mathbf{A}_h(t)$ with values in \mathbb{W}_h . The weak formulation of (5.1)₁ is now: Find $\mathbf{A}_h(t) \in \mathbb{W}_h$ such that the following equation holds, cf. equation (4.14)

$$\int_D \sigma \partial_t \mathbf{A}_h \cdot \boldsymbol{\psi}_h \, dx + \int_D \mu^{-1} \operatorname{curl} \mathbf{A}_h \cdot \operatorname{curl} \boldsymbol{\psi}_h \, dx = \int_D \mathbf{J}_{\text{src}} \cdot \boldsymbol{\psi}_h \, dx \quad (5.5)$$

for all $\boldsymbol{\psi}_h \in \mathbb{W}_h$ and a.e. in $(0, T)$ with initial condition $\mathbf{A}_h(x, 0) = \mathbf{A}_{h,0}(x)$ and $\operatorname{div} \mathbf{A}_{h,0} = 0$.

While in Chapter 4 the gauging condition $\operatorname{div} \mathbf{A} = 0$ was included in the ansatz space \mathbb{X} , we drop this condition for the numerical solution. Instead, we introduce a regularization of the electric conductivity σ in non-conducting regions such that

$$\sigma = \sigma_{\text{NC}} \quad \text{in} \quad D \setminus (\Sigma \cup \Omega) \quad \text{with} \quad 0 < \sigma_{\text{NC}} \ll \min\{\sigma_{\text{wp}}, \sigma_{\text{Cu}}\}. \quad (5.6)$$

It is assumed that the compatibility condition $\operatorname{div} \mathbf{J}_{\text{src}} = 0$ holds and the initial data satisfies $\operatorname{div} \mathbf{A}_{h,0} = 0$, cf. (3.4). Then, the condition $\operatorname{div} \mathbf{A}_h = 0$ is automatically satisfied (in a weak sense). The essential boundary condition $\mathbf{A}_h \times \mathbf{n} = 0$ on ∂D must be included in the definition of the space \mathbb{W}_h .

By analogous considerations as for the vector potential, we obtain the weak form of the heat equation: Find $\theta_h(t) \in V_h$ such that

$$\int_{\Sigma} \rho c_p \partial_t \theta_h \varphi_h \, dx + \int_{\Sigma} \kappa \nabla \theta_h \cdot \nabla \varphi_h \, dx + \int_{\partial \Sigma} \eta \theta_h \varphi_h \, da = \int_{\Sigma} \hat{f}_h \varphi_h \, dx + \int_{\partial \Sigma} g \varphi_h \, da \quad (5.7)$$

for all $\varphi_h \in V_h$ and a.e. in $(0, T)$ with $\theta_h(x, 0) = \theta_{h,0}(x)$. The expression $\hat{f}_h = \sigma \left| \frac{\partial \mathbf{A}_h}{\partial t} \right|^2 - \rho \mathcal{L} \frac{\partial z_h}{\partial t}$ is used as abbreviation for the right hand side.

For the discretization of the rate law for the phase fraction of austenite, several strategies might be possible, either a projection of the rate law on the space V_h or the introduction of a suitable interpolation operator. The projection of equation (5.1)₃ onto the space V_h corresponds to a variational formulation.

Later on, the finite element method is introduced and the discrete space V_h will be chosen as the standard P_1 -finite element space, where the degrees of freedom correspond to nodal values. In this case, an interpolation can be easily realized by evaluating the rate law at the nodes of the discretization. In Section 5.2.5 the discretization of the rate law is described in detail using the finite element interpolation operator.

In order to complete the weak formulation, the initial and boundary conditions (5.2) have to be included in a suitable way. Regarding the boundary conditions, natural boundary conditions enter directly in the weak formulation, as it is the case for equation (5.7). Essential boundary conditions like $\mathbf{A}_h \times \mathbf{n} = 0$ on ∂D are included in the definition of the finite dimensional spaces \mathbb{W}_h and V_h . The definition of these spaces is considered later on.

The initial conditions that are defined for \mathbf{A}_h, θ_h and z_h on the spaces \mathbb{W}_h and V_h must be consistent with (5.2). This can be achieved by using projection operators on the spaces V_h and \mathbb{W}_h that account for the condition $\operatorname{div} \mathbf{A}_{h,0} = 0$, i. e.

$$\mathbf{A}_h(x, 0) = \Pi_{\mathbb{W}}(\mathbf{A}_0(x)), \quad \theta_h(x, 0) = \Pi_V(\theta_0(x)) \quad \text{and} \quad z_h(x, 0) = 0, \quad (5.8)$$

with suitable projection operators Π_V on V_h and $\Pi_{\mathbb{W}}$ on \mathbb{W}_h , satisfying $\operatorname{div}(\Pi_{\mathbb{W}} \mathbf{A}) = 0$ for all \mathbf{A} with $\operatorname{div} \mathbf{A} = 0$ at least in a weak sense.

The weak formulation introduced above has to hold for all $\varphi_h \in V_h$ and $\psi_h \in \mathbb{W}_h$. Since the spaces V_h and \mathbb{W}_h are finite dimensional, the basis functions are used as test functions. Summarizing, the weak formulation of the induction hardening problem is the following. We search for the functions $\mathbf{A}_h(t) \in \mathbb{W}_h$, $\theta_h(t) \in V_h$ and $z_h(t) \in V_h$ as defined by the ansatz (5.4) such that for $t \in (0, T)$ the following equations are satisfied for all $j = 1, \dots, \tilde{N}$ and $k = 1, \dots, N$:

$$\begin{aligned} \int_D \sigma \partial_t \mathbf{A}_h \cdot \psi_j \, dx + \int_D \mu^{-1} \operatorname{curl} \mathbf{A}_h \cdot \operatorname{curl} \psi_j \, dx &= \int_D \mathbf{J}_{\text{src}} \cdot \psi_j \, dx \\ \int_{\Sigma} \rho c_p \partial_t \theta_h \varphi_k \, dx + \int_{\Sigma} \kappa \nabla \theta_h \cdot \nabla \varphi_k \, dx + \int_{\partial \Sigma} \eta \theta_h \varphi_j \, da &= \int_{\Sigma} \hat{f} \varphi_k \, dx + \int_{\partial \Sigma} g \varphi_k \, da \\ \partial_t z_h &= \mathcal{I}_{\mathcal{T}} \left(\frac{z_h^{r(\theta_h)}}{\tau(\theta_h)} [z_{\text{eq}}(\theta_h) - z_h]^+ \right) \\ \mathbf{A}_h(x, 0) = \Pi_{\mathbb{W}}(\mathbf{A}_0(x)), \quad \theta_h(x, 0) = \Pi_V(\theta_0(x)) \quad \text{and} \quad z_h(x, 0) &= 0. \end{aligned} \quad (5.9)$$

The discretization of the rate law for the phase fraction z_h using the interpolation operator $\mathcal{I}_{\mathcal{T}}$ is described in detail in Section 5.2.5.

5.1.2. The semi-discretized problem

Introducing the ansatz functions (5.4) into the weak formulation given above, there results a nonlinear system of ordinary differential equations, which has to be solved by suitable methods. The discretization with respect to time and the linearization of the resulting system is considered in Section 5.3.

In the case of the heat equation one obtains a system of nonlinear ordinary differential equations for the time dependent coefficients $\theta_i(t)$, $i = 1, \dots, N$, which can be written as

$$\mathbf{D}_{\rho c} \partial_t \underline{\theta} + \mathbf{S}_{\kappa} \underline{\theta} = \hat{F}. \quad (5.10)$$

Underlined quantities denote the vector representing the ansatz function (5.4), i. e. $\underline{\theta} = \{\theta_i(t)\}_{i=1, \dots, N}$ with $\theta_h(x, t) = \sum_{i=1}^N \theta_i(t) \varphi_i(x)$. We introduced the matrices

$$\begin{aligned} \mathbf{D}_{\rho c} &= D_{\rho c, ij} & \text{with} & \quad D_{\rho c, ij} = \int_{\Sigma} \rho c_p \varphi_i \varphi_j \, dx \\ \mathbf{S}_{\kappa} &= S_{\kappa, ij} & \text{with} & \quad S_{\kappa, ij} = \int_{\Sigma} \kappa \nabla \varphi_i \cdot \nabla \varphi_j \, dx + \int_{\partial \Sigma} \eta \varphi_i \varphi_j \, da. \end{aligned} \quad (5.11)$$

The matrix $\mathbf{D}_{\rho c}$ denotes the mass matrix and \mathbf{S}_{κ} the stiffness matrix. The right hand side is abbreviated by a (nonlinear) vector $\hat{F}(\underline{A}, \underline{\theta}, \underline{z}) = \{\hat{F}_j(\underline{A}, \underline{\theta}, \underline{z})\}_{j=1, \dots, N}$ with

$$\hat{F}_j(\underline{A}, \underline{\theta}, \underline{z}) = \int_{\Sigma} \hat{f}(\mathbf{A}_h, \theta_h, z_h) \varphi_j \, dx + \int_{\partial \Sigma} g \varphi_j \, da. \quad (5.12)$$

For the vector potential \mathbf{A}_h there results the following system of nonlinear ordinary differential equations for the time dependent coefficients $A_i(t)$, $i = 1, \dots, \tilde{N}$

$$\mathbf{M}_{\sigma} \partial_t \underline{A} + \mathbf{K}_{\mu} \underline{A} = \hat{J} \quad (5.13)$$

with $\underline{A} = \{A_i(t)\}_{i=1, \dots, \tilde{N}}$. The newly introduced matrices \mathbf{M}_{σ} and \mathbf{K}_{μ} refer to the mass matrix (associated to \mathbb{W}_h) and the curl-curl matrix. They are defined as

$$\begin{aligned} \mathbf{M}_{\sigma} &= M_{\sigma, ij} & \text{with} & \quad M_{\sigma, ij} = \int_D \sigma \psi_i \cdot \psi_j \, dx \\ \mathbf{K}_{\mu} &= K_{\mu, ij} & \text{with} & \quad K_{\mu, ij} = \int_D \mu^{-1} \operatorname{curl} \psi_i \cdot \operatorname{curl} \psi_j \, dx. \end{aligned} \quad (5.14)$$

The right hand side is a time dependent vector $\hat{J}(t) = \{\hat{J}_j(t)\}_{j=1, \dots, \tilde{N}}$ and is defined as

$$\hat{J}_j(t) = \int_D \mathbf{J}_{\text{src}}(t) \cdot \psi_j \, dx. \quad (5.15)$$

Summary of the semi-discretized system

Summarizing the equations discretized in space we have to solve the following (nonlinear) system of ordinary differential equations to determine $\mathbf{A}_h(t) \in \mathbb{W}_h$, $\theta_h(t) \in V_h$

and $z_h(t) \in V_h$ defined by (5.4) such that for $t \in (0, T)$ there holds

$$\begin{aligned} \mathbf{M}_\sigma \partial_t \underline{A} + \mathbf{K}_\mu \underline{A} &= \hat{J} \\ \mathbf{D}_{\rho c} \partial_t \underline{\theta} + \mathbf{S}_\kappa \underline{\theta} &= \hat{F} \\ \partial_t z_h &= \mathcal{I}_T \left(\frac{z_h^r(\theta_h)}{\tau(\theta_h)} [z_{\text{eq}}(\theta_h) - z_h]^+ \right) \end{aligned} \quad (5.16)$$

with the matrices and right hand sides introduced in (5.11), (5.12), (5.14) and (5.15). Equation (5.16)₃ is discussed in detail in Section 5.2.5. While the boundary conditions are included in the weak formulation and the definition of the ansatz space, the initial conditions are given by

$$\mathbf{A}_h(x, 0) = \Pi_{\mathbb{W}}(\mathbf{A}_0(x)), \quad \theta_h(x, 0) = \Pi_V(\theta_0(x)) \quad \text{and} \quad z_h(x, 0) = 0. \quad (5.17)$$

The main challenge for the Galerkin method is the definition of the finite dimensional spaces V_h , \mathbb{W}_h and the corresponding basis functions. As a special type of the Galerkin method, a popular approach is the finite element method, where the computational domain is decomposed into simple subdomains and the basis functions are defined locally. They are only non-vanishing on a small number of subdomains, which leads to sparse matrices (5.11) and (5.14). Introducing a time discretization and a suitable linearization strategy, cf. Section 5.3, the resulting linear system of equations can be effectively solved by direct or iterative methods. In the next section, an overview of the finite element method is presented and a definition of the previously introduced finite dimensional spaces V_h and \mathbb{W}_h is given.

5.2. An overview of the finite element method

The construction of the test- and ansatz-functions for the finite dimensional spaces V_h and \mathbb{W}_h is the content of this section. We use the finite element method, which is based on a decomposition of the computational domain into simple subdomains and a local definition of the basis functions.

The definition of the spaces V_h and \mathbb{W}_h introduced in this section is motivated by the fact that the weak formulation of a linear, continuous problem corresponding to the single model components, equations (5.5) and (5.7), where the material parameters are constant, possess solutions in the Hilbert spaces $W^{1,2}(\Sigma) = H^1(\Sigma)$ and $\mathbb{L}_{\text{curl}}^2(D) = H(\text{curl}, D)$. The notation $H^1(\Sigma)$ and $H(\text{curl}, D)$ is standard in the literature for the case $p = 2$ and used in the following.

As has been shown in Chapter 4 for a reduced, nonlinear induction hardening problem with simplified material parameters, higher regularity or integrability of the solution for the continuous problem is expected. In the case of the full nonlinear problem with temperature dependent parameters, a derivation of existence and regularity results is even more complicated, and a solution in $H^1(\Sigma)$ and $H(\text{curl}, D)$ can not be expected.

Nevertheless, for the discrete problem these spaces are taken as basic concept. The use of the notion of ‘conformity’ for the finite elements introduced in the following

sections refers to the spaces $H^1(\Sigma)$ and $H(\text{curl}, D)$ as solution spaces for corresponding linearized, decoupled, single model components. For the full nonlinear problem, the finite element discretization introduced in the following might be considered as non-conforming, due to the fact that the relations $V_h \subset V$ and $\mathbb{W}_h \subset \mathbb{W}$ might not be established, where V and \mathbb{W} denote the solution spaces of the continuous problem for the temperature and the vector potential, respectively.

5.2.1. The spatial decomposition of the computational domain

To describe the finite element method we need some preliminary assumptions. As in Chapter 4 it is assumed that the domains Ω, Σ and D are bounded and have ‘sufficient smoothness’. For simplicity it is assumed in this chapter that the domains Ω, Σ and D are polyhedral.

The main idea of the finite element method as a special type of the Galerkin method is the decomposition of the domain D into small subdomains K_j , e. g. triangles in 2D or tetrahedrons in 3D, and a local definition of the basis functions. The decomposition of the domain D , denoted as triangulation $\mathcal{T}_h = \{K_j\}_{j \in \mathcal{I}}$, where \mathcal{I} denotes an index set, has to satisfy several conditions. The triangulation is assumed to be regular, i. e. it is a covering of the whole domain

$$D = \bigcup_{j \in \mathcal{I}} K_j, \quad (5.18)$$

the elements are non-overlapping and the intersection of the elements \overline{K}_j is either empty, a point, a common edge or a common face (3D) of the element. We denote the diameter of each element $K \in \mathcal{T}_h$ as h_K . Then, $h = \max_{K \in \mathcal{T}_h} h_K$ is used as a discretization parameter. In order to guarantee convergence of the method as the grid size h tends to zero, further conditions like angle conditions must be satisfied. For details we refer to the literature, e. g. [13, 33]. Together with the triangulation \mathcal{T}_h we associate the set of all vertices \mathcal{V} , the set of all edges \mathcal{E} and the set of all faces \mathcal{F} . Referring to a single element, we will use the subscript K , i. e. the set of all vertices belonging to the element K is denoted by \mathcal{V}_K . A similar notation will be used for vertices belonging to an edge $E \in \mathcal{E}$.

The heat equation is only considered in the workpiece, i. e. on the subdomain Σ . Since $\Sigma \subset D$, the previous assumptions hold for the domain Σ in the same way.

5.2.2. An abstract definition of a finite element

In order to introduce the finite element method in detail, we begin with the general definition of a finite element. Following Ciarlet [17], a finite element is defined as a triple (K, P, Λ) , where

- (i) $K \subset \mathbb{R}^d$ is a bounded and closed set with nonempty interior and Lipschitz-continuous boundary, typically intervals ($d = 1$), triangles ($d = 2$) or tetrahedrons ($d = 3$),
- (ii) P is a finite dimensional space of functions on K , usually polynomials,

- (iii) Λ is the set of degrees of freedom, given as linear forms $N_i : P \rightarrow \mathbb{R}$, $i = 1, \dots, n_K$, defined over the space P .

We denote by n_K the number of degrees of freedom on K , which is equal to the dimension of P .

Two important concepts for the construction of finite elements are unisolvency and conformity. A finite element (K, P, Λ) is said to be unisolvent, if specifying a value for each of the degrees of freedom in Λ uniquely determines a function in P . As a consequence, one obtains the following characterization, [79].

Definition 5.1. *The finite element is unisolvent if there exist functions $\varphi_j \in P$, $j = 1, \dots, n_K$ such that*

$$N_i(\varphi_j) = \delta_{ij} \quad \text{for } i, j = 1, \dots, n_K.$$

The set of functions $\{\varphi_1, \dots, \varphi_{n_K}\} \subset P$ defines the nodal basis of the finite dimensional space P .

In order to describe conformity, we need to introduce the finite element interpolant. Assume we have given an unisolvent finite element (K, P, Λ) and denote by $\{\varphi_1, \dots, \varphi_{n_K}\}$ the nodal basis of the space P . Then for any function $v \in V$, where V denotes some Hilbert-space, the local interpolant is defined as

$$\mathcal{I}_K(v) = \sum_{i=1}^{n_K} N_i(v) \varphi_i. \quad (5.19)$$

The local interpolant \mathcal{I}_K is linear, there holds $N_i(\mathcal{I}_K(v)) = N_i(v)$, $i = 1, \dots, n_K$, for all $v \in V$ and $\mathcal{I}_K(v) = v$ for all $v \in P$, [14].

In order to define the global interpolant, we assume that the computational domain D is subdivided into small subdomains by the regular triangulation \mathcal{T}_h , compare (5.18), and each subdomain K_j is equipped with some shape functions P_j and degrees of freedom Λ_j such that (K_j, P_j, Λ_j) forms a finite element. Then, the global finite element interpolant $\mathcal{I}_{\mathcal{T}}$ is defined elementwise by the local interpolants \mathcal{I}_{K_j} such that

$$\mathcal{I}_{\mathcal{T}}(v)|_{K_j} = \mathcal{I}_{K_j}(v) \quad \text{for all } K_j \in \mathcal{T}_h. \quad (5.20)$$

The concept of conformity states that the finite element approximation of a function $v \in V$ belongs to the space V itself:

Definition 5.2. *A finite element is considered as conforming, if for some Hilbert space V of functions over the domain D and a triangulation \mathcal{T}_h of D there holds*

$$\mathcal{I}_{\mathcal{T}}(v) \in V \quad \text{for all } v \in V. \quad (5.21)$$

In this work, we consider finite element approximations on the spaces $H^1(\Sigma)$ and $H(\text{curl}, D)$. Conforming finite element functions on these spaces are characterized by the following properties, [79].

Lemma 5.3 (Conformity requirements for H^1). *Consider a domain Σ with a triangulation \mathcal{T}_h . Then a function $v : \Sigma \rightarrow \mathbb{R}$ belongs to $H^1(\Sigma)$ if and only if*

- (i) $v|_K \in H^1(K)$ for all $K \in \mathcal{T}_h$,
- (ii) for each common face $f = \overline{K}_1 \cap \overline{K}_2$, $K_1, K_2 \in \mathcal{T}_h$ the trace of $v|_{K_1}$ and $v|_{K_2}$ is the same.

Lemma 5.4 (Conformity requirements for $H(\text{curl})$). *Consider a domain D together with a triangulation \mathcal{T}_h . Then a function $\mathbf{v} : D \rightarrow \mathbb{R}^d$ belongs to $H(\text{curl}, D)$ if*

- (i) $\mathbf{v}|_K \in \mathbb{H}^1(K)$ for all $K \in \mathcal{T}_h$,
- (ii) for each common face $f = \overline{K}_1 \cap \overline{K}_2$, $K_1, K_2 \in \mathcal{T}_h$ the trace of the tangential component $\mathbf{n} \times \mathbf{v}|_{K_1}$ and $\mathbf{n} \times \mathbf{v}|_{K_2}$ is the same.

On the other hand, if $\mathbf{v} \in H(\text{curl}, D)$ and (i) is satisfied, then there holds (ii).

For a conforming finite element method over the space $H^1(\Sigma)$, the global finite element functions, which are defined elementwise, must be continuous across element boundaries. In the case of a conforming finite element method for $H(\text{curl}, D)$, tangential continuity is required, while the normal component can be discontinuous across element boundaries. Remembering the continuity conditions for the magnetic vector potential \mathbf{A} , equation (3.13), Lemma 5.4 shows that the space $H(\text{curl}, D)$ is a natural choice for the magnetic vector potential.

The main effort when constructing a conforming finite element method is to find the sets P and Λ for the domains K_j , $j \in \mathcal{I}$, of the triangulation \mathcal{T}_h . A useful concept is the introduction of a reference domain \widehat{K} . The physical finite element is then given by a bijective transformation of the reference element onto the physical element

$$\Phi_{K_j} : \widehat{K} \rightarrow K_j.$$

It is only necessary to construct the finite element for the reference domain \widehat{K} , which can be of simple shape. The finite element on the physical domain K_j is then given by the transformation above. In addition, many computations such as the evaluation of integrals over K_j can be done on the reference domain \widehat{K} using the transformation Φ_{K_j} .

We will exclusively consider tetrahedral meshes in 3D. A tetrahedron K_j , $j \in \mathcal{I}$, of the triangulation \mathcal{T}_h can be described as the convex hull of its vertices $v_i \in \mathcal{V}_{K_j}$, $i = 1, \dots, 4$, where \mathcal{V}_{K_j} denotes the set of the nodes of K_j . Then,

$$K_j = \{x \in \mathbb{R}^3 : x = \sum_{i=1}^4 \lambda_i v_i, \lambda_i \geq 0, \sum_{i=1}^4 \lambda_i = 1\}.$$

The coordinates λ_i are denoted as the barycentric coordinates. They uniquely correspond to a point $x \in K_j$ by the relations $x = \sum_{i=1}^4 \lambda_i v_i$ and $\sum_{i=1}^4 \lambda_i = 1$.

The reference tetrahedron \widehat{K} is defined as the set

$$\widehat{K} = \{\hat{x} = (\hat{x}_1, \hat{x}_2, \hat{x}_3)^T : 0 \leq \hat{x}_i \leq 1, 0 \leq \hat{x}_1 + \hat{x}_2 + \hat{x}_3 \leq 1\}. \quad (5.22)$$

Then, the barycentric coordinates are given as $\lambda_1 = \hat{x}_1$, $\lambda_2 = \hat{x}_2$, $\lambda_3 = \hat{x}_3$ and $\lambda_4 = 1 - \hat{x}_1 - \hat{x}_2 - \hat{x}_3$. In this case, the transformation from the reference domain \widehat{K} onto the physical domain K_j can be described by an affine linear mapping

$$\Phi_{K_j}(\hat{x}) = \mathbf{B}_{K_j}\hat{x} + b_{K_j} \quad \text{with} \quad \mathbf{B}_{K_j} \in \mathbb{R}^{3 \times 3}, b_{K_j} \in \mathbb{R}^3. \quad (5.23)$$

The Jacobian $\mathbf{F}_{K_j} = \partial\Phi_{K_j}/\partial\hat{x}$ and the determinant $J_{K_j} = \det \mathbf{F}_{K_j}$, which are used to transform between the reference and the physical element, are then constant on each element K_j .

With these abstract considerations, we are now able to introduce the finite elements for the spaces $H^1(\Sigma)$ that are used to discretize the heat equation and for $H(\text{curl}, D)$ for the vector potential equation.

5.2.3. Finite elements for H^1

For the finite element discretization of the space $H^1(\Sigma)$ standard linear P_1 -finite elements on tetrahedral meshes are used. The domain K is chosen as the reference tetrahedron \widehat{K} introduced above. Then the finite element $(\widehat{K}, P, \Lambda)$ is defined by

- the polynomial space $P = P_1(\widehat{K})$ with $\dim P_1(\widehat{K}) = 4$,
- the degrees of freedom are given by point evaluations of the basis functions at the vertices, i. e.

$$N_i : v \rightarrow v(V_i) \quad \text{for} \quad i = 1, \dots, 4.$$

The basis functions associated to these degrees of freedom are given on the reference element \widehat{K} by

$$\varphi_i(\hat{x}) = \lambda_i(\hat{x}) \quad \text{for} \quad i = 1, \dots, 4. \quad (5.24)$$

The finite element $(\widehat{K}, P, \Lambda)$ given above is unisolvent, cf. e. g. [86].

The finite element on the physical domain $K_j \in \mathcal{T}_h$ is given by the transformation $\Phi_{K_j} : \widehat{K} \rightarrow K_j$ as introduced in (5.23). A scalar function $\hat{v} \in H^1(\widehat{K})$ defined on the reference domain transforms to v related to the physical element according to

$$v \circ \Phi_{K_j} = \hat{v},$$

i. e. by just a change of variables. By the chain rule, the gradient is given as

$$(\nabla v) \circ \Phi_{K_j} = \mathbf{F}_{K_j}^{-1} \widehat{\nabla} \hat{v}, \quad (5.25)$$

where $\widehat{\nabla}$ denotes the gradient on the reference domain \widehat{K} . For the transformed function v there holds $v \in H^1(K)$, [55].

In order to obtain the global finite element space V_h to discretize functions in $H^1(\Sigma)$ we identify the locally defined degrees of freedom with the global degrees of freedom given by the nodal values of the triangulation \mathcal{T}_h . The global finite element shape functions are obtained by piecing together the locally defined basis functions on each

element transformed to the physical domains $K_j \in \mathcal{T}_h$. Finally, the space V_h is defined as

$$V_h = \bigoplus_{V_i \in \mathcal{V}} \text{span}\{\varphi_i\}, \quad (5.26)$$

where \mathcal{V} denotes the set of vertices of the triangulation \mathcal{T}_h .

Since the shape functions φ_i are defined by the barycentric coordinates, (5.24), the shape functions are continuous across interelement boundaries. As a consequence, the constructed finite element space V_h is conforming with respect to $H^1(\Sigma)$, i.e. $V_h \subset H^1(\Sigma)$, cf. Lemma 5.3. With the finite element space as constructed above, the space V_h consist of piecewise linear functions that are globally continuous and have weak first derivatives [86],

$$V_h = \{v \in H^1(\Sigma) : v|_K \in P_1(K) \text{ for all } K \in \mathcal{T}_h\}. \quad (5.27)$$

Higher order methods can be constructed in the same general framework. For details we refer to the literature, e.g. [17, 86].

5.2.4. Finite elements for $H(\text{curl})$

In this section, we introduce the finite element discretization for the space $H(\text{curl}, D)$. Due to the continuity properties of the electromagnetic fields arising in Maxwell's equations, see Section 3.1.2, it is not appropriate to use vector valued finite element spaces, whose components are discretized by finite elements for $H^1(D)$ as introduced above.

The magnetic vector potential \mathbf{A} for example has only continuous tangential components, cf. equation (3.13). In normal direction, jumps might occur at material interfaces. Consequently, using H^1 -finite elements, which provide continuity in all components, would lead to computational errors. The discontinuity properties of the vector potential \mathbf{A} must be considered in the construction of the finite element method.

The elements we define for the discretization of the vector potential equation go back on Nédélec [57, 58]. We will only consider lowest order Nédélec elements of first and second kind.

Nédélec elements of first kind

The lowest order $H(\text{curl})$ -conforming finite element on the reference tetrahedron \widehat{K} is given by

- the polynomial space $P = \mathcal{N}_0(\widehat{K})$ defined by

$$\mathcal{N}_0(\widehat{K}) = \{\mathbf{a} + \mathbf{b} \times \mathbf{x} : \mathbf{a}, \mathbf{b} \in \mathbb{R}^3, \mathbf{x} \in \widehat{K}\} \quad \text{with} \quad \dim(\mathcal{N}_0(\widehat{K})) = 6 \quad (5.28)$$

- and the edge based degrees of freedom

$$N_\alpha : \mathbf{v} \rightarrow \int_{E_\alpha} \mathbf{v} \cdot \boldsymbol{\tau} \, dx \quad \text{for} \quad \alpha = 1, \dots, 6,$$

where E_α , $\alpha = 1, \dots, 6$ denotes the edges of the tetrahedron \widehat{K} and $\boldsymbol{\tau}$ the uniquely defined tangential vector of the edge E_α .

The degrees of freedom refer to the integral of the tangential component of \boldsymbol{v} . This is the reason why Nédélec elements are often referred to as *edge elements*.

Regarding the polynomial degree of the space $\mathcal{N}_0(\widehat{K})$, it lies between the polynomial spaces of order 0 and 1, i. e. there holds

$$[P_0(\widehat{K})]^3 \subset \mathcal{N}_0(\widehat{K}) \subset [P_1(\widehat{K})]^3.$$

The space is constructed in such a way that the curl of the vector fields are piecewise constant functions, i. e.

$$\operatorname{curl} \mathcal{N}_0(\widehat{K}) = [P_0(\widehat{K})]^3.$$

The basis functions $\boldsymbol{\psi}_\alpha$ associated to the edge based degrees of freedom N_α , $\alpha = 1, \dots, 6$ are given as follows, see e. g. [86],

$$\boldsymbol{\psi}_\alpha^0 = \lambda_{\alpha_2} \nabla \lambda_{\alpha_1} - \lambda_{\alpha_1} \nabla \lambda_{\alpha_2} \quad (5.29)$$

for each edge $E_\alpha \in \mathcal{E}_{\widehat{K}}$ connecting the vertices V_{α_1} and V_{α_2} and λ_{α_i} denoting the barycentric coordinate associated to the vertex V_{α_i} . The tangential trace of the shape function is constant on each edge of \widehat{K} , there holds

$$\boldsymbol{\psi}_\alpha^0 \cdot \boldsymbol{\tau}_{E_\beta} = \frac{1}{|E_\beta|} \delta_{\alpha\beta} \quad \text{for edges } E_\alpha, E_\beta \in \mathcal{E}_{\widehat{K}}, \alpha, \beta = 1, \dots, 6.$$

As a consequence there holds $N_\beta(\boldsymbol{\psi}_\alpha) = \int_{E_\alpha} \boldsymbol{\psi}_\alpha^0 \cdot \boldsymbol{\tau} \, dx = \delta_{\alpha\beta}$, i. e. the finite element $(\widehat{K}, \mathcal{N}_0(\widehat{K}), \Lambda)$ is unisolvent.

Nédélec elements of second kind

The Nédélec element of second kind extends the polynomial space to the full space of polynomials of degree at most one. It is defined by the following characterization.

- The polynomial space $P = \mathcal{N}_1(\widehat{K})$ is given by

$$\mathcal{N}_1(\widehat{K}) = [P_1(\widehat{K})]^3 \quad \text{with} \quad \dim(\mathcal{N}_1(\widehat{K})) = 12, \quad (5.30)$$

- the edge based degrees of freedom Λ are now represented by the following moments on each edge E_α , $\alpha = 1, \dots, 6$

$$N_\alpha^k : \boldsymbol{v} \rightarrow \int_{E_\alpha} \boldsymbol{v} \cdot \boldsymbol{\tau} \, q_k \, dx \quad \text{for } k = 0, 1,$$

where $\{q_k\}$ denotes a basis for $P_1(E_\alpha)$ and $q_0 = 1$.

The vector valued basis functions $\boldsymbol{\psi}_\alpha^k$ associated to the degrees of freedom N_α^k , $\alpha = 1, \dots, 6$ and $k = 0, 1$ for each edge $E_\alpha \in \mathcal{E}_{\widehat{K}}$ connecting the vertices V_{α_1} and V_{α_2} are now given as

$$\begin{aligned}\boldsymbol{\psi}_\alpha^0 &= \lambda_{\alpha_2} \nabla \lambda_{\alpha_1} - \lambda_{\alpha_1} \nabla \lambda_{\alpha_2} \\ \boldsymbol{\psi}_\alpha^1 &= \nabla(\lambda_{\alpha_1} \lambda_{\alpha_2}).\end{aligned}\tag{5.31}$$

The functions $\{\boldsymbol{\psi}_\alpha^0, \boldsymbol{\psi}_\alpha^1\}$ form a basis for the lowest order Nédélec element of second kind $(\widehat{K}, \mathcal{N}_1(\widehat{K}), \Lambda)$, compare to [86].

Global shape functions

The shape functions defined above refer to the reference domain \widehat{K} . In order to obtain the shape functions on the physical domains $K_j \in \mathcal{T}_h$, we use the transformation (5.23). The transformation of a vector valued function $\widehat{\boldsymbol{w}} \in H(\text{curl}, \widehat{K})$ is a bit more involved than in the case of $H^1(\widehat{K})$. Since $\text{curl} \nabla v = 0$ for $v \in H^1(\widehat{K})$, we have that $\nabla v \in H(\text{curl}, \widehat{K})$. Consequently, a function $\widehat{\boldsymbol{w}} \in H(\text{curl}, \widehat{K})$ should transform according to (5.25) in the following way

$$\boldsymbol{w} \circ \Phi_K = \boldsymbol{F}_K^{-1} \widehat{\boldsymbol{w}}.$$

The curl transforms according to

$$(\text{curl} \boldsymbol{w}) \circ \Phi_K = \frac{1}{\det \boldsymbol{F}_K} \boldsymbol{F}_K (\text{curl}_{\widehat{x}} \widehat{\boldsymbol{w}}),$$

where $\text{curl}_{\widehat{x}}$ refers to the curl with respect to the reference domain \widehat{K} . As a consequence, there holds $\boldsymbol{w} \in H(\text{curl}, K)$ for \boldsymbol{w} defined on the physical domain, compare e. g. [55].

In order to obtain the global finite element spaces W_h^0 and W_h^1 consisting of Nédélec elements of first and second kind, respectively, we identify the locally defined degrees of freedom with the global degrees of freedom defined as the tangential traces along the edges of the triangulation \mathcal{T}_h . The global finite element shape functions are obtained by piecing together the locally defined basis functions on each element transformed to the physical domains $K_j \in \mathcal{T}_h$ such that

$$W_h^0 = \bigoplus_{E_k \in \mathcal{E}} \text{span}\{\boldsymbol{\psi}_k^0\}\tag{5.32}$$

for Nédélec elements of first kind and

$$W_h^1 = \bigoplus_{E_k \in \mathcal{E}} \text{span}\{\boldsymbol{\psi}_k^0, \boldsymbol{\psi}_k^1\}\tag{5.33}$$

for Nédélec elements of second kind, where \mathcal{E} denotes the set of edges of \mathcal{T}_h .

The constructed finite element discretizations with Nédélec elements of first and second kind are unisolvent and conforming with respect to $H(\text{curl}, D)$. For a proof of this result we refer to the literature, e. g. [55, 57, 58].

Since the degrees of freedom are defined as the tangential components along the edges of the triangulation, the global orientation of the tangential vectors of the edges has to be taken into account when considering the identification of the local and physical degrees of freedom. Depending on the fact whether the tangential vectors in the description of the reference element and the physical element have the same or the opposite orientation, the transformed shape functions have to be multiplied with $+1$ or -1 when addressing the global shape functions.

Summarizing, the introduced $H(\text{curl})$ -conforming finite element spaces can be written as

$$\begin{aligned} W_h^0 &= \{\mathbf{v} \in H(\text{curl}, D) : \mathbf{v}|_K \in \mathcal{N}_0(K) \text{ for all } K \in \mathcal{T}_h\} \\ W_h^1 &= \{\mathbf{v} \in H(\text{curl}, D) : \mathbf{v}|_K \in \mathcal{N}_1(K) \text{ for all } K \in \mathcal{T}_h\} \end{aligned}$$

with $\mathcal{N}_0(K)$ and $\mathcal{N}_1(K)$ introduced in (5.28) and (5.30), cf. [86].

As a result, we are now able to define the discrete spaces V_h and \mathbb{W}_h for the Galerkin method. The space V_h is chosen as the standard linear P_1 -finite elements, compare (5.27). For the space \mathbb{W}_h we choose either lowest order Nédélec elements of first or second kind. Nédélec elements of first kind are weakly divergence free, which has advantages in realizing the condition $\text{div } \mathbf{A}_h = 0$. For Nédélec elements of second kind, the additional degrees of freedom provide a better approximation of the field \mathbf{A}_h itself. Essential boundary conditions must be included in the ansatz space, such that we define

$$\mathbb{W}_h = \{\mathbf{v}_h \in W_h^k : \mathbf{v}_h \times \mathbf{n} = 0 \text{ on } \partial D\}$$

with $k = 0$ for lowest order Nédélec elements of first kind and $k = 1$ for lowest order Nédélec elements of second kind.

5.2.5. About the spatial discretization of the phase fraction

Having introduced the finite element method, the discretization of the volume fraction of austenite z is considered again. In the continuous setting there holds, cf. (5.1)

$$\partial_t z = \frac{z^{r(\theta)}}{\tau(\theta)} [z_{\text{eq}}(\theta) - z]^+ \quad \text{in } \Sigma \quad \text{for } t \in (0, T).$$

The discretized phase fraction z_h was introduced by the ansatz $z_h = \sum_{i=1}^N z_i(t) \varphi_i(x)$, where $\{\varphi_1, \dots, \varphi_N\}$ denotes the basis of V_h , compare to (5.4). The transition from z to z_h is realized by the nodal interpolation operator $\mathcal{I}_{\mathcal{T}}$ introduced in Section 5.2.2: On each element it is defined as

$$\mathcal{I}_K(v) = \sum_{i=1}^{n_K} N_i(v) \varphi_i,$$

where N_i , $i = 1, \dots, n_K$ denote the local degrees of freedom on a single element K . This interpolation operator is extended to the whole domain by defining the global

interpolation operator $\mathcal{I}_{\mathcal{T}}$ such that

$$\mathcal{I}_{\mathcal{T}}(v)|_{K_j} = \mathcal{I}_{K_j}(v) \quad \text{for all } K_j \in \mathcal{T}_h,$$

compare to (5.20). Consequently, the coefficients $z_i(t)$ correspond to the degrees of freedom N_i on each domain $K_j \in \mathcal{T}_h$, i. e. on V_h they represent the nodal values.

Since the interpolation operator is linear, we obtain from $z_h = \mathcal{I}_{\mathcal{T}}(z)$ an analogous expression for the time derivative of z_h such that $\partial_t z_h = \mathcal{I}_{\mathcal{T}}(\partial_t z)$. Consequently, on the discrete level there holds the following rate law for the volume fraction of austenite

$$\partial_t z_h = \mathcal{I}_{\mathcal{T}}(\partial_t z) = \mathcal{I}_{\mathcal{T}} \left(\frac{z^{r(\theta)}}{\tau(\theta)} [z_{\text{eq}}(\theta) - z]^+ \right). \quad (5.34)$$

In order to evaluate the projection operator for the right hand side of the rate law above, we have to determine the nodal values on each element $K_j \in \mathcal{T}_h$. Since θ and z are discretized by linear P_1 -finite elements, this is realized by evaluating the right hand side of equation (5.34) for the nodal values of θ_h and z_h such that for z_h there holds the following equation

$$\partial_t z_i = \frac{z_i^{r(\theta_i)}}{\tau(\theta_i)} [z_{\text{eq}}(\theta_i) - z_i]^+, \quad i = 1, \dots, N, \quad (5.35)$$

where $\theta_i(t)$ and $z_i(t)$ are the coefficients of the finite element functions $\theta_h(x, t)$ and $z_h(x, t)$, cf. (5.4).

5.3. Discretization in time and nonlinear behaviour

5.3.1. Discretization in time

The semi-discretized equations (5.16) are still continuous in time. They represent a system of nonlinear ordinary differential equations, which has to be solved in time to obtain the time dependent finite element solution of the magnetic vector potential, the temperature and the phase fraction of austenite. The nonlinear ODE system (5.16) can be written in the following general form

$$\frac{\partial y}{\partial t} = R(t, y), \quad y(0) = y_0, \quad (5.36)$$

where y is the vector consisting of the finite element representations $(\underline{A}, \underline{\theta}, \underline{z})$. $R(t, y)$ denotes the right hand side, which is obtained by the spatial discretization of the partial differential equations and y_0 denotes the initial solution. In order to solve such kind of systems, a discretization with respect to time is necessary.

When using the finite element method to solve parabolic equations, the resulting ordinary differential equations are stiff systems, [33]. In order to avoid very small time steps, methods with certain stability properties should be used, e. g. A -stability, where the region of stability contains the complete left half-space of the complex plane [35]. Methods that are A -stable are among many others the implicit Euler method, the

midpoint rule, the α -method¹ with $\alpha \geq 1/2$ and the Backward-Differential-Formula of order two (BDF-2). The midpoint rule, the α -method with $\alpha = 1/2$ and the BDF-2 method approximate the time derivative with an accuracy of order two, while the other methods are only of order one. In addition, the BDF-2 method is also L -stable, which is a stronger property than A -stability. In this section, we introduce these methods to solve the semi-discretized system (5.16) in time.

To explain the different methods, it is assumed that the whole time interval is divided into equidistant time steps $0 < \dots < t_k < \dots < T$. The time derivative is approximated by finite differences

$$\frac{\partial y}{\partial t} \approx \frac{y^{k+1} - y^k}{\tau},$$

where $\tau = t^{k+1} - t^k$ denotes the time step and $y^k = y(t^k)$.

The α -method is defined by an interpolation of the right hand side $R(t, y)$ evaluated at times t^{k+1} and t^k . The integration of equation (5.36) is obtained by solving the following scheme for y^{k+1}

$$\frac{y^{k+1} - y^k}{\tau} = \alpha R(t^{k+1}, y^{k+1}) + (1 - \alpha)R(t^k, y^k). \quad (5.37)$$

The parameter α is used to control the implicit behaviour of the solution method from explicit ($\alpha = 0$) to fully implicit. For $\alpha = 1$ there results the implicit Euler method, the case $\alpha = 1/2$ corresponds to the Crank-Nicolson scheme [19].

The BDF-2 method is a two-step method, see e. g. [35]. Computing the new iterate y^{k+1} involves the previous two time steps by solving the time stepping scheme

$$\frac{3y^{k+1} - 4y^k + y^{k-1}}{2\tau} = R(t^{k+1}, y^{k+1}). \quad (5.38)$$

The Crank-Nicolson method and the BDF-2 method approximate the time derivative with order two. Since the time derivative of the magnetic vector potential is used to evaluate the Joule heat, $Q = \sigma |\partial_t \mathbf{A}|^2$, we are interested in an accurate approximation of this term and we use the BDF-2 method to solve the vector potential equation in time. Since this method represents a multistep method, two initial values are necessary, which are generated consistently by the Crank-Nicolson method.

5.3.2. Nonlinearities

The methods above are implicit (except for $\alpha = 0$), the nonlinear right hand side has to be evaluated at the actual time step t^{k+1} and at $y^{k+1} = y(t^{k+1})$, which is the unknown quantity. Suitable methods have to be used to resolve these nonlinearities.

Typically, Newton type methods are used to solve nonlinear equations. For this, we write the integration schemes (5.37) or (5.38) in the form

$$F(y^{k+1}) = 0. \quad (5.39)$$

¹In literature, the α -method is usually denoted as θ -method. Since we denote the temperature by θ , we use the parameter α instead.

The Newton method is typically derived by linearizing equation (5.39) with respect to some known value \bar{y} , i. e.

$$F(y^{k+1}) \approx F(\bar{y}) + \nabla F(\bar{y})(y^{k+1} - \bar{y}),$$

where $\nabla F(\bar{y})$ denotes the derivative of F with respect to y^{k+1} evaluated at \bar{y} . Denoting $\delta y = (y^{k+1} - \bar{y})$ as the update increment, we can write the Newton algorithm to compute y^{k+1} using the solution at the actual time step y^k as initial value as follows.

- (i) Define an initial value $\bar{y} = y^k$,
- (ii) solve the linear system $\nabla F(\bar{y}) \delta y = -F(\bar{y})$,
- (iii) update $y^{k+1} = \bar{y} + \delta y$,
- (iv) go to step (ii) with $\bar{y} = y^{k+1}$ and iterate until some stopping criterion is satisfied, e. g. $\|\delta y\| \leq \varepsilon$.

Often in application, only a fixed number of Newton steps, in the simplest case only one Newton step, is performed to compute the solution at the new time step y^{k+1} using the iterate y^k as initial guess. The Newton method converges super-linearly, provided the initial guess is close to the exact solution. We refer to the literature for a convergence analysis, e. g. [20].

The complicated task is to evaluate the Jacobian matrix ∇F . Since the material parameters depend nonlinearly on the unknown temperature, phase fraction and even the magnetic vector potential, the computation of the derivative involves also the derivative of the stiffness and mass matrix (5.11) and (5.14) with respect to the unknowns $(\underline{A}, \varrho, \underline{z})$. The solution of the nonlinear system by Newton's method consisting of the repeatedly evaluation of the Jacobian matrix ∇F and the iteration algorithm given above is computational quite expensive.

We want to avoid the iterative solution by the Newton method and propose a semi-implicit algorithm. With this method, the right hand side $R(t, y)$ in (5.36) is only evaluated implicitly at time t^{k+1} for linear terms. Nonlinear terms, especially the material parameters, are evaluated at the old time step t^k . This is also comparable to the method of freezing coefficients, see e. g. [33].

Considering the vector potential equation (5.13) discretized by the Crank-Nicolson scheme in time leads to the following system

$$\mathbf{M}_\sigma(\underline{A}^{k+1} - \underline{A}^k) = -\frac{\tau}{2}\mathbf{K}_\mu(\underline{A}^{k+1} + \underline{A}^k) + \frac{\tau}{2}(\hat{J}^{k+1} + \hat{J}^k),$$

where the matrices \mathbf{M}_σ and \mathbf{K}_μ , cf. (5.14), are assembled with the material parameters evaluated at time t^k . Since the source current density depends only on time, we define $\hat{J}^{k+1} = \{\hat{J}_j(t^{k+1})\}_j$ with $\hat{J}_j(t^{k+1}) = \int_D \mathbf{J}_{\text{src}}(t^{k+1}) \cdot \boldsymbol{\psi}_j \, dx$. In each time step, we have to solve the following linear system

$$\left(\mathbf{M}_\sigma + \frac{\tau}{2}\mathbf{K}_\mu\right)\underline{A}^{k+1} = \left(\mathbf{M}_\sigma - \frac{\tau}{2}\mathbf{K}_\mu\right)\underline{A}^k + \frac{\tau}{2}(\hat{J}^{k+1} + \hat{J}^k). \quad (5.40)$$

In the case of the BDF-2 method, the following linear system results

$$(3\mathbf{M}_\sigma + 2\tau\mathbf{K}_\mu)\underline{\mathbf{A}}^{k+1} = 4\mathbf{M}_\sigma\underline{\mathbf{A}}^k - \mathbf{M}_\sigma\underline{\mathbf{A}}^{k-1} + 2\tau\hat{\mathbf{J}}^{k+1}.$$

Compared to the Crank-Nicolson method, the system matrix differs only by the coefficients in front of the mass- and the curl-curl-matrix.

The big advantage of the semi-implicit method is that it is possible to decouple the system of equations. The discrete vector potential equation above depends only on the magnetic vector potential $\underline{\mathbf{A}}^{k+1}$ evaluated at t^{k+1} while the temperature and the phase fraction are given quantities from the previous time step. Analogously, this holds true for the discretized heat equation.

For the time discretization of the rate law (5.35) we propose the following scheme. Since the right hand side is nonlinear, the phase fraction is computed by an explicit Euler scheme

$$\underline{z}^{k+1} = \underline{z}^k + \tau \left(\frac{(\underline{z}^k)^{r(\underline{\theta}^k)}}{\tau(\underline{\theta}^k)} [z_{\text{eq}}(\underline{\theta}^k) - \underline{z}^k]^+ \right), \quad (5.41)$$

where the evaluation of the right hand side has to be understood componentwise.

If we consider the time discretization of the heat equation by the implicit Euler method, there results the following equation

$$(\mathbf{D}_{\rho c} + \tau\mathbf{S}_\kappa)\underline{\theta}^{k+1} = \mathbf{D}_{\rho c}\underline{\theta}^k + \tau\hat{\mathbf{F}}^k, \quad (5.42)$$

where $\hat{\mathbf{F}}^k = \{\hat{F}_j^k\}_j$ with $\hat{F}_j^k = \int_\Sigma (\sigma |\partial_t \mathbf{A}_h^k|^2 - \rho \mathcal{L} \partial_t z_h^k) \varphi_j \, dx + \int_{\partial\Sigma} g \varphi_j \, da$. The right hand side $\hat{\mathbf{F}}^k$ consists of the time derivatives of \mathbf{A}_h and z_h at time t^k . Since the discrete equations are decoupled, the time derivatives can be computed by a forward difference quotient using the new iterates for \mathbf{A}_h and z_h , i. e.

$$\partial_t \mathbf{A}_h^k = \tau^{-1} \sum_{i=1}^{\tilde{N}} (A_i^{k+1} - A_i^k) \psi_i \quad \text{and} \quad \partial_t z_h^k = \tau^{-1} \sum_{i=1}^N (z_i^{k+1} - z_i^k) \varphi_i. \quad (5.43)$$

As we will see in the next section, the electromagnetic effects and the heat diffusion occur on different time scales. With the decoupling of the equations by a semi-implicit discretization it is possible to solve Maxwell's equations, the heat equation and the rate law for the volume fraction of austenite, which is directly related to the temperature, on different time scales.

5.3.3. Different time scales for heat diffusion and electromagnetic effects

The induction heating problem can be regarded as a multi scale problem in time. The typical time scale on which the temperature changes is by magnitudes larger than the time scale of Maxwell's equations. The time scale of the heat equation is determined by the typical diffusion length. The crucial factors are the physical parameters such as the heat conductivity, the specific heat and a length scale parameter. The time scale

for the heat diffusion is determined by a dimensional analysis as carried out in this section. As we will see, it lies in the range of seconds. The time scale of the vector potential equation is determined by the oscillatory source term. For the frequency range considered in this work it lies in the range of $10^{-6} - 10^{-5}$ s.

In order to determine the time scale of the heat diffusion, we consider the energy balance in its dimensional form, compare (5.1),

$$\rho c_p \frac{\partial \theta}{\partial t} - \operatorname{div} \kappa \nabla \theta = \hat{f}$$

with $\hat{f} = \sigma |\partial \mathbf{A} / \partial t|^2 - \rho \mathcal{L} \partial z / \partial t$. We introduce a dimensionless time $\tilde{t} = t / \tau$ with time scale τ and a dimensionless spatial variable $\tilde{x} = x / X$, where X denotes a length scale parameter, e.g. the penetration depth of the eddy currents. Introducing these quantities into the heat equation above, we obtain

$$\frac{\rho c_p}{\tau} \frac{\partial \theta}{\partial \tilde{t}} - \operatorname{div}_{\tilde{x}} \frac{\kappa}{X^2} \tilde{\nabla} \theta = \hat{f},$$

where $\operatorname{div}_{\tilde{x}}$ and $\tilde{\nabla}$ denote the divergence and the gradient with respect to coordinates \tilde{x} . Assuming the specific heat capacity c_p to be constant for the moment, we can write this equation as

$$\frac{\partial \theta}{\partial \tilde{t}} - \operatorname{div}_{\tilde{x}} \tilde{\kappa} \tilde{\nabla} \theta = \hat{f}$$

with a dimensionless heat diffusion coefficient

$$\tilde{\kappa} = \frac{\kappa \tau}{\rho c_p X^2} \quad (5.44)$$

and a modified right hand side \hat{f} . Introducing typical material parameters for the case of steel and a typical diffusion length, it is possible to define the typical time scale τ such that the dimensionless diffusion coefficient $\tilde{\kappa}$ is of order one. The length scale lies in the range of some millimetres. This corresponds to the boundary layer of the workpiece that is affected by the inductive heating. With the values $c_p = 600$ J/kg K, $\rho = 7800$ kg/m³, $X = 3$ mm and $\kappa = 40$ W/m K we obtain

$$\tau \approx 1 \text{ s},$$

i.e. the typical time scale for the heat diffusion lies in the order of seconds, while the time scale for the electromagnetic effects lies in the range of fractions of milliseconds. The difference of the time scales is of order 10^5 up to 10^6 .

As a consequence, it is not possible to use a single time step for solving the semi-discretized system (5.16) with respect to time. The highly oscillating magnetic field requires a very small time step lying in the range of $\delta t = 10^{-6}$ and smaller. Using the same time step to solve the heat equation within typical time intervals up to 1 s would produce too many time steps that even today's modern computers can not solve within reasonable time. We will consider a discretization of system (5.16) with different time scales as described in the following.

5.3.4. Time discretization of the coupled system

Introduction of different time steps

Since the heat conduction and the electromagnetic effects exhibit different time scales, it is the aim to decouple system (5.16) and solve the time dependent equations with different time step sizes, as it is the usual approach for induction heating problems in the time domain, [18].

If we consider the vector potential equation (5.1)₁ for a given temperature θ , then it represents a parabolic equation that possesses a time periodic solution due to the time periodic source term. We solve this equation for some periods using a time stepping scheme with time step size δt .

The heat equation (5.1)₂ also represents a parabolic equation with rapidly varying right hand side $\sigma |\partial_t \mathbf{A}|^2$. As we have seen, the temperature changes at a time scale that is much larger than the one of the right hand side, which is governed by the frequency of the source current. The usual approach is to approximate the Joule heat term by its average over one period, [18]. Then, the heat equation can be solved using time steps $\Delta t \gg \delta t$, where the oscillating Joule heat is replaced by an averaged Joule heat term, which is obtained from the periodic solution of the vector potential equation. For a further justification of this approach, see also Appendix A.3.

We formulate the algorithm following [18]. We consider the time interval $(0, T)$ and decompose it into M equal time steps t^k with time step size $\Delta t = T/M$ such that

$$t^k = k\Delta t \quad \text{for } k = 1, \dots, M.$$

The ‘large’ time step size Δt results from the typical time scale of the heat conduction. We obtain time intervals (t^k, t^{k+1}) , $k = 0, \dots, M-1$, on which we solve the electromagnetic problem with the assumption that the temperature is constant. For this we use a time step $\delta t \ll \Delta t$ that is related to the source term of the vector potential equation. We obtain a decomposition of the intervals (t^k, t^{k+1}) such that

$$t^{k,l} = t^k + l\delta t \quad \text{for } l = 0, 1, \dots$$

and solve the vector potential equation by the time stepping scheme introduced in Section 5.3.2. In general, it is not necessary to solve for \mathbf{A}_h on the whole interval (t^k, t^{k+1}) . Since the source term \mathbf{J}_{src} is periodic, the discrete solution \mathbf{A}_h is periodic such that it is sufficient to solve until a periodic solution is obtained. This is realized by solving the vector potential equation for a fixed number of periods. Numerical tests using the L -stable BDF-2 time stepping method have shown that a periodic vector potential \mathbf{A}_h is obtained after two, at most three periods. As an alternative, a periodicity test can be used to verify that the solution \mathbf{A}_h is periodic.

The Joule heat, which enters the right hand side of the heat equation, is obtained by averaging the term $\sigma |\partial_t \mathbf{A}_h|^2$ over one period,

$$\bar{Q} = \frac{\omega}{2\pi} \int_0^{\frac{2\pi}{\omega}} \sigma |\partial_t \mathbf{A}_h|^2 dt. \quad (5.45)$$

The averaged Joule heat \bar{Q} is still time dependent due to the temperature and phase dependent electrical conductivity $\sigma(\theta, z)$, but it is not highly oscillating any more. Finally, we have decoupled the vector potential equation and the heat equation together with the rate law for the phase fraction. Having determined the averaged Joule heat, the heat equation can be solved by a suitable time stepping scheme at the discrete times t^k , $k = 1, \dots, M$.

As a test of periodicity it is suggested in [18] not to compare values of the magnetic vector potential \mathbf{A}_h but to check the periodicity of the magnetic vector potential in terms of the Joule heat $Q = \sigma |\partial_t \mathbf{A}_h|^2$ evaluated at a time step $t^{k,l}$, denoted by Q_1 and one period later, denoted by Q_2 . Then, the authors define quantities

$$\eta_i = \frac{|Q_{2,i} - Q_{1,i}|}{\|Q_2\|}$$

that are evaluated at all points i of the mesh. If the values η_i are below some threshold, then the solution is assumed to be periodic and the averaged Joule heat \bar{Q} is accepted for the computation of the next temperature time step. Otherwise, the time iteration of the vector potential equation is carried out for one more period.

The question that arises with this method is, for which points x_i of the mesh the test is performed. This question is closely related to the fact, how and where the Joule heat

$$Q = \sigma \left| \frac{\partial \mathbf{A}_h}{\partial t} \right|^2,$$

respectively the averaged Joule heat \bar{Q} , is evaluated. Since the discrete vector potential is given as $\mathbf{A}_h(x, t) = \sum_{j=1}^N A_j(t) \psi_j(x)$, where A_j are the tangential components of \mathbf{A}_h along the edges $E_j \in \mathcal{E}$ of the triangulation \mathcal{T}_h , it is hardly possible to express the components of the modulus $|\mathbf{A}| = (|A_x|^2 + |A_y|^2 + |A_z|^2)^{1/2}$ by the finite element representation vector \underline{A} itself. Therefore, in order to compute the Joule heat, it is necessary to evaluate the components of the vector field $\mathbf{A}_h(x, t)$ at finitely many points x_i in space, which involves the evaluation of the components of the vector valued basis functions $\psi_j(x)$ in space. Consequently, one has to specify points x_i at which the Joule heat is evaluated.

One possibility is to evaluate \bar{Q} at the nodes of the triangulation \mathcal{T}_h . In this way, it is easily possible to obtain a finite element interpolant of \bar{Q} with respect to the space V_h . But since the vector potential \mathbf{A}_h might be discontinuous in normal direction at interelement boundaries, this method is connected with approximation errors.

The Joule heat appears at the right hand side of the weak formulation of the heat equation, consisting of the evaluation of integrals like

$$\hat{F}_j = \int_{\Sigma} (\bar{Q} - \rho \mathcal{L} \partial_t z_h) \varphi_j \, dx + \int_{\partial \Sigma} g \varphi_j \, da,$$

compare (5.12). Typically in numerical implementations of finite element methods, quadrature formulas are used to compute integrals by evaluating the integrand at certain quadrature points. Therefore, the averaged Joule heat is computed at the

quadrature points q_i that are also used to evaluate the integrals above during the assembly of the right hand side of the space discretized heat equation. With this method, a higher accuracy than for the evaluation of \bar{Q} at the nodes of \mathcal{T}_h is expected. The periodicity test described above can be performed for the values at the quadrature points, too.

5.3.5. On the existence of solutions for the discretized system

In this section, we consider the existence of solutions for the fully discretized and linearized problem consisting of equations (5.40), (5.41) and (5.42). We search for a solution at the fixed time t^{k+1} assuming that a solution for the previous time step t^k is known. The existence and uniqueness of discrete solutions for the heat equation is a common result. For the phase fraction z_h it can be obtained by standard results on ODEs. Due to the non-trivial kernel of the curl-operator, i. e.

$$\ker(\text{curl}) := \{\mathbf{v} \in H(\text{curl}, D) : \text{curl } \mathbf{v} = 0\} = \nabla H^1(D),$$

the existence of a unique solution for the discretized vector potential \mathbf{A}_h is not trivial.

The foundation is the general theory for the existence and uniqueness of solutions for elliptic problems on some Hilbert space S in terms of the following result.

Lemma 5.5 (Lax-Milgram, [33]). *Let $a(\cdot, \cdot) : S \times S \rightarrow \mathbb{R}$ be a bounded, S -elliptic bilinear form. Then for every $f \in S^*$ the variational equation*

$$a(u, v) = f(v) \quad \text{for all } v \in S$$

possesses a unique solution $u \in S$. Furthermore, there holds the a priori estimate

$$\|u\|_S \leq \frac{1}{\gamma} \|f\|_{S^*}.$$

We apply the general theory to the fully discretized equation (5.40), where the vector potential equation is discretized by the Crank-Nicolson method (the same results hold true for the BDF-2 method). With the definition of the matrices (5.11) this problem is equivalent to

$$a(\mathbf{A}_h^{k+1}, \mathbf{w}_h) = \bar{f}(\mathbf{w}_h) \quad \text{for all } \mathbf{w}_h \in \mathbb{W}_h, \quad (5.46)$$

where the bilinear form $a : \mathbb{W}_h \times \mathbb{W}_h \rightarrow \mathbb{R}$ is defined as

$$a(\mathbf{A}_h, \mathbf{w}_h) = \int_D \sigma \mathbf{A}_h \cdot \mathbf{w}_h \, dx + \frac{\tau}{2} \int_D \mu^{-1} \text{curl } \mathbf{A}_h \cdot \text{curl } \mathbf{w}_h \, dx$$

and the linear functional $\bar{f} \in H(\text{curl}, D)^*$ is given by

$$\begin{aligned} \bar{f}(\mathbf{w}_h) = & \int_D \sigma \mathbf{A}_h^k \cdot \mathbf{w}_h \, dx - \frac{\tau}{2} \int_D \mu^{-1} \text{curl } \mathbf{A}_h^k \cdot \text{curl } \mathbf{w}_h \, dx \\ & + \frac{\tau}{2} \int_D (\mathbf{J}_{\text{src}}(t^{k+1}) + \mathbf{J}_{\text{src}}(t^k)) \cdot \mathbf{w}_h \, dx. \end{aligned}$$

One has to show the boundedness and the coercivity of the bilinear form $a(\cdot, \cdot)$, i. e. $|a(u, v)| \leq M \|u\|_S \|v\|_S$ for all $u, v \in S$ with some constant $M > 0$ and $a(u, u) \geq \gamma \|u\|_S^2$ for all $u \in S$ with a constant $\gamma > 0$

Since the material parameters are evaluated at the previous time step, they represent known quantities depending on space x . As in Chapter 4 the coefficients σ and μ are assumed to be bounded from above and below, cf. Hyp. (H) (i) and (ii). Remember that instead of including the gauging condition $\operatorname{div} \mathbf{A}_h$ into the definition of the ansatz space \mathbb{W}_h , a regularization of the electrical conductivity is introduced, i. e. $\sigma = \sigma_{\text{NC}}$ in $D \setminus (\Sigma \cup \Omega)$ with $0 < \sigma_{\text{NC}} \ll \min\{\sigma_{\text{wp}}, \sigma_{\text{Cu}}\}$, cf. (5.6). Then, for the bilinear form $a(\cdot, \cdot)$ there holds

$$\begin{aligned} a(\mathbf{A}_h, \mathbf{w}_h) &= \int_D \sigma \mathbf{A}_h \cdot \mathbf{w}_h \, dx + \frac{\tau}{2} \int_D \mu^{-1} \operatorname{curl} \mathbf{A}_h \cdot \operatorname{curl} \mathbf{w}_h \, dx \\ &\leq \bar{\sigma} \|\mathbf{A}_h\|_{\mathbb{L}^2} \|\mathbf{w}_h\|_{\mathbb{L}^2} + \frac{\tau}{2} \underline{\mu}^{-1} \|\operatorname{curl} \mathbf{A}_h\|_{\mathbb{L}^2} \|\operatorname{curl} \mathbf{w}_h\|_{\mathbb{L}^2} \\ &\leq \max\{\bar{\sigma}, \frac{\tau}{2} \underline{\mu}^{-1}\} \|\mathbf{A}_h\|_{\operatorname{curl}} \|\mathbf{w}_h\|_{\operatorname{curl}} \end{aligned}$$

for all $\mathbf{A}_h, \mathbf{w}_h$ in $\mathbb{W}_h \subset H(\operatorname{curl}, D)$ equipped with the usual norm on $H(\operatorname{curl}, D)$. On the other hand, there holds

$$\begin{aligned} a(\mathbf{w}_h, \mathbf{w}_h) &= \int_D \sigma \mathbf{w}_h \cdot \mathbf{w}_h \, dx + \frac{\tau}{2} \int_D \mu^{-1} \operatorname{curl} \mathbf{w}_h \cdot \operatorname{curl} \mathbf{w}_h \, dx \\ &\geq \underline{\sigma} \|\mathbf{w}_h\|_{\mathbb{L}^2}^2 + \frac{\tau}{2} \bar{\mu}^{-1} \|\operatorname{curl} \mathbf{w}_h\|_{\mathbb{L}^2}^2 \\ &\geq \min\{\underline{\sigma}, \frac{\tau}{2} \bar{\mu}^{-1}\} \|\mathbf{w}_h\|_{\operatorname{curl}}^2 \end{aligned}$$

for all \mathbf{w}_h in \mathbb{W}_h . Consequently, the bilinear form $a(\cdot, \cdot)$ is bounded and coercive on \mathbb{W}_h . In the case of $\sigma = 0$ in non-conducting regions, coercivity can not be established, since for arbitrary gradient fields $\nabla\phi$ there holds $a(\nabla\phi, \nabla\phi) = 0$ on $D \setminus (\Sigma \cup \Omega)$, but $\|\nabla\phi\|_{\operatorname{curl}} = \|\nabla\phi\|_{\mathbb{L}^2}$. In this case, the gauging condition $\operatorname{div} \mathbf{A}_h$ is necessary. Coercivity can be established for a mixed variational problem, cf. [86].

From Lemma 5.5 one obtains that the discrete equation (5.40) possesses a unique solution, provided the right hand sides are sufficiently regular. Assuming $\mathbf{J}_{\text{src}} \in \mathbb{L}^2(D)$, then there holds $\bar{f} \in \mathbb{L}^2(D)$. Consequently, we have the existence of a unique discrete solution \mathbf{A}_h^{k+1} at the new time step t^{k+1} .

5.3.6. Solution of the linearized systems

In every time step, the time stepping schemes introduced above require the solution of linear systems in the form

$$\mathbf{S}u = b,$$

where $\mathbf{S} = (\mathbf{M}_\sigma + \tau/2\mathbf{K}_\mu)$ in the case of the vector potential equation discretized by the Crank-Nicolson scheme, $\mathbf{S} = (3\mathbf{M}_\sigma + 2\tau\mathbf{K}_\mu)$ for the BDF-2 method, or $\mathbf{S} =$

$(\mathbf{D}_{\rho c} + \tau \mathbf{S}_{\kappa})$ for the heat equation discretized by an implicit Euler scheme, with various right hand sides b . In order to solve these linear systems, direct as well as iterative methods are used.

The heat equation is solved only in the workpiece, the domain Σ . Compared to the vector potential equation, which has to be solved on the whole domain D and is discretized by edge elements, it is possible to use a direct solver. We use the direct sparse solver PARDISO.

The package PARDISO is a high-performance, robust, memory efficient and easy to use software for solving large sparse symmetric and non-symmetric linear systems of equations on shared-memory and distributed-memory architectures. PARDISO calculates the solution of a set of sparse linear equations with multiple right-hand sides using a parallel LU , LDL or LL^T factorization, [66, 67].

For huge systems, direct solvers come to their limits regarding memory usage and computational time. The use of iterative methods, such as the preconditioned conjugate gradient method (PCG) is suggested. For solving Maxwell's equation, the performance of the PCG method with a simple Jacobi preconditioner is due to the ill-conditioned iteration matrix and the non-trivial kernel of the curl-operator quite bad. Special methods like additive Schwarz-methods [86] or multigrid methods [37] are proposed. Their implementation is quite complex.

As an alternative, we use a combination of the direct, high-performance solver PARDISO and the PCG method. Solving the vector potential equation, we have to solve systems $\mathbf{S}u = b$ with varying right hand sides b . In Section 5.5, we introduce an averaging method to linearize the vector potential equation. With this method, we can drop the nonlinear dependence of the magnetic permeability μ on the magnetic field. Then, the iteration matrix $\mathbf{S} = (\mathbf{M}_{\sigma} + \tau/2\mathbf{K}_{\mu})$ does not change during a time step Δt and we propose the following method. We solve the system $\mathbf{S}u = b$ using PARDISO once and store the LU or LL^T -decomposition of \mathbf{S} . Then, it is easily possible to solve the system for various right hand sides b .

In the next time step for the heat equation, $t^k + \Delta t$, the matrices \mathbf{M}_{σ} , \mathbf{K}_{μ} and consequently the iteration matrix \mathbf{S} need to be reassembled. The changes result from the changing temperature, since the material parameters depend on the temperature. If the changes in the temperature θ are small, the differences in σ and μ compared to the previous time step are small. Consequently, the difference between the iteration matrix for subsequent time steps is small. This suggests the use of the LU or LL^T decomposition of the previous time step as preconditioner for a PCG method. This is similar to incomplete Cholesky CG-methods (ICCG) that use an incomplete or inexact Cholesky decomposition of the iteration matrix as a preconditioner.

In the following, we give a sketch of the PCG method. In order to solve the linear system $\mathbf{S}u = b$, where \mathbf{S} is a symmetric, positive definite matrix, the system $\mathbf{C}^{-1}\mathbf{S}u = \mathbf{C}^{-1}b$ is considered, where \mathbf{C} denotes the preconditioner. The PCG method is explained e. g. in [33] and consist of the following steps.

- Starting from an initial value $u^0 \in \mathbb{R}^n$ define vectors

$$p^0 = d^0 = b - \mathbf{S}u^0 \quad \text{and} \quad s^0 = \mathbf{C}^{-1}d^0.$$

- Compute recursively for $k = 0, 1, \dots$ until $\|d^k\| \leq \varepsilon$

$$\begin{aligned} \alpha_k &= \frac{(s^k, d^k)}{(\mathbf{S}p^k, p^k)} \\ u^{k+1} &= u^k + \alpha_k p^k \\ d^{k+1} &= b - \mathbf{S}u^{k+1} \\ s^{k+1} &= \mathbf{C}^{-1}d^{k+1} \\ \beta_k &= \frac{(s^{k+1}, d^{k+1})}{(s^k, d^k)} \\ p^{k+1} &= s^{k+1} + \beta_k p^k. \end{aligned}$$

In order to compute the vectors $s^{k+1} = \mathbf{C}^{-1}d^{k+1}$ one has to solve the system $\mathbf{C}s^{k+1} = d^{k+1}$. It is the aim to construct the preconditioner \mathbf{C} in such a way that $\mathbf{C} \approx \mathbf{S}$ but the system $\mathbf{C}s^{k+1} = d^{k+1}$ can still be solved effectively.

Often, a lower triangular matrix \mathbf{L} is proposed as preconditioner, such that

$$\mathbf{S} = \mathbf{L}\mathbf{L}^T + \mathbf{R},$$

where \mathbf{R} is a remainder with $\|\mathbf{R}\|$ small. The PCG algorithm described before is then applied to the system $(\mathbf{L}^{-1}\mathbf{S}\mathbf{L}^{-T})(\mathbf{L}^T u) = \mathbf{L}^{-1}b$ with the new unknown vector $y = \mathbf{L}^T u$. The solution u itself can be determined by finally solving $\mathbf{L}^T u = y$ by a simple backward substitution. In the special case of $\mathbf{R} = 0$ the complete Cholesky-decomposition of \mathbf{S} is known and the solution can be obtained within one iteration. For the convergence behaviour of the PCG method, we refer to the literature, e. g. [33]. In the case of an incomplete Cholesky-decomposition as preconditioner, the method should converge within a small number of iterations.

For the solution of the vector potential equation, we limit the number of PCG iterations to a fixed number. If the method does not converge for the actual time step within the prescribed number of iterations, the preconditioner must be updated. Then, the system is solved again using the direct solver PARDISO and the newly created LU - or LL^T -decomposition is stored to use it as preconditioner for subsequent time steps. Since the linear systems have to be solved for various right hand sides, the speed up of the PCG method using an LL^T -preconditioner outweighs the computational effort using PARDISO in comparison to the easily computable Jacobi- or Gauss-Seidel-preconditioners.

5.4. Adaptive mesh generation

Solutions to the vector potential equation exhibit only tangential continuity, cf. equation (3.13). At material interfaces, the normal component of \mathbf{A} can be discontinuous or

singularities can occur. In addition, due to the skin effect, the eddy current density is concentrated in the surface region of the workpiece. The electrical power decays exponentially with the distance to the surface. In addition, the magnetic field, respectively the magnetic vector potential \mathbf{A} , decreases to zero away from the inductor.

In order to obtain accurate results, the mesh of the finite element discretization has to be fine enough to resolve material interfaces and the surface area of the workpiece. On the other hand one is interested in reducing the computational cost, especially for 3D computations, such that it is desirable to increase the mesh size in regions that are sufficiently far away from the zone of interest.

Therefore, it is the aim to create an adaptive grid that has a high resolution in the surface area of the workpiece and at interfaces, where material properties might change, and is coarse in regions, where a high accuracy is not necessary.

In order to create adaptive grids, information on the local error of the computed approximative solutions for the magnetic vector potential can be used. These are typically obtained by a posteriori error estimators. These error estimators provide an indicator, which mesh cells need to be refined and which cells might be coarsened.

A posteriori error estimators are a well established tool for the effective numerical solution of elliptic boundary value problems. A general overview with further references can be found in the article [12] and the book by Verfürth [83]. In the following section, an overview is given.

5.4.1. A general adaptive algorithm

It is the aim of every adaptive algorithm to refine the discretization of the computational domain near the critical regions, where e.g. material properties change or singularities in the solution appear, [83]. The question is how such regions can be identified. A posteriori error estimates can deliver reliable and efficient local error indicators that can be extracted from the known numerical solution. In this context, the concept of reliability and effectivity states that the error estimator provides upper and lower bounds for the true error.

If the error indicator is an upper bound of the true error (reliability), it is possible to obtain a numerical solution with a prescribed tolerance ϵ . An inequality in the form ‘error estimate \leq tolerance’ yields that the true error is also smaller than the tolerance, up to a multiplicative constant. The lower bounds are necessary to guarantee that the error is not overestimated and the grid is not refined in regions, where the true error is small (effectivity).

Independent of the specific problem to solve and the problem dependent choice of the error estimator, an adaptive algorithm has the following general structure, [83]:

- (i) Construct an initial coarse mesh \mathcal{T}_k , with $k = 0$.
- (ii) Solve the discrete problem on the triangulation \mathcal{T}_k .
- (iii) Compute the a posteriori error indicator on each element $K \in \mathcal{T}_k$.

- (iv) If the estimated error is below some tolerance ϵ then stop. Otherwise select elements $K \in \mathcal{T}_k$ to refine and create a new mesh. Increment k by 1 and return to (ii).

For time dependent problems, the algorithm has to be modified in order to take the temporal error into account, which arises from the time discretization. This might also result in coarsening of the mesh or even a complete remeshing of the computational domain.

Remark 5.6. *In our adaptive algorithm, we will not consider the discretization errors in time. We only consider the spatial error and derive an error estimator that estimates the error for fixed given times t^k . Since the temporal error is not controlled, the time steps to discretize the vector potential equation and the heat equation have to be taken sufficiently small such that the contribution of the temporal error is of similar order as the spatial error.*

In order to perform step (ii) of the algorithm above, discretization methods and suitable solution algorithms for the discrete problems are necessary. These have been discussed in the preceding sections.

To design an adaptive algorithm one has to specify a local error indicator in form of an a posteriori error estimator, a refinement strategy to select the elements that should be refined and finally, an algorithm to create the new grid. A suitable error estimator for our problem is introduced in Section 5.4.2 based on [7]. Widely used refinement strategies will be shortly introduced in Section 5.4.3. For the solution of our induction hardening problem, we use the grid generator **TetGen**, which in addition to grid generation also provides the functionality of grid refinement.

5.4.2. A residual based error estimator for Maxwell's equation

For finite element approximations with Nédélec elements, one of the first work on a posteriori error estimators has been done by Beck et al. [7]. We use the error estimator introduced in this article to generate adaptive grids for the solution of the induction heating problem. The following explanations are cited from [7].

The authors consider the following general elliptic boundary value problem

$$\begin{aligned} \operatorname{curl} \chi \operatorname{curl} \mathbf{u} + \beta \mathbf{u} &= \mathbf{f} \quad \text{in } D \\ \mathbf{u} \times \mathbf{n} &= 0 \quad \text{on } \partial D, \end{aligned}$$

where $\chi, \beta \in L^\infty(D)$ with χ uniformly positive and $\beta \geq 0$. Such kind of equation emerges for example after the discretization in time of the vector potential equation (5.1), compare also to Section 5.3. Then, \mathbf{u} corresponds to the new approximation of \mathbf{A} , χ is the inverse of the magnetic permeability μ , β corresponds to σ scaled by the time step size and \mathbf{f} includes in addition to the impressed current density \mathbf{J}_{src} the approximation of \mathbf{A} from the previous time step.

The weak formulation is the following, cf. also (5.5). Find $\mathbf{u} \in H_0(\operatorname{curl}, D)$ such that

$$(\chi \operatorname{curl} \mathbf{u}, \operatorname{curl} \boldsymbol{\psi})_{\mathbb{L}^2} + (\beta \mathbf{u}, \boldsymbol{\psi})_{\mathbb{L}^2} = (\mathbf{f}, \boldsymbol{\psi})_{\mathbb{L}^2} \quad \text{for all } \boldsymbol{\psi} \in H_0(\operatorname{curl}, D) \quad (5.47)$$

with $H_0(\text{curl}, D) = \{\mathbf{v} \in H(\text{curl}, D) : \mathbf{v} \times \mathbf{n} = 0 \text{ on } \partial D\}$ and $(\cdot, \cdot)_{\mathbb{L}^2}$ denoting the L^2 -scalar product on D .

Equation (5.47) is discretized by curl-conforming finite elements on a fixed triangulation \mathcal{T}_h . The triangulation is for example taken from a sequence of refined meshes, \mathcal{T}_{h_k} , where \mathcal{T}_{h_0} denotes the coarsest mesh. In [7], Nédélec elements of general order k are considered. The finite element space is denoted by W_h^k , compare Section 5.2.4. Though in the sections above we only introduced lowest order elements (corresponding to $k = 0$ and $k = 1$), we keep the presentation general and consider the following curl-conforming finite element approximation of (5.47).

Find $\mathbf{u}_h \in W_{h,0}^k$ such that

$$(\chi \text{curl } \mathbf{u}_h, \text{curl } \boldsymbol{\psi}_h)_{\mathbb{L}^2} + (\beta \mathbf{u}_h, \boldsymbol{\psi}_h)_{\mathbb{L}^2} = (\mathbf{f}, \boldsymbol{\psi}_h)_{\mathbb{L}^2} \quad \text{for all } \boldsymbol{\psi}_h \in W_{h,0}^k, \quad (5.48)$$

where $W_{h,0}^k = W_h^k \cap H_0(\text{curl}, D)$.

Now it is assumed that $\tilde{\mathbf{u}}_h \in W_{h,0}^k$ is an approximate solution to the exact solution of (5.48), denoted by \mathbf{u}_h , which is obtained by some iterative method. It is the aim to obtain an effective and reliable error estimator for the total error

$$\mathbf{e} = \mathbf{u} - \tilde{\mathbf{u}}_h$$

in the energy norm

$$\|\mathbf{u}\|_E = (\chi \text{curl } \mathbf{u}, \text{curl } \mathbf{u})_{\mathbb{L}^2} + (\beta \mathbf{u}, \mathbf{u})_{\mathbb{L}^2}.$$

Since $W_{h,0}^k \subset H_0(\text{curl}, D)$ there holds for the error $\mathbf{e} \in H_0(\text{curl}, D)$. Inserting \mathbf{e} into the weak form (5.47), the error satisfies the following identity

$$(\chi \text{curl } \mathbf{e}, \text{curl } \boldsymbol{\psi})_{\mathbb{L}^2} + (\beta \mathbf{e}, \boldsymbol{\psi})_{\mathbb{L}^2} = r(\boldsymbol{\psi}) \quad \text{for all } \boldsymbol{\psi} \in H_0(\text{curl}, D), \quad (5.49)$$

where $r(\cdot)$ is defined as the residual

$$r(\boldsymbol{\psi}) = (\mathbf{f}, \boldsymbol{\psi})_{\mathbb{L}^2} - (\chi \text{curl } \tilde{\mathbf{u}}_h, \text{curl } \boldsymbol{\psi})_{\mathbb{L}^2} - (\beta \tilde{\mathbf{u}}_h, \boldsymbol{\psi})_{\mathbb{L}^2}, \quad \boldsymbol{\psi} \in H_0(\text{curl}, D). \quad (5.50)$$

The construction of the error estimator is based on a Helmholtz-type decomposition of the space $H_0(\text{curl}, D)$ such that

$$H_0(\text{curl}, D) = H_0^0(\text{curl}, D) \oplus H_0^\perp(\text{curl}, D), \quad (5.51)$$

where $H_0^0(\text{curl}, D) = \ker H_0(\text{curl}, D) = \{\mathbf{v} \in H_0(\text{curl}, D) : \text{curl } \mathbf{v} = 0\}$ is the kernel of $H_0(\text{curl}, D)$ and $H_0^\perp(\text{curl}, D)$ is the “ β -orthogonal” complement in the following sense

$$(\beta \boldsymbol{\psi}^\perp, \boldsymbol{\psi}^0)_{\mathbb{L}^2} = 0 \quad \text{for all } \boldsymbol{\psi}^\perp \in H_0^\perp(\text{curl}, D) \text{ and } \boldsymbol{\psi}^0 \in H_0^0(\text{curl}, D).$$

Furthermore, it is required that the spaces $H_0^0(\text{curl}, D)$ and $H_0^\perp(\text{curl}, D)$ are closed subspaces of $H_0(\text{curl}, D)$. The formulation of the main result requires an assumption regarding the decomposition (5.51), since the case $\beta \geq 0$ is considered.

Assumption 5.7. *We assume that a splitting (5.51) with the above features can be found such that $H_0^\perp(\text{curl}, D)$ is continuously embedded in $H^1(D) \cap H_0(\text{curl}, D)$ and moreover*

$$\|\boldsymbol{\psi}^\perp\|_{\mathbb{H}^1(D)} \leq C(D) \|\text{curl } \boldsymbol{\psi}^\perp\|_{\mathbb{L}^2} \quad \text{for all } \boldsymbol{\psi}^\perp \in H_0^\perp(\text{curl}, D).$$

For further details on the construction of the decomposition we refer to [7]. With the decomposition (5.51) the total error \mathbf{e} can be decomposed into a curl-free part \mathbf{e}^0 and a “ β -weakly solenoidal” part \mathbf{e}^\perp such that

$$\mathbf{e} = \mathbf{e}^0 + \mathbf{e}^\perp \quad \text{with } \mathbf{e}^0 \in H_0^0(\text{curl}, D), \mathbf{e}^\perp \in H_0^\perp(\text{curl}, D).$$

Introducing the decomposition of \mathbf{e} into (5.49), then \mathbf{e}^0 and \mathbf{e}^\perp can be obtained as the solution of

$$\begin{aligned} (\beta \mathbf{e}^0, \boldsymbol{\psi}^0)_{\mathbb{L}^2} &= r(\boldsymbol{\psi}^0) \quad \text{for all } \boldsymbol{\psi}^0 \in H_0^0(\text{curl}, D) \\ (\chi \text{curl } \mathbf{e}^\perp, \text{curl } \boldsymbol{\psi}^\perp)_{\mathbb{L}^2} + (\beta \mathbf{e}^\perp, \boldsymbol{\psi}^\perp)_{\mathbb{L}^2} &= r(\boldsymbol{\psi}^\perp) \quad \text{for all } \boldsymbol{\psi}^\perp \in H_0^\perp(\text{curl}, D). \end{aligned}$$

The two contributions of the error are estimated separately, where for simplicity it is assumed that the coefficients β and χ are constant on each element. Considering \mathbf{e}^0 , we know that if $\boldsymbol{\psi} \in H_0^0(\text{curl}, D)$, i.e. $\text{curl } \boldsymbol{\psi} = 0$, there exist $\phi \in H_0^1(D)$ such that $\boldsymbol{\psi} = \nabla \phi$. Evaluating the residual for $H_0^0(\text{curl}, D)$ yields using Green’s formula (Corollary 5 in App. A.1) and the fact that $\text{div } \mathbf{f} = 0$

$$\begin{aligned} r(\nabla \phi) &= \sum_{K \in \mathcal{T}_h} (\mathbf{f} - \beta \tilde{\mathbf{u}}_h, \nabla \phi)_{\mathbb{L}^2(K)} \\ &= \sum_{K \in \mathcal{T}_h} (\text{div } \beta \tilde{\mathbf{u}}_h, \phi)_{L^2(K)} - \sum_{F \in \mathcal{F}} ([[\mathbf{n} \cdot \beta \tilde{\mathbf{u}}_h]], \phi)_{L^2(F)}, \end{aligned}$$

where $[[\mathbf{n} \cdot \beta \tilde{\mathbf{u}}_h]]$ denotes the jump of the normal component of $\tilde{\mathbf{u}}_h$ across the interelement face $F \in \mathcal{F}$ and \mathcal{F} the set of (inner) faces. When F is the common face of two adjacent elements $K_{\text{in}}, K_{\text{out}} \in \mathcal{T}_h$, then

$$[[\mathbf{n} \cdot \boldsymbol{\psi}]] = \mathbf{n} \cdot \boldsymbol{\psi}|_{F \subset K_{\text{out}}} - \mathbf{n} \cdot \boldsymbol{\psi}|_{F \subset K_{\text{in}}}.$$

As has been shown in [7] there result upper and lower error bounds for $\|\mathbf{e}^0\|_{\mathbb{L}^2}$ that involve the terms

$$\eta^{(0)} = \left(\sum_{K \in \mathcal{T}_h} (\eta_0^K)^2 \right)^{\frac{1}{2}} + \left(\sum_{F \in \mathcal{F}} (\eta_0^F)^2 \right)^{\frac{1}{2}}$$

with local contributions

$$\begin{aligned} \eta_0^K &= h_T \left\| \text{div } \sqrt{\beta} \tilde{\mathbf{u}}_h \right\|_{L^2(K)} \quad \text{for } K \in \mathcal{T}_h \\ \eta_0^F &= h_F^{\frac{1}{2}} \left\| \frac{1}{\sqrt{\beta_A}} [[\mathbf{n} \cdot \beta \tilde{\mathbf{u}}_h]] \right\|_{L^2(F)} \quad \text{for } F \in \mathcal{F}, \end{aligned}$$

where $\beta_A = \frac{1}{2}(\beta_{|\kappa_{\text{out}}|} + \beta_{|\kappa_{\text{in}}|})$ denotes the average of β across a face F of adjacent elements. The upper bound will also involve the iteration error $\eta_{\text{it}}^{(0)} = \|\sqrt{\beta}(\mathbf{u}_h - \tilde{\mathbf{u}}_h)\|$.

The estimation of the part \mathbf{e}^\perp of the error is based on the residual $r(\cdot)$ restricted to $H_0^\perp(\text{curl}, D)$. For $\boldsymbol{\psi} \in H_0^\perp(\text{curl}, D)$ there holds for the residual using (4.7)

$$\begin{aligned} r(\boldsymbol{\psi}^\perp) &= \sum_{K \in \mathcal{T}_h} \{(\mathbf{f} - \beta \tilde{\mathbf{u}}_h, \boldsymbol{\psi})_{\mathbb{L}^2(K)} - (\chi \text{curl } \tilde{\mathbf{u}}_h, \text{curl } \boldsymbol{\psi})_{\mathbb{L}^2(K)}\} \\ &= \sum_{K \in \mathcal{T}_h} (\mathbf{f} - \text{curl } \chi \text{curl } \tilde{\mathbf{u}}_h - \beta \tilde{\mathbf{u}}_h, \boldsymbol{\psi})_{\mathbb{L}^2(K)} - \sum_{F \in \mathcal{F}} (\llbracket \mathbf{n} \times \chi \text{curl } \tilde{\mathbf{u}}_h \rrbracket, \boldsymbol{\psi})_{\mathbb{L}^2(F)}. \end{aligned}$$

As has been shown in [7], from the representation of the residual there result upper and lower error bounds for $\|\mathbf{e}^\perp\|_E$ that involve the terms

$$\begin{aligned} \eta_1^{(1)} &= \left(\sum_{K \in \mathcal{T}_h} (\eta_{1,1}^K)^2 \right)^{\frac{1}{2}} + \left(\sum_{F \in \mathcal{F}} (\eta_1^F)^2 \right)^{\frac{1}{2}} \\ \eta_2 &= \left(\sum_{K \in \mathcal{T}_h} (\eta_{1,2}^K)^2 \right)^{\frac{1}{2}} \end{aligned}$$

with local contributions

$$\begin{aligned} \eta_{1,1}^K &= h_T \left\| \frac{1}{\sqrt{\chi}} (\pi_h \mathbf{f} - \text{curl } \chi \text{curl } \tilde{\mathbf{u}}_h - \beta \tilde{\mathbf{u}}_h) \right\|_{\mathbb{L}^2(K)} \quad \text{for } K \in \mathcal{T}_h \\ \eta_{1,2}^K &= h_T \left\| \frac{1}{\sqrt{\chi}} (\mathbf{f} - \pi_h \mathbf{f}) \right\|_{\mathbb{L}^2(K)} \quad \text{for } K \in \mathcal{T}_h \\ \eta_1^F &= h_F^{\frac{1}{2}} \left\| \frac{1}{\sqrt{\chi_A}} \llbracket \mathbf{n} \times \chi \text{curl } \tilde{\mathbf{u}}_h \rrbracket \right\|_{\mathbb{L}^2(F)} \quad \text{for } F \in \mathcal{F}. \end{aligned}$$

Here, $\pi_h \mathbf{f}$ denotes the L^2 -projection onto $\prod_{K \in \mathcal{T}_h} [P_k(K)]^3$ and χ_A is again the average of χ across the face F , $\chi_A = \frac{1}{2}(\chi_{|\kappa_{\text{out}}|} + \chi_{|\kappa_{\text{in}}|})$. As before, the iteration error has to be considered in the upper bound, $\eta_{\text{it}}^{(1)} = \|\mathbf{u}_h - \tilde{\mathbf{u}}_h\|_E$.

The main result of [7] is now the existence of an effective and reliable a posteriori error estimator for \mathbf{e} , measured in the energy norm, that is formulated as follows.

Theorem 2 ([7, Thm. 3.3.]). *Let $\eta_1 = \eta^{(0)} + \eta_1^{(1)}$, $\eta_{\text{it}} = \eta_{\text{it}}^{(0)} + \eta_{\text{it}}^{(1)}$ and the quantities $\eta^{(0)}$, $\eta_1^{(1)}$, $\eta_{\text{it}}^{(0)}$, $\eta_{\text{it}}^{(1)}$ given as above. If Assumption 5.7 holds true, then there exist constants $\gamma_1, \gamma_2, \Gamma_1, \Gamma_2$ depending only on the domain D , the uniform bounds of the coefficients χ and β and the initial triangulation \mathcal{T}_{h_0} such that*

$$\gamma_1 \eta_1 - \gamma_2 \eta_2 \leq \|\mathbf{e}\|_E \leq \Gamma_1 (\eta_1 + \eta_2) + \Gamma_2 \eta_{\text{it}}.$$

For the detailed proof, we refer to [7].

Since it is the aim to get an indicator which elements of the triangulation \mathcal{T}_h need to be refined, an estimate for the error on each element is required. It is proposed to assign half of the contributions of the faces to each of the adjacent elements. With an additional scaling, the following elementwise error estimates are proposed on each element $K \in \mathcal{T}_h$

$$\hat{\eta}_K^2 = (\eta_0^K)^2 + (\eta_{1,1}^T)^2 + \sum_{F \in \mathcal{F}_K} \frac{\beta_{|K}}{2\beta_A} (\eta_0^F)^2 + \frac{\chi_{|K}}{2\chi_A} (\eta_1^F)^2. \quad (5.52)$$

Please note that the contribution $\eta_{1,2}^T$ has been neglected, it is assumed that this contribution decays faster than the other contributions of the error estimator.

In the case of a finite element discretization by lowest order edge elements, W_h^0 , the error estimator can be simplified. The lowest order edge elements of first kind are weakly divergence free. Furthermore, the curl is approximated by piecewise constant functions such that the expression above simplifies to

$$\hat{\eta}_K^2 = h_T^2 \left\| \frac{1}{\sqrt{\chi}} (\pi_h \mathbf{f} - \beta \tilde{\mathbf{u}}_h) \right\|_{\mathbb{L}^2(K)}^2 + \sum_{F \in \mathcal{F}_K} \frac{h_F}{2} \left(\frac{\beta_{|K}}{\beta_A} \left\| \frac{1}{\sqrt{\beta_A}} [\mathbf{n} \cdot \beta \tilde{\mathbf{u}}_h] \right\|_{L^2(F)}^2 + \frac{\chi_{|K}}{\chi_A} \left\| \frac{1}{\sqrt{\chi_A}} [\mathbf{n} \times \chi \operatorname{curl} \tilde{\mathbf{u}}_h] \right\|_{\mathbb{L}^2(F)}^2 \right). \quad (5.53)$$

All contributions of the error estimator can be computed using only information of the discrete solution $\tilde{\mathbf{u}}_h$.

5.4.3. Strategies for the grid refinement

The error estimator derived in the preceding section provides an indicator for the error of the discrete solution on each element of the triangulation \mathcal{T}_k . To construct a new mesh, one has to decide, which cells should be refined and how the cells are refined. After the refinement process one has to ensure that there are no hanging nodes in the new triangulation \mathcal{T}_{k+1} , i. e. the triangulation is regular, compare (5.18).

Next, we discuss some marking strategies to select the elements that should be refined. In literature, two popular strategies are widely used. The first is a maximum criterion, the second one is an equilibration strategy. The latter one is often referred to as Dörfler criterion, [21, 83]. Let \mathcal{T}_k be a triangulation of the computational domain and denote η_K the local error estimate on each element $K \in \mathcal{T}_k$. Then, these two strategies can be described as follows.

Maximum strategy: Refine all elements $K \in \mathcal{T}_k$ for which

$$\eta_K \geq \theta \max_{\tilde{K} \in \mathcal{T}_k} \eta_{\tilde{K}}, \quad (5.54)$$

where $\theta \in (0, 1)$ is some threshold that controls how many elements are refined.

Equilibration strategy: Find the minimal set $\tilde{\mathcal{T}} \subset \mathcal{T}_k$ such that

$$\sum_{K \in \tilde{\mathcal{T}}} \eta_K^2 \geq \theta \sum_{K \in \mathcal{T}_k} \eta_K^2.$$

The maximum strategy is cheaper to evaluate than the equilibration strategy. With the help of the parameter θ it is possible to adjust how many elements will be refined. For the maximum strategy, a small value of θ will lead to a large number of elements to be refined. For the equilibration strategy, the effect is reversed. A value close to one will lead to a large set $\tilde{\mathcal{T}}$ such that nearly all elements will be refined. Usually in applications, a value of $\theta = 0.5$ is proposed for both strategies. In the case of the equilibration strategy, the convergence of adaptive methods has been proved, [21].

After marking the elements for refinement, we have to discuss how the elements are refined and the new grid is created. This is done in two stages. In the first stage, the elements that are marked for refinement due to a large value of the error indicator are refined. This refinement is usually called regular. In a second step, additional elements have to be refined in order to avoid hanging nodes and to guarantee that the new triangulation is regular.

In the case of 2D meshes consisting of triangles, a regular refinement can be performed by connecting the midpoints of the edges. This refinement is often denoted as red. In order to avoid hanging nodes, additional triangles have to be refined, where new nodes were introduced due to a red refinement of adjacent elements. Depending on the number of new nodes, these refinements are denoted as green or blue, we refer to the literature for details, e. g. [83]. In the case of tetrahedrons, a regular refinement can be obtained by connecting the midpoints of the edges. There result four new tetrahedrons. The remaining octahedron can be divided into four tetrahedrons by cutting along two orthogonal diagonals. Finally, there result eight new tetrahedrons of equal volume, but they are in general not similar to the parent tetrahedron. Therefore, one can not guarantee that the shape parameter of the mesh does not deteriorate during repeated refinement. Additional techniques can preserve the shape parameter, see e. g. [9]. In order to avoid hanging nodes, further tetrahedrons have to be refined. As in the case of triangles there arise different irregular refinement patterns. For details we refer to the literature.

An alternative method of grid refinement are bisection algorithms. There, triangles and also tetrahedrons are bisected by joining the midpoint of the longest edge with the opposite node(s). Details can be found in the literature.

In the present work, we use the grid generator **TetGen** for the creation of the new grid. **TetGen** is a robust, fast, and easy-to-use software for generating tetrahedral meshes. For a 3D polyhedral domain, **TetGen** generates the constrained Delaunay tetrahedralization and an isotropic adaptive tetrahedral mesh of it. Domain boundaries (edges and faces) are respected and can be preserved in the resulting mesh, [76].

The elements that need to be refined are marked according to the maximum strategy (5.54). For the refinement process it is assumed that an initial grid \mathcal{T}_k is given. For

the creation of an initial grid with **TetGen**, it is possible to provide volume constraints for different regions of the geometry. For the refinement process, we can make use of this functionality. It is possible to prescribe volume constraints for each grid cell of the mesh \mathcal{T}_k . Using e. g.

$$\tilde{V}_K = \frac{1}{8}V_K \quad \text{for } K \in \tilde{\mathcal{T}},$$

where $\tilde{\mathcal{T}} \subset \mathcal{T}_k$ denotes the elements marked for refinement, V_K the volume of the element K and \tilde{V}_K the volume constraint for the cell K in the new grid \mathcal{T}_{k+1} , corresponds to a regular refinement of the marked tetrahedrons.

TetGen automatically creates a new grid \mathcal{T}_{k+1} by refining the old grid \mathcal{T}_k , taking the prescribed volume constraints \tilde{V}_K for each element $K \in \mathcal{T}_k$ into account. The resulting mesh is regular, i. e. there are no hanging nodes, and the Delaunay property of the mesh is satisfied. In order to preserve the Delaunay property, it might be possible that additional nodes are created or the mesh is smoothed. As a drawback of the smoothing one can not guarantee that the created meshes are hierarchic.

Since **TetGen** expects a volume constraint for the refinement process, we are not restricted to regular refinements where e. g. the new volume is $1/8$ of the old volume. It is also possible to construct the volume constraint for the new mesh in dependence on the estimated error on each cell. A large estimated error would lead to more refinements of the parent cell, while a small error might only require a bisection of the element. We propose the following strategy to prescribe the volume constraint for the mesh cell $K \in \mathcal{T}_k$

$$\tilde{V}_K = \max \left\{ \eta_0 \frac{\epsilon}{\eta_K}, \delta_0 \right\} V_K, \quad (5.55)$$

where ϵ denotes the desired tolerance, δ_0 some constant to bound the maximum reduction of the new volume and $\eta_0 < 1$ some constant to enforce a grid refinement if the ratio $\epsilon/\eta_K \approx 1$. In this way, the reduction in the error might be accelerated and the number of iterations to obtain a prescribed accuracy might be reduced. A numerical example, where a refinement using the maximum strategy is compared to the proposed strategy (5.55), is presented in Section 6.1.

We use the strategy (5.55) together with the a posteriori error estimator introduced in Section 5.4.2 to create the adaptive grid for the simulation of the induction heating problem.

5.5. Averaging of the magnetic permeability

In ferromagnetic materials, the magnetic permeability is a nonlinear function. It depends on the temperature θ and the magnetic field \mathbf{H} , cf. Section 3.4, i. e.

$$\mu = \mu(|\mathbf{H}|, \theta).$$

As a consequence, the vector potential equation is nonlinear and suitable solvers are required. Using e. g. Newton's method is computational costly. In Section 5.3 the method of freezing coefficients is introduced. As a drawback, it might require quite

small time steps to resolve the nonlinearity and to obtain an accurate solution for \mathbf{A}_h . Furthermore, the curl-curl matrix \mathbf{K}_μ has to be assembled in every time step of the Maxwell iteration. As a consequence, in every time step, the system matrices of the time stepping scheme have to be updated and the matrix factorizations have to be recomputed, which is the most time consuming step.

Therefore, we introduce a method to linearize the vector potential equation. This is done by an averaging procedure proposed in [18]. In induction heating problems, the focus lies on the efficient computation of the Joule heat. The exact reproduction of the magnetic field is of minor importance as long as the Joule heat term $\mathbf{J} \cdot \mathbf{E} = \sigma |\partial_t \mathbf{A}|^2$ is approximated with sufficient accuracy. Since only an averaged value of the Joule heat enters the heat equation, it is assumed that it is sufficient to consider also a time averaged value of the permeability. In the following, we explain the algorithm to compute the averaged permeability $\bar{\mu}$.

After decoupling the heat- and the vector potential equation as described in Section 5.3 we consider the time interval (t^k, t^{k+1}) and assume that the temperature is given at time t^k . Furthermore, it is assumed that the vector potential equation has been solved and a periodic solution for \mathbf{A} is known on (t^k, t^{k+1}) . It is assumed that this solution has been obtained using a known averaged permeability $\bar{\mu}(x)$. Then, the periodic magnetic field is given by $\mathbf{H} = \bar{\mu}^{-1} \text{curl } \mathbf{A}$. The exact magnetic permeability is then a periodic function obtained from the nonlinear magnetization curve

$$\tilde{\mu}(x, t) = \mu(|\mathbf{H}(x, t)|, \theta^k(x)). \quad (5.56)$$

Now, the new iterate of the averaged magnetic permeability $\bar{\mu}(x)$ is obtained by computing the mean value of $\tilde{\mu}(x, t)$ over one period in the following way

$$\frac{1}{\bar{\mu}(x)} = \frac{\omega}{2\pi} \int_0^{\frac{2\pi}{\omega}} \frac{1}{\tilde{\mu}(x, t)} dt. \quad (5.57)$$

Using the inverse of μ for the averaging procedure is proposed in [18]. The authors investigate different averaging techniques and consider an averaging of μ^2 , μ , μ^{-1} and μ^{-2} . By numerical tests, the harmonic mean given in (5.57) performed best.

The permeability $\bar{\mu}(x)$ is independent of \mathbf{A} , it only depends on the space coordinate x and has to be computed in every point of the domain. It was assumed that a solution of \mathbf{A} is known on the actual time interval (t^k, t^{k+1}) . Of course, \mathbf{A} is only available for previous time steps such that the averaged permeability $\bar{\mu}$ has to be computed by a fixed point iteration, starting e. g. with $\bar{\mu} = \mu_0$. Numerical tests have shown that the averaging of the permeability converges typically within two to three iterations.

It is the advantage of the averaged permeability that $\bar{\mu}$ is constant on the interval (t^k, t^{k+1}) . The vector potential equation is linear and we can keep the matrix \mathbf{K}_μ for the whole interval (t^k, t^{k+1}) , there is no need to reassemble and, more important, to recompute the matrix factorization. In this case, the time iteration of the vector potential equation can be computed effectively using e. g. the PCG method in combination with PARDISO, cf. Section 5.3.6.

Compared to the literature, a linearization of μ is a common approach. A similar approach as described above is used in [48]. The technique is also used in actual publications related to induction hardening, [36, 72]. A fictive linear material with a fictive permeability μ_f is introduced. By an iterative procedure, the fictive permeability is computed by energetic considerations. This approach can be easily implemented when considering Maxwell's equations in the frequency domain, since it only involves the magnetic energy $\mathbf{H} \cdot \mathbf{B}$. Ostrowski [60] introduces an effective permeability μ_{eff} by averaging the nonlinear permeability over one period similar as described above.

5.6. The complete algorithm to solve the induction hardening problem

The solution of the system of partial and ordinary differential equations (5.9) is obtained using the software package `pdelib`, which is developed and maintained at WIAS Berlin. The `pdelib` is a modular software package based on C/C++ to solve partial differential equations by the finite element or finite volume method [61].

In `pdelib`, hierarchical finite elements for H^1 are available. In order to solve the vector potential equation, edge based elements of Nédélec type as described in Section 5.2.4 are used. These were implemented in `pdelib`. The complete algorithm to simulate the inductive heating for gears consisting of the methods described in Sections 5.1 to 5.5 is summarized in the following.

1. Initialization.

The first step consists in the definition of the scenario, i. e. the definition of the heating time T , the specification of the MF and HF frequencies f_{mf} and f_{hf} and the relative power p_{mf} and p_{hf} corresponding MF and HF, cf. equation (3.25). Furthermore, one has to define an error tolerance ϵ for the error estimator to create an adaptive grid. Then, the geometry description is read from a file and a coarse initial grid is created using `TetGen`.

2. Adaptive grid generation.

Setting the initial magnetic permeability to $\mu = \mu_0$ the vector potential equation is solved for some time steps (one fourth of a period) using edge based finite elements for the discretization in space and a Crank-Nicolson scheme in time on the coarse grid. The error estimator $\hat{\eta}$, equation (5.53), is evaluated on each element and for each time step. The estimated local errors are summed up for the time steps to get an indicator, which mesh cells need to be refined. A refined grid is created using `TetGen` together with (5.55) until $\max_{K \in \mathcal{T}} \hat{\eta} \leq \epsilon$.

3. Time iteration of the magnetic vector potential.

We set the time step count to $k = 0$ and $t^k = 0$. Since in the case of multifrequency induction hardening the high frequency might be by a factor of 20 higher than the medium frequency (typically $f_{\text{mf}} = 10$ kHz and $f_{\text{hf}} = 200$ kHz), it is recommended to split the magnetic vector potential \mathbf{A} into a MF and HF part

$$\mathbf{A} = \mathbf{A}_{\text{mf}} + \mathbf{A}_{\text{hf}}.$$

With the use of the averaged magnetic permeability, cf. Section 5.5, the vector potential equation is linear such that \mathbf{A}_{mf} and \mathbf{A}_{hf} are the solutions of

$$\begin{aligned}\sigma \partial_t \mathbf{A}_{\text{mf}} + \text{curl} \bar{\mu}^{-1} \text{curl} \mathbf{A}_{\text{mf}} &= \mathbf{J}_{\text{src,mf}} \quad \text{and} \\ \sigma \partial_t \mathbf{A}_{\text{hf}} + \text{curl} \bar{\mu}^{-1} \text{curl} \mathbf{A}_{\text{hf}} &= \mathbf{J}_{\text{src,hf}}\end{aligned}$$

where $\mathbf{J}_{\text{src}} = \mathbf{J}_{\text{src,mf}} + \mathbf{J}_{\text{src,hf}}$ and

$$\mathbf{J}_{\text{src,mf}} = I_{\text{mf}} p_{\text{mf}}(t) \cos(2\pi f_{\text{mf}} t) \mathbf{J}_0(x) \quad \text{and} \quad \mathbf{J}_{\text{src,hf}} = I_{\text{hf}} p_{\text{hf}}(t) \cos(2\pi f_{\text{hf}} t) \mathbf{J}_0(x).$$

We solve the equations above separately using a BDF-2 discretization in time, see Section 5.3.1, in combination with the PCG method and PARDISO as preconditioner, Section 5.3.2, until we obtain a periodic solution for \mathbf{A}_{mf} and \mathbf{A}_{hf} .

(a) *Computation of the averaged magnetic permeability.*

The update of the averaged magnetic permeability requires knowledge of the complete vector potential field $\mathbf{A} = \mathbf{A}_{\text{mf}} + \mathbf{A}_{\text{hf}}$. The vector potential \mathbf{A} is determined from the periodic solutions for \mathbf{A}_{mf} and \mathbf{A}_{hf} by interpolation. Then, the averaging of μ is done according to Section 5.5. We iterate the computation of \mathbf{A}_{mf} , \mathbf{A}_{hf} and $\bar{\mu}$ until there is no significant change in $\bar{\mu}$.

(b) *Computation of the averaged Joule heat.*

Since the functions $\sin(2\pi kt)$ and $\cos(2\pi kt)$, $k \in \mathbb{N}$, are orthogonal, there holds for the averaged Joule heat

$$|\partial_t \mathbf{A}|^2 = |\partial_t \mathbf{A}_{\text{mf}}|^2 + |\partial_t \mathbf{A}_{\text{hf}}|^2,$$

provided that the high frequency is an integer multiple of the medium frequency: $\omega_{\text{hf}} = n \omega_{\text{mf}}$ with $n \in \mathbb{N}$. As a consequence, the averaging of the Joule heat can be done separately for the medium and high frequency parts as described in Section 5.3.4. The overall Joule heat entering the right hand side is obtained by summing up both contributions.

4. *Time iteration of the heat equation.*

With the heat source given by the averaged Joule heat, the next step is the computation of the temperature and the volume fraction of austenite for the new time step t^{k+1} by solving equations (5.42) and (5.41) as described in Section 5.3.4.

5. Finally, set $k = k + 1$ and iterate steps 3. and 4. until $t^k \geq T$.

Chapter 6.

Simulation

Introduction

In this chapter, numerical simulations of the inductive heating of discs and gears are presented and compared to experimental results. Before the simulation of the inductive heating is considered, an academic test example is used to verify the implementation of the finite element discretization with curl-conforming edge elements and to test the adaptive grid refinement.

6.1. Test of the adaptive grid refinement

To test the implementation of the edge elements and the adaptive refinement algorithm we consider the following model problem on an L-shape domain, where the exact solution is known. Find $\mathbf{u} \in H(\text{curl}, L)$ such that

$$\begin{aligned} \text{curl curl } \mathbf{u} + \mathbf{u} &= \mathbf{f} & \text{in } L := (-1, 1)^3 \setminus [0, 1]^2 \times [-1, 1] \\ \text{curl } \mathbf{u} \times \mathbf{n} &= 0 & \text{on } \partial L \end{aligned} \tag{6.1}$$

in a weak sense, where $\mathbf{f} = \nabla(r^{2/3} \sin(2/3\varphi))$ in cylindrical coordinates. The exact solution is irrotational and divergence free. It is given by $\mathbf{u} = \mathbf{f}$ and does not belong to $H^1(L)$, the solution exhibits a singularity, [7]. We test the adaptive algorithm introduced in Section 5.4 for this test problem. It is expected that a graduated numerical grid results from the adaptive refinement. The initial and the final grid as well as the numerical solution $\mathbf{u} = (u_x, u_y, u_z)^T$, where $u_z = 0$, are depicted in Figure 6.1. In Figure 6.2 the total error in dependence on the number of degrees of freedom is depicted for different refinement strategies and a uniform refinement. For the solution of equation (6.1) the maximum criterion (5.54) with $\eta = 0.5$ is used to select the elements for refinement. The tetrahedrons are then refined by a regular refinement or a bisection algorithm. As a third strategy, we consider the error related refinement strategy (5.55). The grid generator PARDISO is used for refinement. It expects a volume constraint to create an adaptive grid. Therefore, the volume restriction for each element is defined in relation to the estimated error on each element as explained in Section 5.4.3, compare to (5.55). We stop the adaptive algorithm, if the estimated error is below a given threshold. As depicted in Figure 6.2, the total error for the final iterate for the adaptive refinement strategies is nearly the same. The different methods deviate essentially in the number of iterations that are necessary to reach

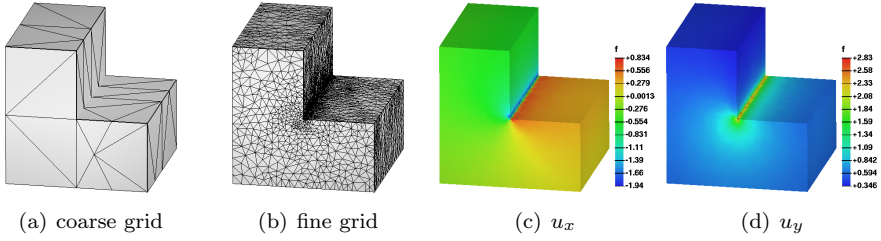


Figure 6.1.: Coarsest and finest grid and numerical solution $\mathbf{u} = (u_x, u_y, u_z)$ for problem (6.1)

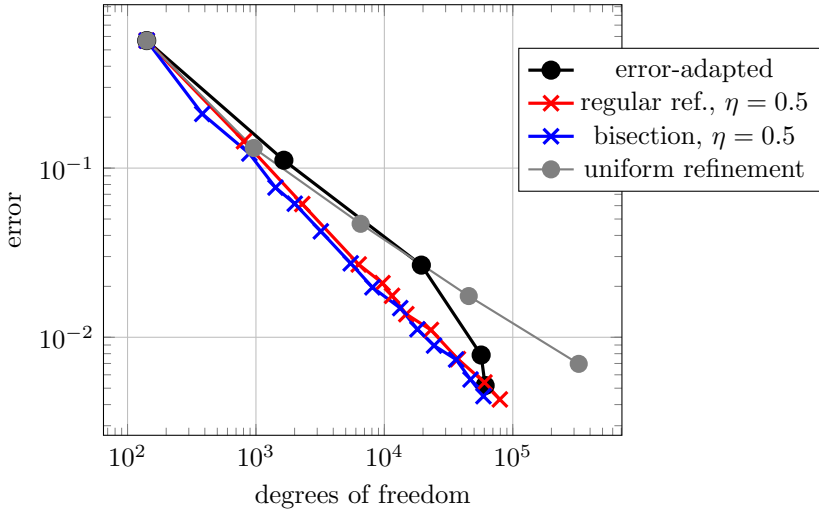


Figure 6.2.: Comparison of different adaptive grid generation strategies

the prescribed error tolerance. While the adaptive methods using the maximum criterion require 11 (regular refinement) or 14 (bisection) iterations, the proposed error related strategy reaches the prescribed error tolerance after 5 cycles and the number of degrees of freedom for the final iterate is nearly the same as for the other strategies. Due to the design of the error based refinement strategy the relation between degrees of freedom and total error is not optimal for the intermediate iterates. For these it is comparable to a uniform refinement and the other strategies show better performance. Nevertheless, we prefer the error related refinement strategy since the solution of the vector potential equation is the most time consuming step during the adaptive grid generation process.

6.2. Numerical simulations for discs

6.2.1. Numerical simulations

As the next step, we consider numerical simulations of induction heating for discs and perform an experimental verification. In order to account for the different coupling distances that occur in the case of gears, discs with three different radii are considered, which correspond to the addendum circle (47.7 mm), the pitch circle (42 mm) and the root circle (38.7 mm) of the reference gear used in Section 6.3. This results in different coupling distances. The width of the discs is taken as 8 mm.

The parameters for the simulation are shown in Table 6.1, which result in nine different cases. To allow for an experimental verification, the parameters are matched to experiments carried out by IWT Bremen. This is necessary, since e. g. the frequency can not be adjusted freely. The multifrequency converter operates at the resonant frequency of the oscillating circuit, consisting of the inductor coil, the converter, connection cables and the necessary filters and adaptation capacitors to compensate the reactive power. The experimental setup is described in detail in Section 6.2.2.

Parameter	Variants		
Diameter	47.7 mm (addendum circle)	42 mm (pitch circle)	38.7 mm (root circle)
Coupling distance	1.15 mm	4 mm	5.65 mm
Induction heating	HF	MF	(MF+HF)
Frequency	200 kHz	12 kHz	12 kHz + 200 kHz
Power in %	50 %	63 %	46 % (MF) + 35 % (HF)

Table 6.1.: Parameter variants for the experimental verification of discs

For the numerical simulations of the disc specimen it is possible to reduce the geometric complexity by exploiting the symmetry of the workpiece. It is not necessary to simulate the complete disc. The cross section of a horizontal cut serves as a symmetry plane. In addition, due to angular symmetry, it is possible to consider only a

segment of the disc ¹. The disc geometry is depicted in Figure 6.3. The reduced computational domain is indicated in red, where for the sake of presentation the domain corresponding to the surrounding air is blanked out.

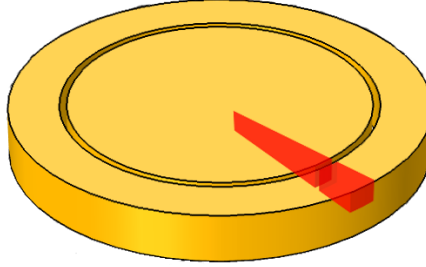


Figure 6.3.: Computational domain using symmetry conditions (exemplary for the disc)

It is necessary to define boundary conditions on the cutting planes for the reduced geometry. For this, we denote the horizontal cross section by Γ_H . The vertical cuts are denoted by Γ_V . Since the source current \mathbf{J}_{src} is defined only in angular direction, the radial and the z -component of the magnetic vector potential \mathbf{A} are zero on the vertical cutting planes. Therefore, the tangential components of \mathbf{A} vanish on Γ_V , $\mathbf{A} \times \mathbf{n} = 0$.

The magnetic induction \mathbf{B} is perpendicular to \mathbf{A} . As a consequence, the magnetic field \mathbf{H} has only non-vanishing normal components on the horizontal cutting plane Γ_H . All together there holds

$$\mathbf{A} \times \mathbf{n} = 0 \quad \text{on} \quad \Gamma_V \quad \text{and} \quad \mu^{-1} \text{curl} \mathbf{A} \times \mathbf{n} = 0 \quad \text{on} \quad \Gamma_H.$$

These boundary conditions arising from symmetry conditions correspond to the conditions (PEC) and (PMC) introduced in (3.12).

For the reduced disc geometry, simulations of the heating procedure are carried out. The heating time is set to 1.0 s. Since in the experiments a temperature measurement by pyrometer is not possible during the heating process but only immediately after switching off the current, the effect of self-cooling with the source term set to zero, i. e. $\mathbf{J}_{\text{src}} = 0$, is taken into account and the simulation time is extended up to 1.2 s.

In the following we present detailed simulation results for the disc with diameter $d = 47.7$ mm. The obtained results are discussed in Section 6.2.3. The grids that are used for the finite element simulations for the case of medium, high and multi-frequency are depicted in Figure 6.4. The grids are generated adaptively by the algorithm described in Section 5.4. The grid is adapted to the frequency dependent penetration depth of

¹Due to angular symmetry it is possible to consider the setting in 2D. We are interested in the performance and the calibration of our 3D algorithm and consider a 3D geometry. The angle has been chosen as half the size of a tooth as for the gear experiments.

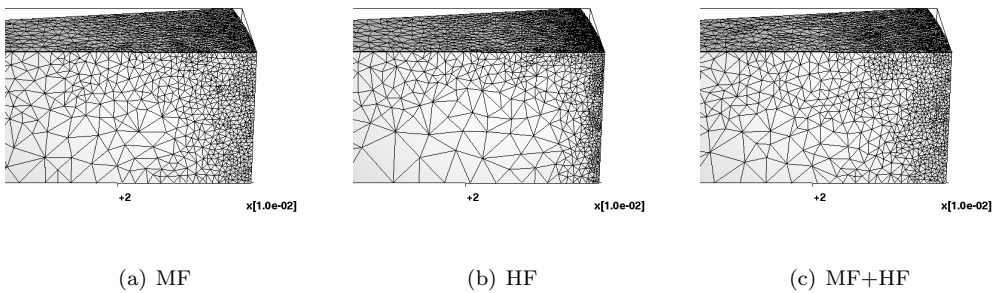


Figure 6.4.: Comparison of the adaptively generated grids

the eddy currents. In the case of high frequency, the grid is very fine in a small surface layer of the workpiece, while in the case of medium frequency the elements are refined also within the workpiece. In the case of multifrequency, the MF part dominates such that the grid is quite similar to the medium frequency case, cf. Fig. 6.4.

Disc with diameter 47.7 mm, MF

The simulation results for the disc heated with medium frequency are depicted in Figure 6.5. The temperature profile and the corresponding phase fraction of austenite are depicted for different time snapshots. The maximum temperature is reached after 1.0s, Fig. 6.5 (c). Since the experimental measurement of the temperature by a pyrometer is only possible with a delay, the simulation is continued. The temperature reduces due to heat diffusion. The final temperature after 1.2s and the corresponding austenitic fraction are depicted in Fig. 6.5 (d).

Disc with diameter 47.7 mm, HF

In Figure 6.6, the results using high frequency power are shown. As above, the temperature profile and the austenite fraction for different time snapshots are presented. Compared to the case of medium frequency, the profile of the austenite is concave while in the case of MF it is convex. This is due to the fact that the highest temperature is attained at the upper corner of the disc, Fig. 6.6 (b).

Disc with diameter 47.7 mm, MF+HF

Finally, the temperature profiles and the corresponding austenite fraction for the case of simultaneous applied medium and high frequency power is shown in Figure 6.7. The most significant difference to the single frequency case is the nearly homogeneous austenitic profile, while in the case of MF, the profile is convex and in the case of HF a concave profile results.

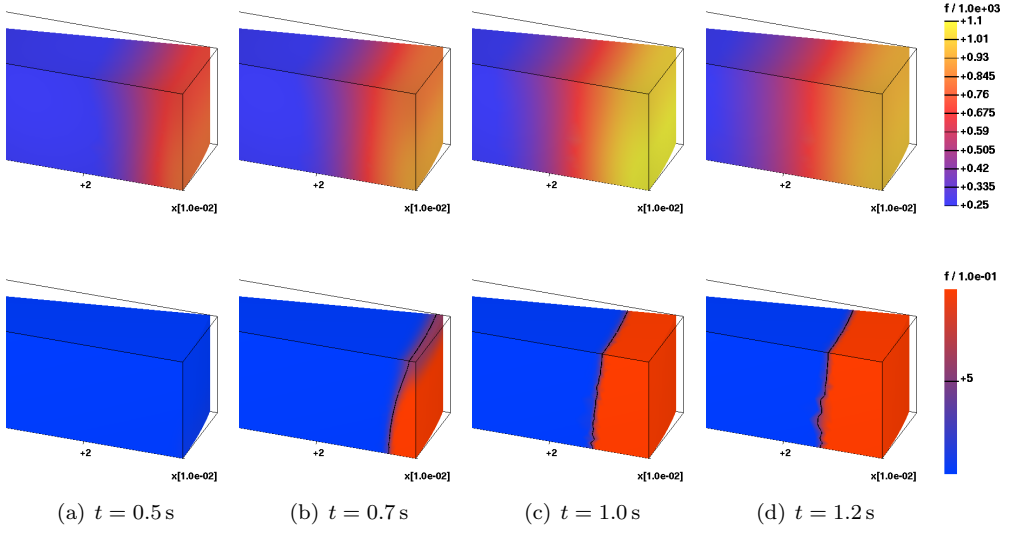


Figure 6.5.: Temperature θ and phase fraction of austenite z for the disc with diameter $d = 47.7$ mm, MF: $f = 12$ kHz

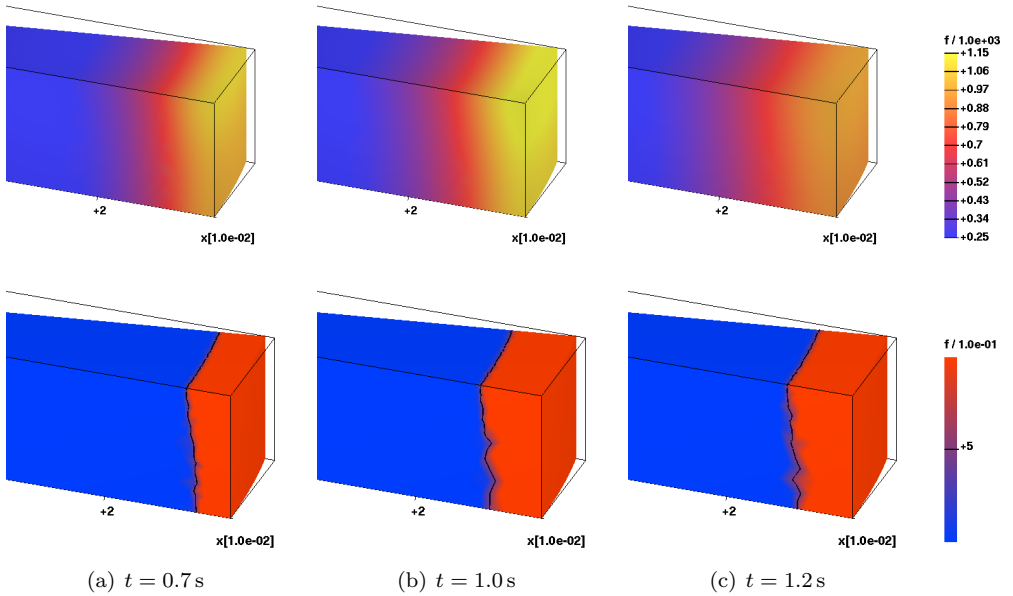


Figure 6.6.: Temperature θ and phase fraction of austenite z for the disc with diameter $d = 47.7$ mm, HF: $f = 204$ kHz

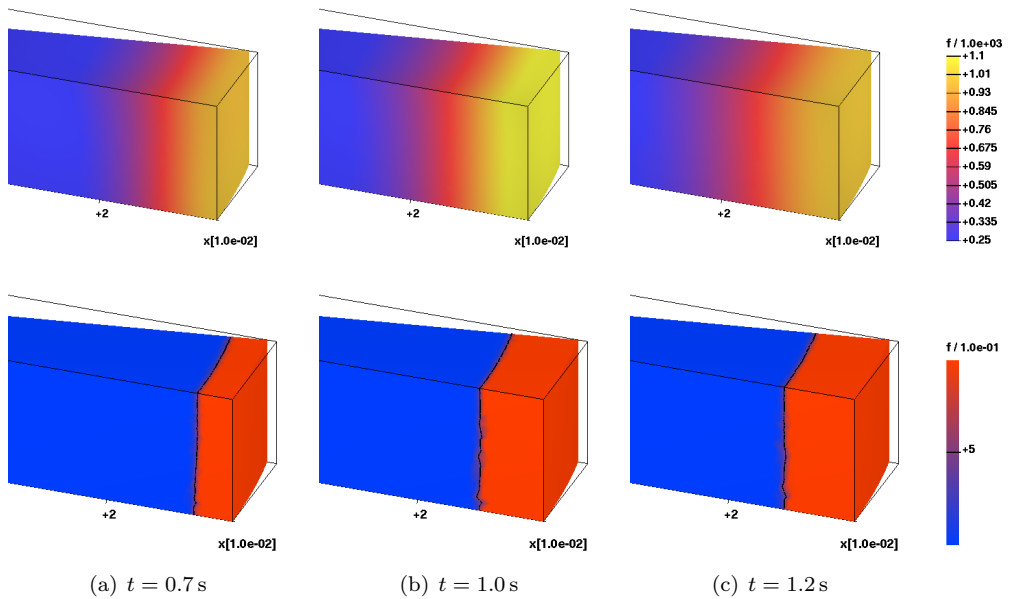


Figure 6.7.: Temperature θ and phase fraction of austenite z for the disc with diameter $d = 47.7$ mm, MF+HF: $f = 12$ kHz + 204 kHz.

The simulation results for all of the three disc diameters, 38.7 mm, 42.0 mm and 47.7 mm are summarized in Table 6.2. In subsequent sections, an experimental verification of the numerical results is established.

No.	Diameter [mm]	Power [%]		Frequency [kHz]		Inductor current [A]		Temperature [°C]		Aust. [mm]	
		MF	HF	MF	HF	MF	HF	max	at 1.2 s	cross section	upper surface
1.	38.7	63	0	11		5292		635	524		
2.	38.7	0	50		198		1600	928	668		1.01
3.	38.7	46	35	11	198	3864	1120	779	593		
4.	42	63	0	11		5292		791	676		
5.	42	0	50		198		1600	956	717	0.54	1.2
6.	42	46	35	11	198	3864	1120	845	699	0.34	0.63
7.	47.7	63	0	12		5040		1137	1000	2.43	2.1
8.	47.7	0	50		204		1700	1221	925	1.69	1.99
9.	47.7	46	35	12	204	3680	1190	1176	1005	2.17	2.16

Table 6.2.: Summary of the simulation results

6.2.2. Experimental setup

The experimental studies presented in this section and in Section 6.3.2 were conducted by IWT Bremen. For the experiments, a 200 kW medium frequency plus 100 kW high frequency induction hardening machine (from EFD Induction GmbH) with Multi-Frequency Concept (MFC) for contour hardening was used for the induction hardening of disc samples and for gears made of the steel 42CrMo4. The samples were heated by a ring inductor made of copper with a diameter of 50 mm and subsequently quenched by a shower of a polymer-water mixture. During the heating and the quenching, the workpiece rotates in order to avoid any effects from the connection of the inductor to the generator. The samples for metallographic analyses were taken with a water cooled abrasive cut-off machine and then prepared metallographically. Finally they were etched with nital and the hardness pattern was analysed with a microscope.

The temperature during the induction hardening process was measured by a pyrometer and by thermo couples. Usually the coupling distance between the workpiece and the inductor is about 1 mm. Therefore, the typically used pyrometer can not determine the surface temperature during the heating. Only during the transfer of the workpiece to the quenching equipment, the surface is in ‘plain view’ and the temperature can be measured by the pyrometer. The retardation time between the temperature measurement and the end of the heating was estimated as 0.2 s. In addition, there is an error in the temperature measurement due to variations of the emission degree of the metal surface. Despite calibration, this error is estimated as ± 10 K. Regarding the temperature measurement by thermo couples, the temperature sensors were placed 1 mm beyond the surface of the specimen. During the experiments it turned out that the thermo couples show a retardation time. Figure 6.8 shows exemplary a temperature measurement by thermocouples for the gear together with a numerical simulated temperature evolution. For the disc specimen, the same effect is observed. The measured

temperature curve is shifted by some tenth of a second compared to the simulation. Especially the fact, that the temperature still rises significantly after the heating power is turned off can not be explained by heat conduction effects alone. This is an indication that the delay results from a thermal inertia of the thermo couple. The effect is stronger in the tip of the tooth, where higher heating rates are achieved. Since there is this delay, we do not use the thermo couple measurements for verification purpose.

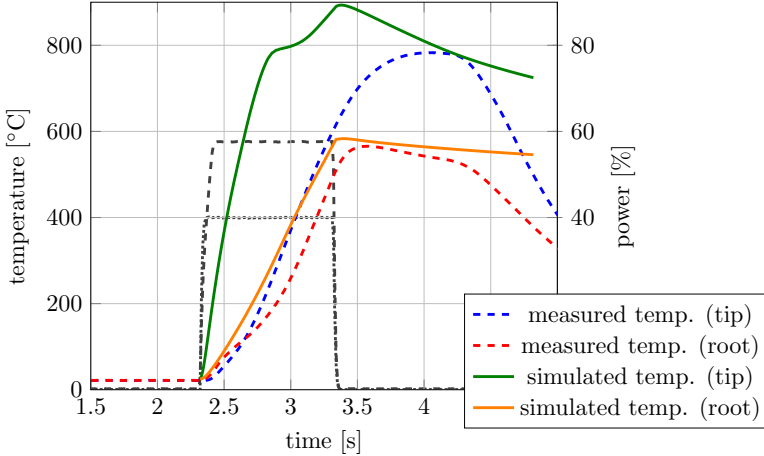


Figure 6.8.: Exemplary evolution of the simulated and the measured temperature by thermo-elements positioned 1 mm below surface; the grey curves indicate the MF and HF power

In addition to the temperature, measurements of the hardness in the surface area were performed. From these values, the hardening depth can be estimated as the distance, where the hardness drops below some threshold. It is directly related to the amount of martensite that has been formed during the hardening process.

In the simulation of the inductive heating, the austenite fraction z is computed. In order to compare simulation and experiment, we have to relate this information to the measured hardness or the martensitic profile. Since the subsequent quenching procedure is not considered in this work, it is assumed that during the quenching, the austenite transforms completely into martensite. This fact is confirmed by experimental observations. The hardening depth obtained from the experiment is then compared to the penetration depth of the austenite phase z .

For the numerical simulation it is necessary to define the source current density \mathbf{J}_{src} in the inductor. Therefore, knowledge of the inductor current is necessary to compare simulation and experiment. A direct measurement of the current in the induction coil is not possible. Typically in technical applications, the induction heating process is power controlled. The power of the medium and high frequency is given as relative value in percent, related to the maximum possible value of the hardening machine for a given frequency. Nevertheless, the current is the crucial quantity for the generation of

the electromagnetic fields. By an online monitoring system at the induction hardening machine, the absolute power and the current in the generator can be determined. As it turned out, the measured inverter current and not the absolute power value is linearly related to the relative power, which serves as the control parameter at the machine. Therefore, the current is used as input parameter for the simulations instead of the voltage or the power. From the specifications of the hardening machine, the transmission ratio between inverter and inductor is known, for medium frequency it is approximately 9:1 while for high frequency it is 10:1. With the knowledge of the transmission ratio and the inverter current that corresponds to a machine specific parameter of 100 %, it is possible to set the experimental input datum in relation to the numerical input datum and a comparison of the simulation and the experiment is possible.

For the numerical algorithm it is necessary that the ratio between the medium and high frequency is an integer number. Therefore, we can not use exactly the same values for the frequency as in the experiments. The frequency used in the simulation is adapted to the nearest possible value to achieve an integer ratio.

6.2.3. Experimental verification and discussion

The numerical results are compared to the experiments described above. In order to account for the delay of 0.2s for the temperature measurement by pyrometer, the effect of self-cooling with the heating switched off is simulated. The temperature at $t = 1.2$ s is then compared to the experimental measurement.

In Figure 6.9, the measured and the simulated temperature is depicted for the three different disc geometries for medium-, high- and multifrequency induction heating, respectively. Comparing the experimental results to the simulation one can see that the temperature obtained after 1.2s is in good correspondence for all disc diameters. The differences are slightly bigger than the measurement error of ± 10 K. Keeping in mind that there is the delay in the temperature measurement, in general, the temperature is reproduced quite well.

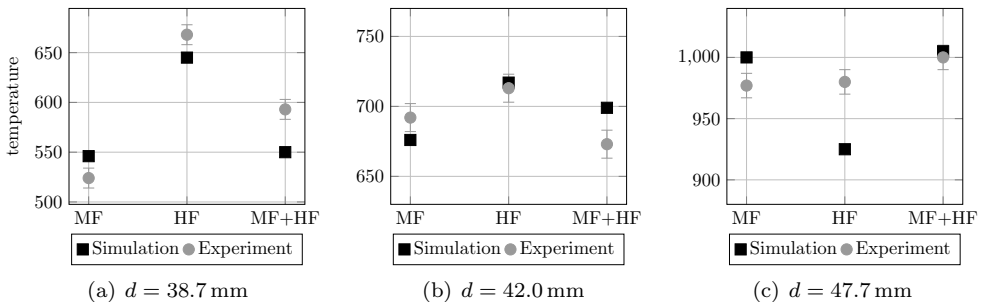


Figure 6.9.: Comparison between the measured and simulated temperature for the different disc specimen

One has to mention that the focus was not to fit the simulated temperature to the experimental result. It was the aim to use an input datum that can be directly related to machine parameters. With the knowledge of the transformation ratio between the inverter and the inductor we obtain an estimate of the inductor current, which is used as a source term in the simulation, compare Section 3.1.4.

The obtained hardening depths for the experiment and the simulation are opposed in Table 6.3. In the case of the largest coupling distance, the maximum temperatures lie below the austenitization temperature such that no phase transition occurred.

No.	Frequency	Diameter [mm]	Aust. [mm] cross section	Exp. hardening depth [mm]		
				norm.	Q&T low t.	Q&T high t.
1.	MF	38.7				
2.	HF	38.7		0.16		0.49
3.	MF+HF	38.7				
4.	MF	42		0.59	0.59	1.06
5.	HF	42	0.54	0.64	0.6	0.87
6.	MF+HF	42	0.34	0.27	0.16	0.69
7.	MF	47.7	2.43	2.61	2.6	2.78
8.	HF	47.7	1.69	1.95	1.94	2.16
9.	MF+HF	47.7	2.17	2.35	2.11	2.56

Table 6.3.: Comparison between simulated and experimental hardening depth

For the heating of the disc with diameter $d = 42$ mm a phase transition occurs. In the case of using pure HF and simultaneously applied MF+HF, No. 5 and 6, the simulated hardening depths lie in the range of the experimentally observed ones. In the case of heating with pure MF, No. 4, the austenitization temperature is not reached in the simulation while in the experiment, a phase transition occurs and a hardening depth of 0.59 mm is obtained. Opposed to that, the simulated temperature after 1.2 s lies in a comparable range and is only 20 K below the experimental result.

In general, the experimental results could be reproduced quite well. Especially for the largest disc with $d = 47.7$ mm, which corresponds to a realistic coupling distance in induction heating of cylindrical shaped workpieces such as shafts, there is a good correspondence between experimental and computational result. This holds true for the temperature as well as the hardening depth.

A further indication of the good correspondence between experiment and simulation represents the lateral profile of the austenitic phase fraction. In Figure 6.10 the computed profile is compared to micrographs of a lateral cut through the disc with diameter $d = 47.7$ mm for pure MF, HF and the case of multifrequency. In the case of medium frequency, a convex profile results, where the penetration depth is higher in the centre of the disc. For HF the profile is concave, while in the case of the simultaneous applied medium and high frequency a nearly homogeneous profile could be observed. In the experiments, three different initial states for the microstructure were considered, which are a normalized state and two different states quenched and tempered (Q&T). The dependence on the initial microstructure can not be resolved directly by the numerical simulation. The austenitization behaviour is recaptured by the evolution equation for the phase fraction of austenite z in terms of equation (3.26).

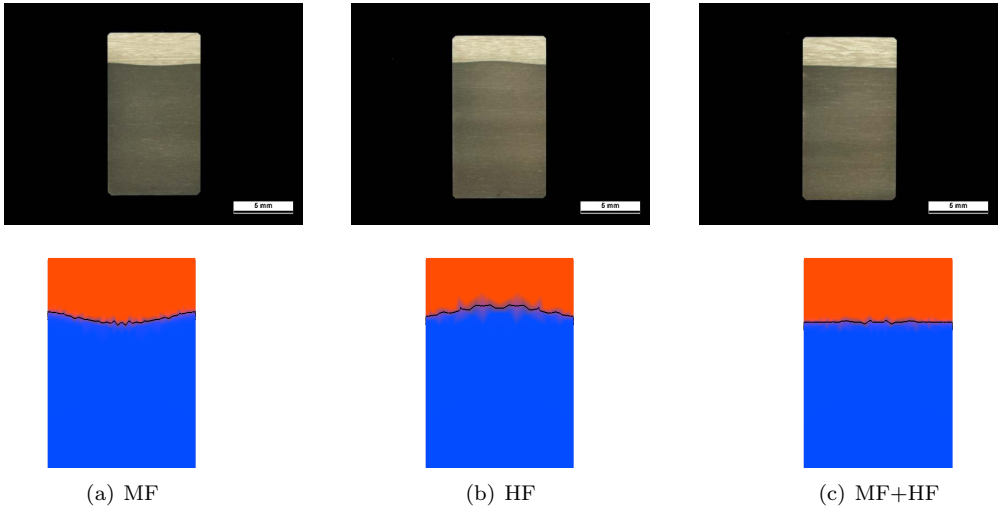


Figure 6.10.: Comparison of the hardening profile between experiment (top row) and numerical simulation (bottom row) for the disc with diameter $d = 47.7$ mm

The relevant model parameters for the transformation kinetics are taken from the literature. The data is based on [54], where the austenitization behaviour is investigated for a quenched and tempered steel 42CrMo4. Therefore, it is only possible to account for the influence of the initial microstructure by modifying the rate law for the evolution of z , which is not within the scope of this work.

As experiments have shown, the surface temperature and the surface hardness depend on the coupling distance. A dependence of the temperature on the initial microstructure could not be observed during the experiments. In contrast to that, the surface hardness depends essentially on the initial microstructure. This can be explained by a different austenitization behaviour. In the state ‘quenched and tempered’, the initial distribution of martensite is fine and cementite precipitates are small. A nearly complete austenitization seems possible within the short heating times. If cementite precipitates are larger, their dissolution and consequently the austenitization process takes more time.

6.3. Numerical simulations for gears

6.3.1. Numerical simulation

The simulation of the induction hardening process yields good results for discs. Nevertheless, the aim of this work is the simulation of the heating stage of multifrequency induction hardening for gears. At the example of a spur gear with diameter $d = 47.7$ mm, $z = 21$ teeth and a modulus of $m = 2$ mm numerical simulations are performed and

compared to experiments. The geometry is depicted in Figure 6.11. Due to symmetry



Figure 6.11.: Geometry of the gear

conditions, the simulations are performed on a reduced geometry consisting of the upper part of half a tooth as in the case of discs, cf. Fig. 6.3. Numerical simulations are performed using a single frequency current, MF and HF separately, and using a simultaneously applied multifrequency current. The parameters are summarized in Table 6.4. The heating time is set to 1.0 s.

	MF	HF	MF + HF
Frequency	15 kHz	200 kHz	15 kHz + 200 kHz
Power	80 % 150 kW	50 % 60 kW	57 % + 40 % 80 kW + 28 kW
Current	775 A	175 A	550 + 140 A

Table 6.4.: Parameter variants for the experimental verification for gears

Medium frequency

As a first example, we consider the heating with medium frequency, $f = 15$ kHz, and a relative power of 80%. The computed temperature θ and the corresponding austenite profile z are depicted in Figure 6.12.

The heating is concentrated to the root of the tooth and the austenitization occurs predominantly in this region. Nevertheless, the tip of the tooth is heated, too. Especially in the early stages of the heating process, when the temperature is still low, the tip of the tooth is heated. As the temperature rises, the material parameters such as the electrical conductivity and the magnetic permeability decrease, which leads to an increase of the penetration depth of the eddy current density, cf. equation (2.1). At this stage, the highest temperatures are attained at the flank of the tooth. This

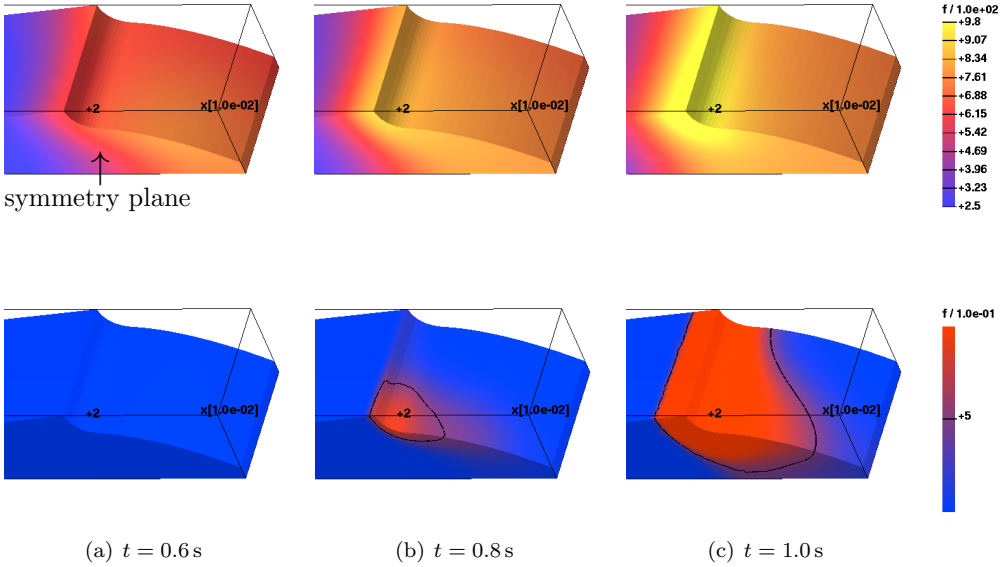


Figure 6.12.: Temperature und austenitic fraction, MF: $f = 15\text{ kHz}$

can be seen in Figure 6.12 (a). With further increase of the temperature, the heating predominantly occurs in the root of the tooth. After a heating time of 1.0 s, the root of the tooth is nearly through hardened.

To illustrate the effect of the Joule heating and the changing penetration depth, the averaged power density per unit volume of the eddy currents, $\bar{Q} = 1/T \int_0^T \sigma |\partial_t \mathbf{A}|^2 dt$, is depicted in Figure 6.13.

In the beginning, the heat power concentrates in the surface region of the flank of the tooth. But already at the early stage, the maximum power is attained at the root of the tooth. Nevertheless, the maximum temperature is attained at the tip or the flank of the tooth, cf. Fig. 6.12. This can be explained by the fact that heat conduction in the root of the tooth is extremely high. Most of the heat is conducted into the core of the gear, while due to the small volume of the tooth, the heat accumulates at the tooth tip.

With rising temperature, the penetration depth of the eddy currents rises. At the end of the heating procedure, the heat power concentrates completely to the root of the tooth, Fig. 6.13 (c). Comparing the beginning and the end of the heating, the magnitude of the heat power reduces significantly. This can be explained by the fact, that above the Curie point, the material loses its ferromagnetic properties and the generated heat reduces drastically.

In Figure 6.17 (a), the temperature t evolution at the tip and the root of the tooth

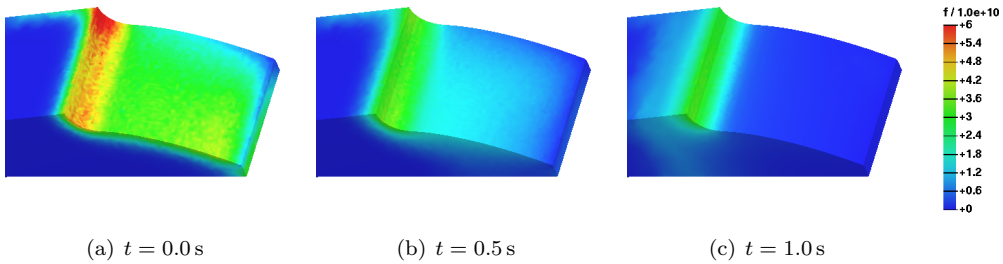


Figure 6.13.: Magnitude of the Joule heat using MF; the skin depth increases with rising temperature

is depicted. This figure illustrates again the afore mentioned process. In the early stage of heating, the temperature increase at the tip of the tooth is higher, though the maximum of the heat power is attained at the root. The reason for this is the heat conduction. During the evolution, the temperature at the root of the tooth rises above the austenitization temperature and the phase transition occurs.

High frequency

As next example, we consider the inductive heating of the gear with high frequency, $f = 195$ kHz, and a relative power of 50%. The results are shown in Figure 6.14.

In this case, the heating concentrates to the tip of the tooth. Nevertheless, as the temperature rises, the skin depth increases and also the root of the tooth is affected by the heating. After a heating time of 1.0s, the tooth is completely transformed to austenite due to the rising skin depth and heat conduction effects. In Figure 6.15 the averaged heat power density is depicted. As in the case of MF, the power is concentrated on the complete flank of the tooth. Compared to MF, Fig. 6.13, the skin depth is reduced. With rising temperature, the penetration depth rises and the maximum of the heat power concentrates at the root of the tooth, Fig. 6.15 (b). But in contrast to MF, there is still heat generation at the tooth tip. Due to heat conduction to the core of the gear and the already mentioned accumulation of heat in the tooth tip, the maximum of the temperature is attained at the tip of the tooth despite the fact that the heat input is larger at the root at later stages of heating, Fig. 6.15 (c). This can also be seen in the temporal temperature evolution in the tip and the root of the tooth, depicted in Figure 6.17 (b) for the case of HF.

Multifrequency concept

The computations using the multifrequency approach are shown in Figure 6.16. The heating occurs simultaneously at the tip, the flank and the root of the tooth. The

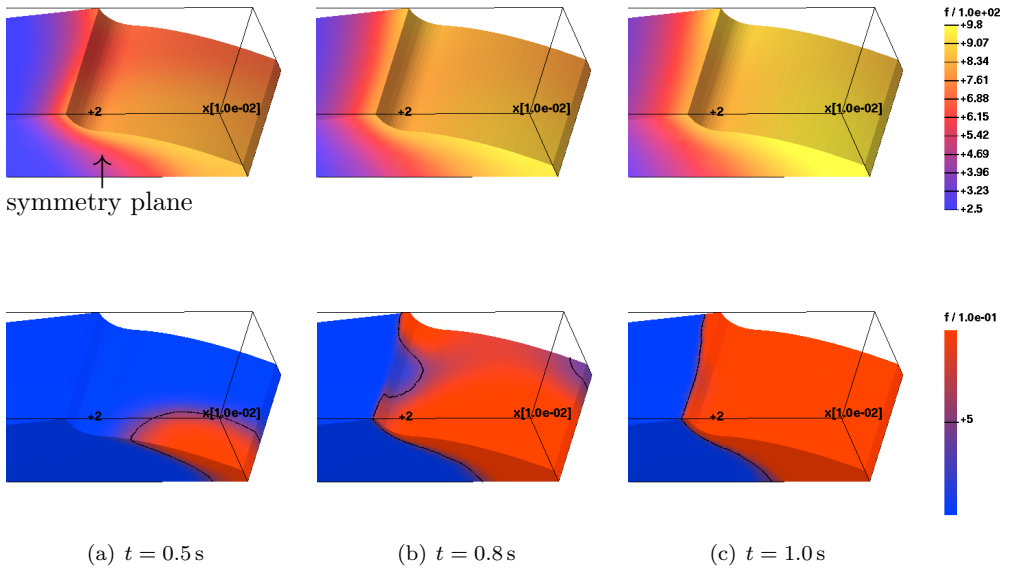


Figure 6.14.: Temperature und austenitic phase fraction, HF: $f = 195$ kHz

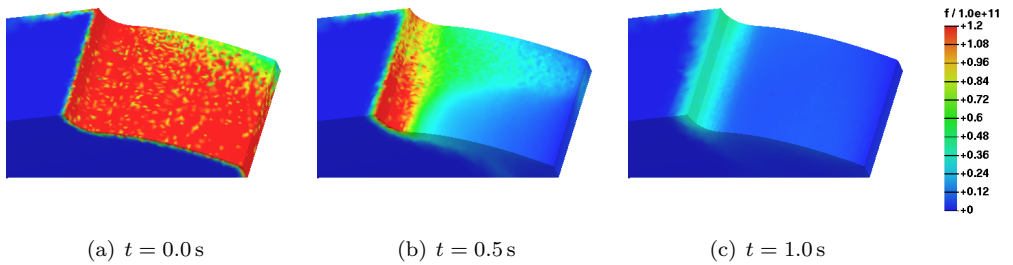


Figure 6.15.: Magnitude of the Joule heat for induction heating using HF

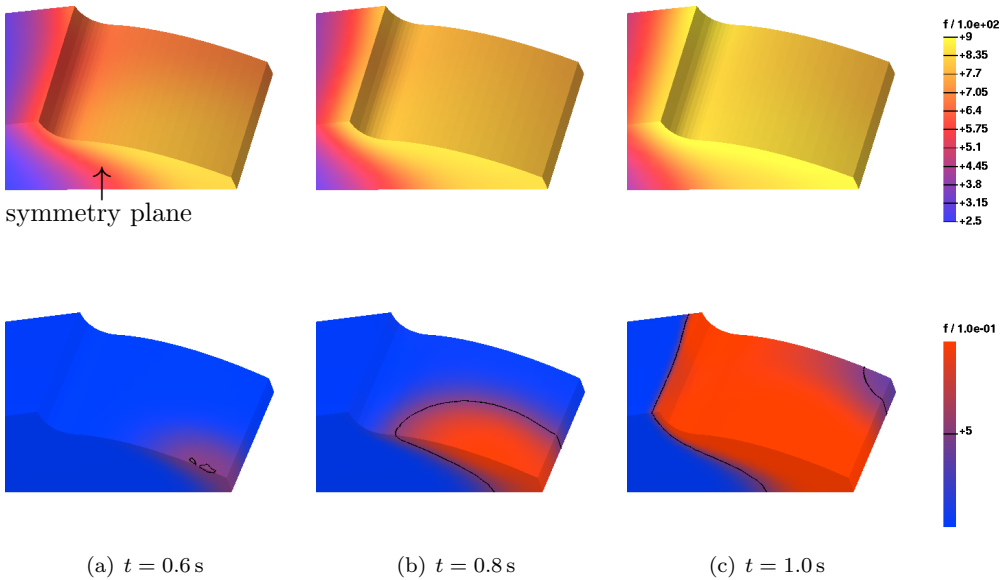


Figure 6.16.: Temperature und austenite fraction, MF+HF: $f = 15$ kHz + 195 kHz

austenitic profile after a heating time of 1.0 s is shown in Figure 6.16 (c). A contour hardening of the gear with the chosen parameters can not be achieved. For a contour hardening, a heating time of 1.0 s might already be too long. Heat conduction effects lead to a nearly complete austenitization of the whole tooth. In order to avoid these effects, shorter heating times are necessary, which demand the use of higher power input.

In Figure 6.17 the temporal evolution of the temperature in the root and the tip of the tooth for the three different heating strategies is shown. This illustrates the heating procedure described in this section once again. For medium frequency, first the tooth tip is heated. Above the Curie temperature, the heat generation in the root of the tooth dominates such that the temperature rises above the austenitization temperature only in the root of the tooth. In Figure 6.17 (a) we can also observe the occurrence of the phase transition. Due to the latent heat that is consumed during the formation of austenite, there is a reduction in the heating rate (approx. at 0.75 s and a temperature of 820 °C, cf. also Fig. 2.4). In the case of high frequency, Fig. 6.17 (b), the temperature reaches the austenitization temperature only in the tooth tip. Due to the effect of the latent heat, a decrease of the temperature in the tip of the tooth occurs at approx. 0.25 s. Since above the Curie temperature, the heat power concentrates in the root of the tooth, the decrease of the heating rate in the tip is stronger than for the medium frequency case. For the multi frequency approach,

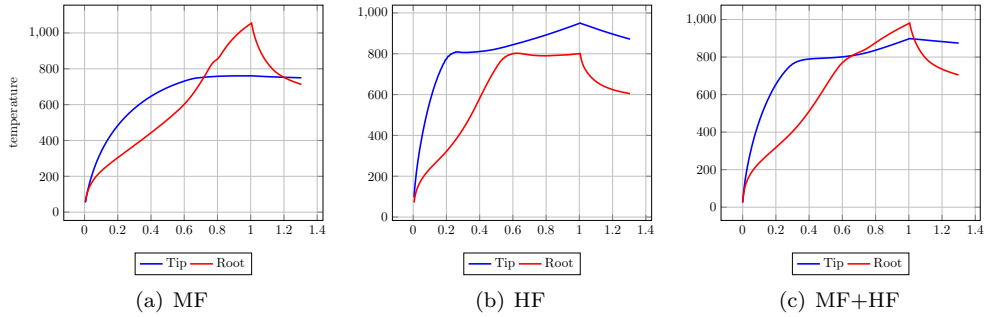


Figure 6.17.: Temporal evolution of the temperature at the tip of the tooth (blue) and the root of the tooth (red)

Fig. 6.17 (c), the temperature at the tip and the root of the tooth rises above the austenitization temperature.

6.3.2. Experimental verification

As in the case of the discs, experiments for the induction hardening of gears have been performed at IWT Bremen. Gears were induction heated using a single frequency current, MF and HF separately, and using the multifrequency concept with the simultaneous supply of MF and HF currents. A comparison of the experiments with the simulation is even more complicated than in the case of discs. It is not possible to measure the surface temperature with sufficient accuracy. A temperature measurement by a pyrometer is only possible after the heating procedure during the transfer of the workpiece to the quenching equipment. In the case of the gear, an exact alignment of the pyrometer with the tip or the root of the tooth is not possible. Due to the rotation of the workpiece during the heating stage, which is necessary to avoid asymmetric heating profiles, there is always the problem that the temperature on the flank of the tooth influences the temperature measurement. The temperature measurement by thermo couples is also not reliable, as has been shown in Figure 6.8. Therefore, we compare the results with the help of micrographs and the measurement of the hardening depth. As in the case of the disc, the latter is related to the computed austenite profile.

In the experiments, the input parameter at the induction hardening machine is the heating time and the relative power in percent. As in the case of the disc, the current is directly related to the relative power. With knowledge of the transformation ratio between the converter and the inductor it is possible to determine the source current density J_{src} in relation to machine specific input parameters.

A comparison of the simulation results with micrographs yields a very good correspondence of the simulated austenite profile to the experimentally obtained martensitic profile, see Figure 6.18.

The measurement of the hardening depth and the penetration depth of the simulated

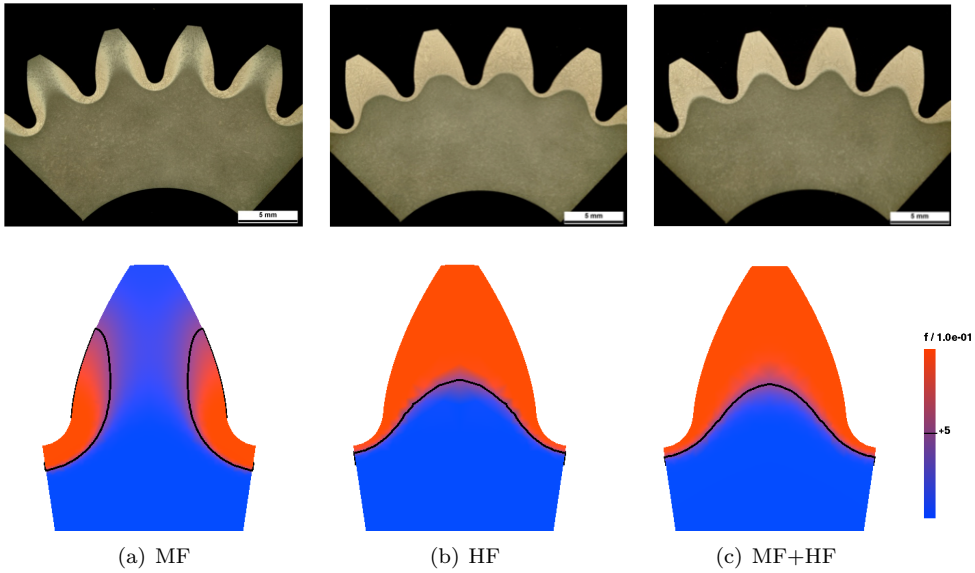


Figure 6.18.: Comparison of the hardening profile between experiment (top row) and numerical simulation (bottom row)

austenite fraction are opposed in Table 6.5. Again, the simulation results reflect the experiments very well.

No.	Power [kW]		Frequency [kHz]		Sim. austenitization depth [mm]		Exp. hardening depth [mm]	
	MF	HF	MF	HF	tip	root	tip	root
1.	150 (80 %)		15		–	0.75 ²	–	0.52
2.		60 (50 %)		195	3.35	0.24	3.77	0.24
3.	80 (57 %)	28 (40 %)	15	195	3.01	0.24	3.37	0.24

Table 6.5.: Comparison of the hardening depth between simulation and experiment

The computations shown in Fig. 6.18 (c) using the multifrequency approach did not lead to a satisfactory contour hardening. For a heating time of 1.0s, the influence of heat conduction effects becomes significant. Therefore, in order to achieve a contour hardening of the gear, shorter heating times are necessary. Further experiments were carried out and are presented in the following section.

²Penetration depth after 0.9s. Due to an overestimation of the MF power, see Section 6.3.4, the heating time is reduced for a comparison between simulation and experiment.

6.3.3. Contour hardening of gears in an industrial setting

In order to obtain a contour hardened gear, shorter heating times in connection with high heating rates are necessary. The experiments related to the following simulations were done on a machine with higher power output at EFD Induction, Freiburg. The objective was the contour hardening of the gear depicted in Figure 6.11. In order to determine the correct machine parameters, experiments with subsequent metallographical analysis of the hardening profile were carried out by trial and error. After several experiments a set of parameters was found leading to a contour hardening of the gear. The machine specific relative power for this experiment were determined as 53% MF and 22 % HF, which correspond to approximately 300 kW MF and 100 kW HF. The heating time was set to 0.25 s, which is a typical heating time to produce a contour hardening.

In order to simulate the process, input parameters in terms of the inductor current are necessary. Unfortunately, a measurement of the current was not possible and the transmission ratio between inverter and inductor for the used induction hardening machine was unknown. Therefore, a calibration of the input data for the simulation was necessary. For this, experiments using only a single frequency, MF and HF separately, were used. The inductor current for the numerical computation was adapted until a correspondence between the computed austenitic profile and the experimentally obtained hardening profile for the cross section of the tooth was achieved. In this way, it was possible to determine the inductor current for pure MF and HF that corresponds to machine specific values of 100 %, compare to Figure 6.19.

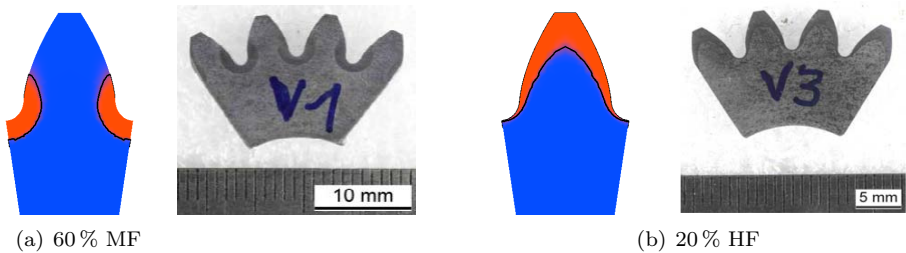


Figure 6.19.: Calibration of the current density for the simulation with respect to experiments using a single frequency, experimental results by courtesy of EFD Induction

In the next step, a numerical simulation using the experimentally determined input data (53% MF and 22 % HF) leading to a contour hardening of the gear was performed without any further adaptation of the parameters. The simulation results are shown in Figure 6.20.

The austenitization starts after approx. 0.1 s at the top corner of the root of the tooth. During the whole heating process, this edge represents a reentrant corner and the highest temperatures are attained there. Continuing in the time evolution, the austenitization occurs along the contour of the whole tooth flank. After 0.25 s the

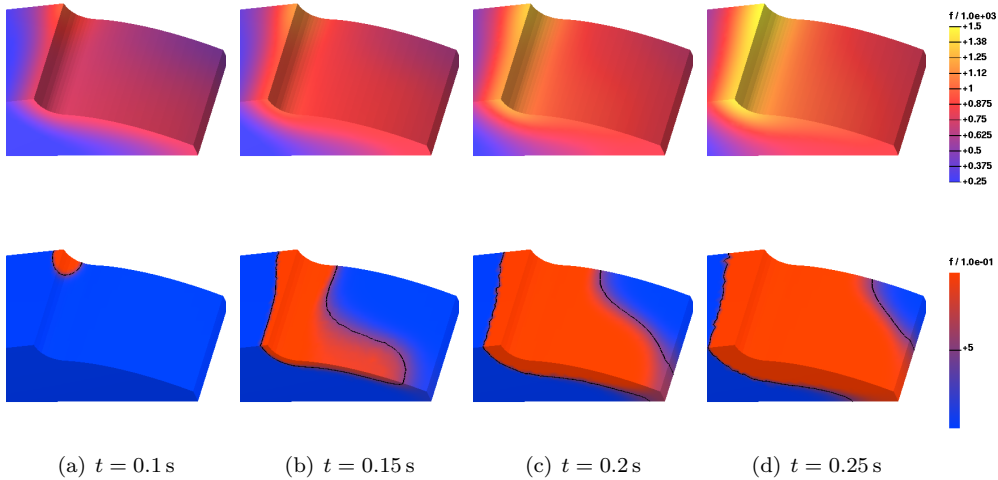


Figure 6.20.: Heating of a gear using the multifrequency approach

austenitization profile follows the contour of the tooth, Figure 6.20 (d). Furthermore, it can be observed that the maximum temperature is approximately $1500\text{ }^{\circ}\text{C}$, which is close to the melting temperature. Often in experiments with high power output, a melting of the workpiece can occur at corners of the workpiece if the heating time is only by fractions of seconds too long.

The austenitization profile follows the contour of the gear in the horizontal cross section. Though, the austenitization profile is not homogeneous in the lateral direction of the tooth. For example, the top edge of the tip of the tooth is not heated beyond the austenitization temperature.

Often in the experimental validation, only the cross section of the gear is analysed by micrographs to determine optimal machine parameters for the contour hardening of gears. With the help of the simulation, it is easily possible to investigate the complete tooth. A comparison of the simulation with experimental results, also to lateral cuts in the tip and the root, is shown in Figure 6.21. As one can see, the non-homogeneous hardening profile along the lateral direction is also observed in the experiment. The correspondence between the simulation and the experimentally determined hardening profiles is very good.

By measurements of the hardness, the hardening depth in the root of the tooth was determined as 0.69 mm and the hardening depth in the tip as 1.79 mm . The hardening depth itself was defined as the distance where the hardness drops below 550 HV . In the simulation, the hardening depth was defined as the distance, where the austenitic fraction z is equal to 0.5 . For the simulation presented in this section, we obtain 0.97 mm in the root and 1.63 mm in the tip of the tooth. One has to keep in mind that the measurement of the hardness is quite error sensitive and the hardening

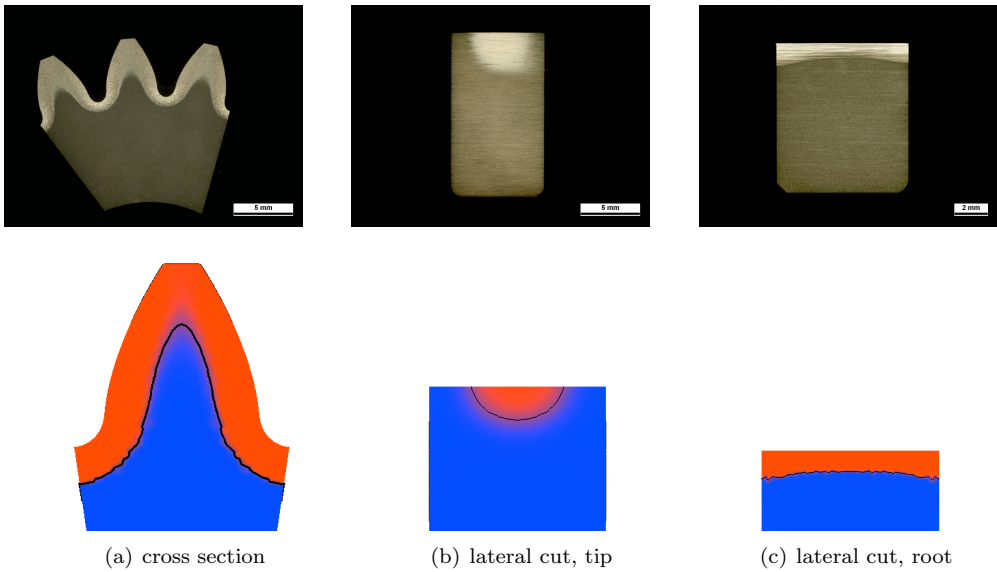


Figure 6.21.: Comparison of the hardening profile between experiment (top row), courtesy of IWT Bremen/EFD Induction, and numerical simulation (bottom row)

depth itself can be defined in different ways. Therefore, the prediction of the hardening depth within some tenth of a millimetre confirms the good agreement of the simulation results with the experiment.

In Figure 6.22, the simulated austenitic fraction in dependence on the distance to the surface in the tip and the root of the tooth is plotted and compared to the measured hardness. The hardness in the root drops to the core hardness very rapidly, while in the tip the transition is quite smoothly. The hardness itself is directly related to the fraction of martensite that formed during the quenching. Compared to the simulated austenitic fraction, which is assumed to transform entirely to martensite during the quenching, one can observe the same behaviour. The decrease of the austenite fraction to zero is very steep at the root, while in the tip, the transition is smooth. One can still observe a small austenitic fraction in a distance of 3 mm from the boundary. In the experiment, the same is obtained.

6.3.4. Discussion

In general, the simulation of the induction hardening process reproduces the experimental results very well. In the final example, a hardening profile is obtained that is close to the contour. There is a reduction in the hardening depth in the root of the tooth. The experimental and the numerical results are in very good agreement, cf. Figures 6.18 and 6.21. Regarding the micrograph of a longitudinal cut through the tip

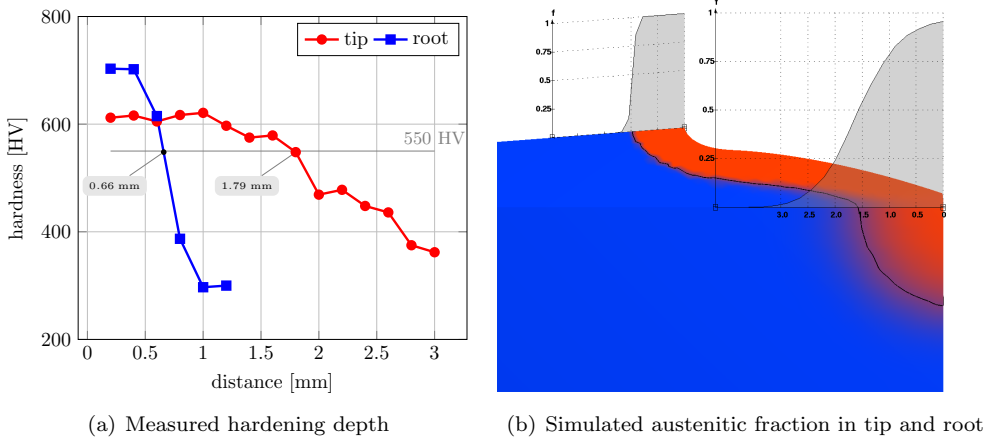


Figure 6.22.: Comparison of the hardening profile between experiment and simulation

and the root of the tooth, the simulation reproduces the concave profile in the root and the convex profile in the tip of the tooth, cf. Figure 6.21 (b) and (c).

Nevertheless, when we compare the simulation to the experimental results, the hardening depth in the root of the tooth tends to be overestimated by the simulation. A similar effect could be observed in the single frequency case when only medium frequency is used and also in the case of the disc.

These differences between experiment and computation can have different reasons. The first one can be a shadowing effect during the quenching: During the inductive heating, the gear rotates to achieve a homogenous hardening result. At the connection of the induction coil to the machine, the field intensity is lower such that the workpiece is usually rotating. During the quenching, the workpiece also rotates. Compared to the heating stage, the rotation speed is much lower, but there is the possibility that the spray quench does not reach the root of the tooth with the same intensity as the tooth tip. This shadowing effect might lead to a reduction of the cooling rate below the critical cooling rate such that the austenite might not transform completely into martensite, which leads finally to a decrease in the hardening depth. The investigated micrographs gave no indication for the formation of additional phases during the quenching. Therefore, the following effect might be a more probable explanation for the mentioned differences.

After evaluating the experiments, it turned out that the current, especially for the medium frequency, is not constant during the whole heating time interval. An examination of the temporal evolution of the inverter current showed that the specified power level is only reached with a delay. Figure 6.23 shows this behaviour exemplary for an experiment with predefined relative MF power of 57%. A constant current is reached with a delay of approx. 0.1 s. In order to account for this effect, it is possible

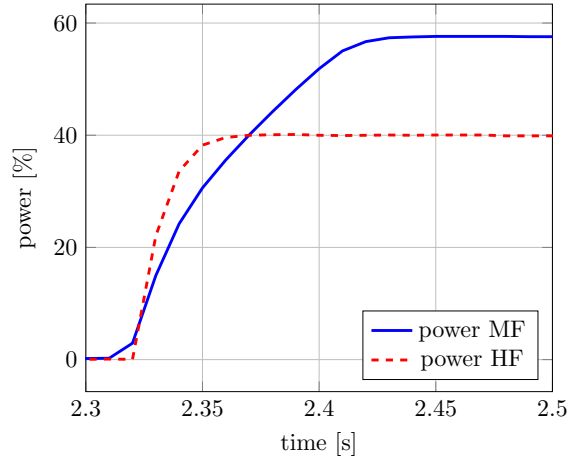


Figure 6.23.: Measured MF and HF power of the machine, the predefined MF power of 57% is attained with a delay of approx. 0.1 s

to consider the time dependent behaviour of the source current in the simulation. But a prediction of the effect is difficult, since it depends on the power and the frequency. For high frequency for example, the delay is not observed.

The delay was also reported by other authors, e. g. [72]. There, an effective heating time is introduced. The power of the source current in the simulation is kept at a constant level, but compared to the experiment, the effective heating time for the simulation is reduced.

Chapter 7.

Conclusion and Outlook

The aim of this work is the the modelling and the simulation of the process of multifrequency induction hardening for complex shaped workpieces in 3D. A model is presented to describe the physical process. It consists of a coupled system of partial and ordinary differential equations, namely the vector potential formulation of Maxwell's equations, the balance of energy and a rate law to describe phase transition phenomena in steel.

For a reduced model, where the material parameters are independent of the temperature but are allowed to depend on the phase fraction and on space, existence and uniqueness of solutions is shown analytically. Furthermore, a numerical algorithm based on the Galerkin method to solve the full nonlinear problem is developed. Due to the nonlinearities, Maxwell's equations are considered in the time domain. The appearance of multiple time scales and of multiple spatial scales resulting from the skin effect requires suitable algorithms to solve the coupled, nonlinear PDE system:

For the approximation of Maxwell's equations, edge elements of Nédélec type are used to discretize the vector potential equation in space. The temperature and the phase fraction of the high temperature phase austenite are discretized using standard conforming P_1 -finite elements. For the discretization in time, semi-implicit time stepping schemes are used to solve the decoupled system of differential equations on different time scales.

The algorithms are implemented in C++ by extending the finite element software `pdelib`, developed at WIAS Berlin, for the use of vector valued edge elements. Simulations are carried out for the induction hardening of discs and of spur gears using a single frequency current, MF or HF, and using the concept of simultaneously applied multifrequency current. The numerical results are compared to experiments carried out by IWT Bremen.

Concluding the results, simulations of the multifrequency induction hardening process are performed, where a very good agreement of the predicted hardening pattern with the experimentally observed martensitic surface layer is achieved. To obtain these results, it is necessary to include the nonlinearities for the material parameters in the simulation. In addition to the temperature dependence of the characteristic material parameters, the nonlinear magnetization curve needs to be considered to get the correct temperature evolution, and consequently the correct hardening pattern. Due to a magnetic saturation behaviour of steel and due to local variations in the magnetic field intensity, the magnetic permeability shows local variations that are essential to

reproduce the experimentally determined hardening profiles for gears, in particular for longitudinal cuts through the tip and the root of the tooth. To avoid the time consuming solution of nonlinear systems of equations, an averaged magnetic permeability is introduced. In this way, the vector potential equation is linearized, but the information of the nonlinear magnetization curve in terms of the saturation behaviour for high magnetic field intensities is included in the simulation.

In electromagnetic applications with high frequency power supply, the skin effect leads to a distribution of the electric current close to the surface of conducting materials. Thus, the heat source in terms of the Joule heat acts only in a small area of the workpiece. We successfully apply residual based error estimators to create adaptive grids, which are capable to resolve the small surface layer but are coarse in areas far away from the region of interest to keep the computational cost at an acceptable level. In addition to this we make use of parallel computing. The software package `pdelib` makes use of parallelization during the assembly of the finite element matrices. Furthermore, the solver PARDISO is used as solution algorithm for the linear systems resulting from the discretization of the PDE system, which also utilizes parallel computing.

As a consequence, it is possible to solve the equations with acceptable computational cost and maintain a sufficient numerical accuracy at the same time. For example, the computational time for the simulation of induction heating for a spur gear using the multifrequency approach as presented in Chapter 6 lies in the range of one to two hours with a number of unknowns of approximately 100 000 for the vector potential \mathbf{A} . In order to determine the process parameters by simulation, a high resolution of the grid might not be necessary, such that the computational time can be reduced to several minutes using a coarse grid.

The quality of the simulation depends on the calibration of the numerical input data with respect to machine specific parameters in an experimental setup. With the availability of measurements of the inductor current or of the inverter current together with knowledge of the transmission ratio between inverter and inductor, a reproduction of the experimental results is possible and the numerical computation can be used to predict the hardening profile.

The example of the contour hardening of a gear described in Section 6.3.3 shows that even in the case where a determination of the inductor current is not possible, a calibration of the numerical simulation with respect to machine specific parameters is possible. Only two experiments for the induction heating of a gear using a single frequency are necessary to determine the correct input parameters. As Figure 6.21 and 6.22 show, a very good prediction of the hardening profile for the contour hardening of gears in the case of short heating times that are typical for industrial applications is possible by the simulation.

With the good correspondence between experiments and simulation it is of great interest to simulate the induction heating process for a wide range of gear geometries. Of major interest in engineering applications are helical gears, where the teeth are cut at an angle to the surface of the gear. This results in a gradual engagement of two teeth, which makes the gear running more smoothly and quietly than spur gears.

Helical gears are used in almost all car transmissions.

Furthermore, it is easily possible to consider different inductor geometries in the simulation and to test their effect on the resulting hardening pattern, especially regarding a lateral cross section of a tooth. In experiments, a change of the inductor geometry is hardly possible. A change of geometry requires a complete reconstruction of the inductor, which is very cost-intensive. A reconfiguration of the inductor geometry is only possible with the help of reliable simulations.

The availability of a software tool that allows the prediction of the hardening pattern opens the door for the optimization of the process. On one hand one is interested in an optimal choice of the process parameters to obtain a desired hardening depth. The process parameters are e. g. the MF- and HF-power and frequency as well as the heating time. On the other hand, there is the possibility to optimize the shape of the inductor to achieve a uniform hardening pattern across the lateral cross section of the tooth. The resulting optimal control problems require the repeated solution of the so called forward problem, equation (5.9), and an adjoint problem, which has a similar structure, [82]. The foundation are effective solution algorithms for the system of partial differential equations as presented in this thesis.

In order to further increase the computational efficiency for the optimal control problems also techniques of model reduction like proper orthogonal decomposition (POD) might be used to resolve all aspects of the model for the optimization problem. Important to mention are the different time scales and the nonlinear material parameters, which are essential to reflect the physical properties of the induction hardening process and finally led to the good agreement between experiments and numerical simulation.

Appendix A.

Appendix

A.1. Integral identities

For the derivation of the jump conditions in Chapter 3 and the weak formulation in Chapters 4 and 5 the following fundamental integral identities are used, which are cited from literature, e. g. [29].

Theorem 3 (Gauss). *Let $\Omega \subset \mathbb{R}^d$ denote a compact set with smooth boundary $\partial\Omega$ and let $\mathbf{v} : \Omega \rightarrow \mathbb{R}^d$ denote a continuously differentiable vector field. Then*

$$\int_{\Omega} \operatorname{div} \mathbf{v} \, dx = \int_{\partial\Omega} \mathbf{v} \cdot \mathbf{n} \, da,$$

where \mathbf{n} denotes the outward unit normal vector of the boundary $\partial\Omega$.

Theorem 4 (Stokes). *Let $\Omega \subset \mathbb{R}^3$ denote an open set and let $\mathbf{v} : \Omega \rightarrow \mathbb{R}^d$ denote a continuously differentiable vector field. Furthermore, let $\Sigma \subset V$ denote a two dimensional regular sub manifold with an outward unit normal vector \mathbf{n} and denote by $\boldsymbol{\tau}$ the unit tangential vector of the boundary curve $\partial\Sigma$ of Σ . Then*

$$\int_{\Sigma} \operatorname{curl} \mathbf{v} \cdot \mathbf{n} \, da = \int_{\partial\Sigma} \mathbf{v} \cdot \boldsymbol{\tau} \, ds.$$

As a consequence of Gauss' theorem, one obtains the following formulas of partial integration that are required to derive the weak formulation in Chapters 4 and 5.

Corollary 5 (Green's formula). *Let $\varphi : \Omega \rightarrow \mathbb{R}$ denote a continuously differentiable function on Ω and let $\mathbf{v} : \Omega \rightarrow \mathbb{R}^d$ denote a continuously differentiable vector field. Then there holds the following identity*

$$\int_{\Omega} \varphi \operatorname{div} \mathbf{v} \, dx = \int_{\partial\Omega} \varphi \mathbf{v} \cdot \mathbf{n} \, da - \int_{\Omega} \nabla \varphi \cdot \mathbf{v} \, dx.$$

Furthermore, there holds with $\mathbf{w} : \Omega \rightarrow \mathbb{R}^d$

$$\int_{\Omega} \operatorname{curl} \mathbf{v} \cdot \mathbf{w} \, dx - \int_{\Omega} \mathbf{v} \cdot \operatorname{curl} \mathbf{w} \, dx = \int_{\partial\Omega} (\mathbf{v} \times \mathbf{n}) \cdot \mathbf{w} \, da.$$

A.2. Material parameters for the steel 42CrMo4

A.2.1. Specific heat capacity

For the specific heat capacity c_p there is only little data available in literature for different types of steels. In order to determine the temperature dependent specific heat capacity for the steel 42CrMo4, the thermodynamic database Thermo-Calc [81] is used. The graph is depicted in Figure A.1. The peak at a temperature of approx.

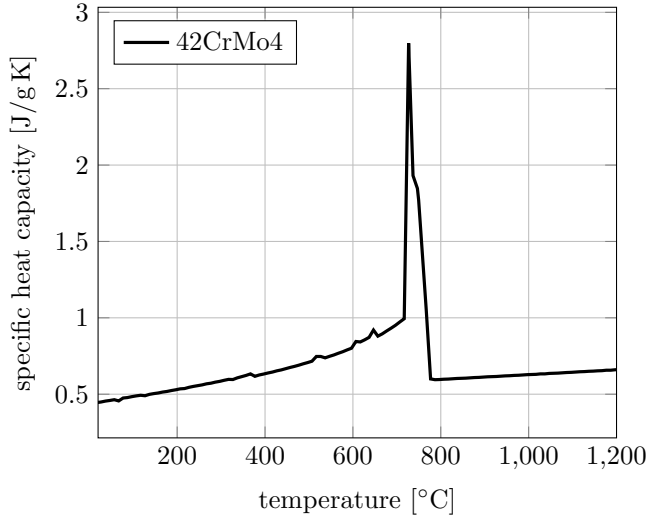


Figure A.1.: Specific heat capacity, [81]

750 °C emerges from the latent heat that is consumed during the phase transition from ferrite to austenite. Since the latent heat is directly treated in our model, we separate the specific heat capacity for the low temperature region and the austenitic region. A possible under- or overcooling is taken into account by extrapolation of the curves for the single phase region.

A.2.2. Heat conductivity

The temperature dependent heat conductivity κ is depicted in Figure A.2. The data is based on [75].

A.2.3. Electrical conductivity

The electrical conductivity σ is depicted in Figure A.3. The data for ferrite is taken from [75], the data for austenite is due to [11]. In the region of the phase transition between 600 °C and 820 °C interpolation of the data for the pure phases is used.

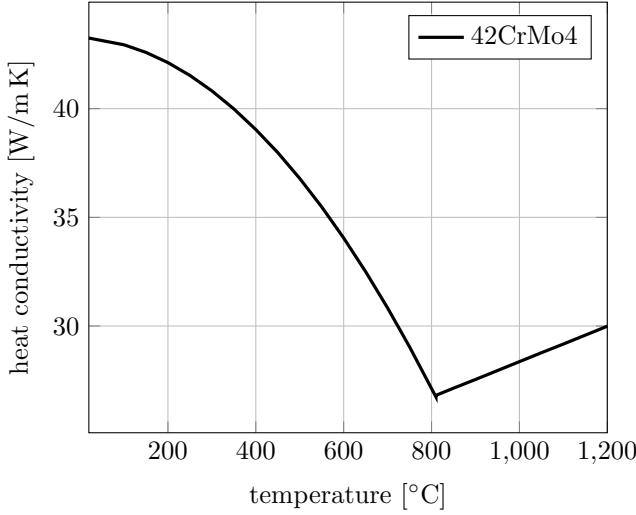


Figure A.2.: Heat conductivity, [75]

A.2.4. Magnetic permeability

The temperature dependent magnetization curve $\mathbf{B} = f(|\mathbf{H}|, \theta)$ was determined using a vibration magnetometer. The measurements were carried out by IWT Bremen. The temperature dependent data is shown in Figure A.4. The measured data was fitted to the commonly used Fröhlich-Kennelly model, where the magnetization curve is modelled by

$$\mathbf{B} = \mu_0 \mathbf{H} + \frac{\mathbf{H}}{a + b|\mathbf{H}|}$$

with parameters $a, b > 0$. In order to account for the temperature dependence, we use the following approach, [77]. A function $f(\theta)$ is introduced such that

$$\mathbf{B} = \mu_0 \mathbf{H} + f(\theta) \frac{\mathbf{H}}{a + b|\mathbf{H}|}.$$

The temperature dependent factor $f(\theta)$ can be modelled as follows, [77]

$$f(\theta) = \left(\frac{\theta_C^2 - \theta^2}{\theta_C^2 - \theta_0^2} \right)^{\frac{1}{4}},$$

where θ_C and θ_0 denote the Curie and the room temperature in Kelvin, respectively. Then, for the magnetic permeability $\mu = \mathbf{B}/\mathbf{H}$ there holds

$$\mu = \begin{cases} \mu_0 \left(1 + f(\theta) \frac{1}{a+b|\mathbf{H}|} \right) & \text{for } \theta \leq \theta_C \\ \mu_0 & \text{for } \theta > \theta_C. \end{cases}$$

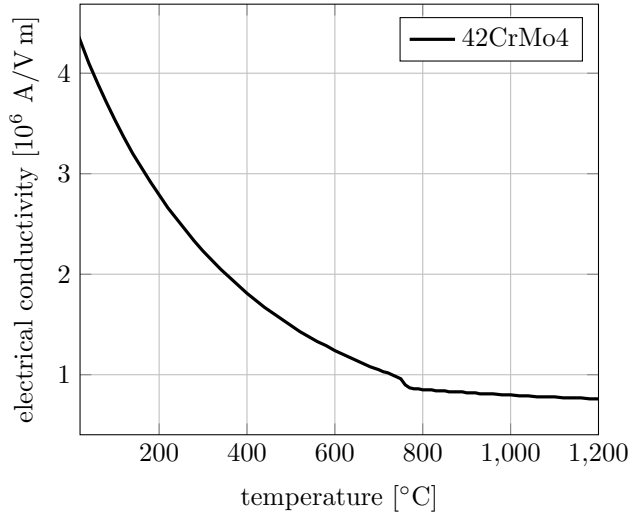


Figure A.3.: Electrical conductivity, [11, 75]

A.2.5. Further parameters

The experimental measurement of the latent heat \mathcal{L} is quite difficult. Comparing different citations, there are quite big differences in the values for the latent heat that is consumed during the formation of austenite. For the rate law describing the formation of austenite, we referred to [54]. Therefore, we use this reference for the latent heat and define

$$\mathcal{L} = 65.2 \cdot 10^7 \text{ J/m}^3.$$

The density ρ that appears in the heat equation refers to the density of a fixed reference configuration. The density of the steel 42CrMo4 for the initial microstructure at room temperature is given as, [65],

$$\rho = 7834 \text{ kg/m}^3.$$

A.3. Averaging of the Joule heat

The problem that arises in the time discretization of the energy balance lies in the fact that the heat source is given by the oscillatory Joule heat $\sigma |\partial_t \mathbf{A}|^2$. The frequency is related to the source currents, lies in the range of $f = 10 - 200$ kHz leading to a typical time scale of $10^{-6} - 10^{-5}$ s. However, the time scale of the heat equation lies in the range of some seconds. It is hardly possible for a numerical time stepping scheme to resolve the oscillations of the Joule heat on the large time interval. This would require too many time steps leading to large computational times.

Due to the damping properties of the Laplace operator it is even not necessary to resolve changes of the temperature on the short time scale. The typical approach for

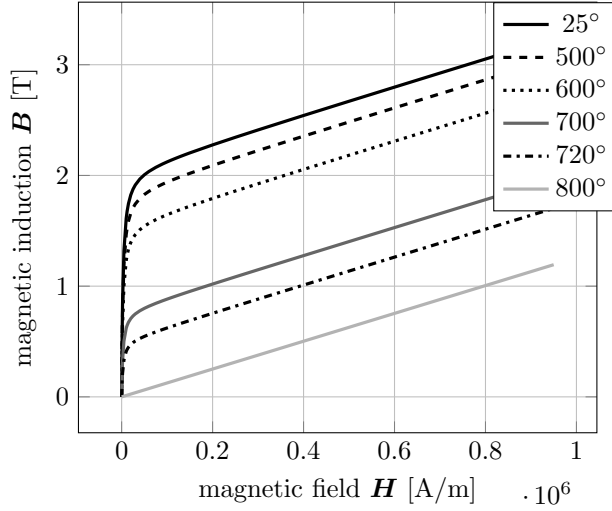


Figure A.4.: Magnetization curve, fit to measurements conducted by IWT Bremen

eddy current problems is to replace the time dependent Joule heat term by an averaged value over one period [18], i. e.

$$\bar{Q} = \frac{\omega}{2\pi} \int_0^{\frac{2\pi}{\omega}} \sigma |\partial_t \mathbf{A}|^2 dt. \quad (\text{A.1})$$

We want to give a short mathematical justification for this approach. For this, we consider the heat equation in a one dimensional infinite domain for a dimensionless temperature u . It reads

$$\partial_t u - \partial_{xx} u = Q \quad \text{in } \mathbb{R} \quad \text{and } t > 0$$

with $u(x, 0) = u_0$ and Q denoting the Joule heat. We decompose the Joule heat term into an average value and oscillations such that $Q = \bar{Q} + Q_{\text{osc}}$. Corresponding to that, we decompose u also into two parts \bar{u} and u_{osc} such that \bar{u} solves

$$\partial_t \bar{u} - \partial_{xx} \bar{u} = \bar{Q} \quad \text{with } \bar{u}(x, 0) = u_0 \quad (\text{A.2})$$

and u_{osc} solves

$$\partial_t u_{\text{osc}} - \partial_{xx} u_{\text{osc}} = Q_{\text{osc}} \quad \text{with } u_{\text{osc}}(x, 0) = 0.$$

The exact solution of the non-homogeneous heat equation can be written as a convolution of the heat kernel $H(x, t)$ and the right hand side such that

$$u_{\text{osc}} = \int_0^t \int_{\mathbb{R}} H(x - y, t - s) Q_{\text{osc}}(y, s) dy ds$$

with

$$H(x, t) = \frac{1}{\sqrt{4\pi t}} \exp\left(-\frac{x^2}{4t}\right).$$

The right hand side Q_{osc} is an oscillating term with zero mean. For simplicity, we assume that it is an harmonic function in time with frequency ω , whose power is concentrated at $x = 0$ such that $Q_{\text{osc}}(x, t) = \sin(\omega t)\delta(x)$ with $\delta(x)$ denoting the Dirac-delta. Then,

$$u_{\text{osc}}(x, t) = \int_0^t \frac{1}{\sqrt{4\pi s}} \exp\left(-\frac{x^2}{4s}\right) \sin \omega s \, ds.$$

Since the maximum of u_{osc} is expected at $x = 0$ we want to compute $u(0, t)$. Evaluating the integral at $x = 0$ using e. g. Mathematica yields the following expression

$$u_{\text{osc}}(0, t) = \frac{1}{2\omega} \left(\sin(\omega t) C\left(\sqrt{\frac{2\omega t}{\pi}}\right) - \cos(\omega t) S\left(\sqrt{\frac{2\omega t}{\pi}}\right) \right),$$

where $C(z)$ and $S(z)$ denote the Fresnel integrals, [1], that are defined as

$$C(z) = \int_0^z \cos(\pi/2x^2) \, dx \quad \text{and} \quad S(z) = \int_0^z \sin(\pi/2x^2) \, dx.$$

For $z \gg 1$ there hold the asymptotic expansions

$$C(z) \approx \frac{1}{2} + \frac{1}{\pi z} \sin\left(\frac{1}{2}\pi z^2\right) \quad \text{and} \quad S(z) \approx \frac{1}{2} - \frac{1}{\pi z} \cos\left(\frac{1}{2}\pi z^2\right).$$

We are interested in the long time behaviour for high frequencies ω such that this approximation is reasonable. Then there holds

$$u_{\text{osc}}(0, t) \approx \frac{1}{\sqrt{2\omega}} \left(\frac{1}{\sqrt{2}} \sin(\omega t - \pi/4) + \frac{1}{\sqrt{2\pi\omega t}} \right). \quad (\text{A.3})$$

From this expression, we obtain that the oscillatory part of the temperature u_{osc} consist of two contributions. The first term in (A.3) corresponds to an oscillation of the temperature around the average solution \bar{u} with an amplitude proportional to $1/\sqrt{\omega}$. The second term in (A.3) is proportional to $1/\omega$ and tends to zero as $t \rightarrow \infty$.

Since we are only interested in the case $\omega \gg 1$ there is the justification that the oscillatory part u_{osc} can be neglected. Consequently,

$$u \approx \bar{u},$$

where \bar{u} is given by (A.2).

Finally, the consequence for the energy balance is that the oscillatory Joule heat can be approximated by an averaged value such that

$$\rho c_p \partial_t \theta + \text{div } \kappa \nabla \theta = \bar{Q} - \rho \mathcal{L} \partial_t z, \quad (\text{A.4})$$

where \bar{Q} is given by (A.1). Of course, the Joule heat still depends on time, since the coefficients σ and μ depend on the temperature θ . But since θ changes only on the large time scale, the averaged Joule heat \bar{Q} also changes only on the large time scale.

Bibliography

- [1] M. ABRAMOWITZ AND I. A. STEGUN, *Handbook of Mathematical Functions: With Formulas, Graphs, and Mathematical Tables*, vol. 55, Dover Publications, 1964.
- [2] M. AVRAMI, *Kinetics of Phase Change. I General Theory*, The Journal of Chemical Physics, 7 (1939), pp. 1103–1112.
- [3] F. BACHINGER, U. LANGER, AND J. SCHÖBERL, *Numerical analysis of nonlinear multiharmonic eddy current problems*, Numerische Mathematik, 100 (2005), pp. 593–616.
- [4] F. BACHINGER, U. LANGER, AND J. SCHÖBERL, *Efficient solvers for nonlinear time-periodic eddy current problems*, Computing and Visualization in Science, 9 (2006), pp. 197–207.
- [5] H.-J. BARGEL AND G. SCHULZE, *Werkstoffkunde*, Springer-Verlag Berlin, Heidelberg, 9. ed., 2005.
- [6] F. BAY, V. LABBE, Y. FAVENNEC, AND J. L. CHENOT, *A numerical model for induction heating processes coupling electromagnetism and thermomechanics*, International Journal for Numerical Methods in Engineering, 58 (2003), pp. 839–867.
- [7] R. BECK, R. HIPTMAIR, R. H. HOPPE, AND B. WOHLMUTH, *Residual based a posteriori error estimators for eddy current computation*, ESAIM: Mathematical Modelling and Numerical Analysis, 34 (2000), pp. 159–182.
- [8] K. BERGGREN AND H. STIELE, *Induction Heating: A Guide to the Process and Its Benefits*, Gear Solutions, 7 (2012), pp. 40–46.
- [9] J. BEY, *Tetrahedral grid refinement*, Computing, 55 (1995), pp. 355–378.
- [10] H. K. D. H. BHADOSHIA AND R. W. K. HONEYCOMBE, *Steels: Microstructure and Properties*, Butterworth-Heinemann, 2006.
- [11] U. BOHNENKAMP AND R. SANDSTRÖM, *Evaluation of the electrical resistivity of steels*, Steel research, 71 (2000), pp. 410–416.
- [12] F. A. BORNEMANN, B. ERDMANN, AND R. KORNHUBER, *A posteriori error estimates for elliptic problems in two and three space dimensions*, SIAM Journal on Numerical Analysis, 33 (1996), pp. 1188–1204.

- [13] D. BRAESS, *Finite Elemente. Theorie, schnelle Löser und Anwendungen in der Elastizitätstheorie*, Berlin: Springer, 3. ed., 2003.
- [14] S. C. BRENNER AND L. R. SCOTT, *The mathematical theory of finite element methods*, vol. 15, Springer, 2008.
- [15] C. CARSTENSEN AND R. H. HOPPE, *Unified framework for an a posteriori error analysis of non-standard finite element approximations of $H(\text{curl})$ -elliptic problems*, *Journal of Numerical Mathematics*, 17 (2009), pp. 27–44.
- [16] C. CHABOUDEZ, S. CLAIN, R. GLARDON, D. MARI, J. RAPPAZ, AND M. SWIERKOSZ, *Numerical modeling in induction heating for axisymmetric geometries*, *Magnetics, IEEE Transactions on*, 33 (Jan 1997), pp. 739–745.
- [17] P. G. CIARLET, *The Finite Element Method for Elliptic Problems*, North Holland, Amsterdam, 1978.
- [18] S. CLAIN, J. RAPPAZ, M. SWIERKOSZ, AND R. TOUZANI, *Numerical modeling of induction heating for two-dimensional geometries*, *Mathematical models and methods in applied sciences*, 3 (1993), pp. 805–822.
- [19] J. CRANK AND P. NICOLSON, *A practical method for numerical evaluation of solutions of partial differential equations of the heat-conduction type*, *Mathematical Proceedings of the Cambridge Philosophical Society*, 43 (1947), pp. 50–67.
- [20] P. DEUFLHARD AND A. HOHMANN, *Numerische Mathematik I. Eine algorithmisch orientierte Einführung*, vol. 4, Walter de Gruyter, Berlin, 2008.
- [21] W. DÖRFLER, *A Convergent Adaptive Algorithm for Poisson's Equation*, *SIAM Journal on Numerical Analysis*, 33 (1996), pp. 1106–1124.
- [22] P.-É. DRUET, *Higher integrability of the Lorentz force for weak solutions to Maxwell's equations in complex geometries*, *WIAS preprint no. 1270*, (2007).
- [23] P.-É. DRUET, O. KLEIN, J. SPREKELS, F. TRÖLTZSCH, AND I. YOUSEPT, *Optimal control of three-dimensional state-constrained induction heating problems with nonlocal radiation effects*, *SIAM Journal on Control and Optimization*, 49 (2011), pp. 1707–1736.
- [24] M. DURAND-CHARRE, *Microstructure of Steels and Cast Irons*, Springer Verlag, Berlin, Heidelberg, New York, 2004.
- [25] G. DUVAUT AND J. L. LIONS, *Inequalities in mechanics and physics*, Springer-Verlag, Berlin, New York, 1976.
- [26] S. V. DZLIEV, *Prinzipien des Aufbaus von Speisesystemen für Anlagen zum Induktionshärten von Zahnrädern mit Zweifrequenzerwärmung*, *Elektrowärme International*, 4 (2005), pp. 176–180.

- [27] L. R. EGAN AND E. P. FURLANI, *A computer simulation of an induction heating system*, Magnetics, IEEE Transactions on, 27 (1991), pp. 4343–4354.
- [28] V. ESTEVE, J. JORDAN, E. J. DEDE, E. SANCHIS-KILDERS, AND E. MASET, *Induction heating inverter with simultaneous dual-frequency output*, Applied Power Electronics Conference and Exposition, 2006. APEC '06. Twenty-First Annual IEEE, (2006), pp. 1505–1509.
- [29] O. FORSTER, *Analysis 3: Integralrechnung im \mathbf{R}^n mit Anwendungen*, Vieweg Studium: Aufbaukurs Mathematik. Wiesbaden, 3. ed., 1999.
- [30] V. GIRAULT AND P.-A. RAVIART, *Finite element methods for Navier-Stokes equations. Theory and algorithms*, Springer Series in Computational Mathematics, 5, Springer-Verlag, Berlin, 1986.
- [31] M. T. GONZÁLEZ MONTESINOS AND F. ORTEGÓN GALLEGO, *On an induction-conduction PDEs system in the harmonic regime*, Nonlinear Analysis: Real World Applications, 15 (2014), pp. 58–66.
- [32] R. GRIESINGER, *The Boundary Value Problem $\operatorname{rot} u = f$, u Vanishing at the Boundary and the Related Decompositions of L^q and $H_0^{1,q}$: Existence*, Annali dell'Università di Ferrara, 36 (1990), pp. 15–43.
- [33] C. GROSSMANN AND H.-G. ROOS, *Numerische Behandlung partieller Differentialgleichungen*, Vieweg+Teubner Verlag, 2005.
- [34] P. HAASEN, *Physikalische Metallkunde, 2. Auflage.*, Springer Verlag, Berlin, 1985.
- [35] E. HAIRER, S. P. NØRSETT, AND G. WANNER, *Solving Ordinary Differential Equations II: Stiff and Differential-Algebraic Problems*, Springer, 1996.
- [36] S. HANSSON AND M. FISK, *Simulations and measurements of combined induction heating and extrusion processes*, Finite Elements in Analysis and Design, 46 (2010), pp. 905–915.
- [37] R. HIPTMAIR, *Multigrid Method for Maxwell's Equations*, SIAM Journal on Numerical Analysis, 36 (1998), pp. 204–225.
- [38] D. HÖMBERG, *A mathematical model for induction hardening including mechanical effects*, Nonlinear Analysis: Real World Applications, 5 (2004), pp. 55–90.
- [39] D. HÖMBERG, T. PETZOLD, AND E. ROCCA, *Analysis and simulations of multifrequency induction hardening*. WIAS Preprint No. 1910, 2013.
- [40] D. HÖMBERG AND J. SOKOLOWSKI, *Optimal Shape Design of Inductor Coils for Surface Hardening*, SIAM Journal on Control and Optimization, 42 (2003), pp. 1087–1117.

- [41] R. H. HOPPE AND R. KORNHUBER, *Multi-grid solution of two coupled Stefan equations arising in induction heating of large steel slabs*, International Journal for Numerical Methods in Engineering, 30 (1990), pp. 779–801.
- [42] J. D. JACKSON, *Classical Electrodynamics*, Wiley, third ed., 1998.
- [43] A. JACOT, M. SWIERKOSZ, J. RAPPAZ, M. RAPPAZ, AND D. MARI, *Modelling of Electromagnetic Heating, Cooling and Phase Transformations during Surface Hardening of Steels*, Journal de Physique IV, 06 (1996), pp. C1–203–C1–213.
- [44] W. A. JOHNSON AND R. F. MEHL, *Reaction kinetics in processes of nucleation and growth*, Transactions of American Institute of Mining and Metallurgical Engineers, 135 (1939), pp. 416–458.
- [45] J. KAČUR, *Method of Rothe in evolution equations*, Teubner Texts in Mathematics, 80, BSB B. G. Teubner Verlagsgesellschaft, Leipzig, 1985.
- [46] T. KAWANAGO, *Estimation L^p – L^q des solutions de $u_t = \Delta\phi(u) + f$* , Comptes Rendus de l'Académie des Sciences, 317 (1993), pp. 821–824.
- [47] D. P. KOISTINEN AND R. E. MARBURGER, *A general equation prescribing the extent of the austenite-martensite transformation in pure iron-carbon alloys and plain carbon steels*, Acta Metallurgica, 7 (1959), pp. 59–60.
- [48] D. LABRIDIS AND P. DOKOPOULOS, *Calculation of eddy current losses in non-linear ferromagnetic materials*, Magnetics, IEEE Transactions on, 25 (1989), pp. 2665–2669.
- [49] J. B. LEBLOND AND J. DEVAUX, *A new kinetic model for anisothermal metallurgical transformations in steels including effect of austenite grain size*, Acta Metallurgica, 32 (1984), pp. 137–146.
- [50] G. LEHNER, *Elektromagnetische Feldtheorie*, vol. 6, Springer Verlag, Berlin, Heidelberg, 2008.
- [51] D. LIEDTKE AND H. STIELE, *Wärmebehandlung von Stahl – Randschichthärten*. Merkblatt 236, Stahl-Informations-Zentrum, 2009.
- [52] I. MAGNABOSCO, P. FERRO, A. TIZIANI, AND F. BONOLLO, *Induction heat treatment of a ISO C45 steel bar: Experimental and numerical analysis*, Computational Materials Science, 35 (2006), pp. 98–106.
- [53] L. MARKEGARD AND W. SCHWENK, *Method and device for surface hardening of rotation symmetrical parts through inductive heating by means of at least two different frequencies*, European Patent, 91906813 (1995).
- [54] T. MIOKOVIC, *Analyse des Umwandlungsverhaltens bei ein- und mehrfacher Kurzzeithärtung bzw. Laserstrahlhärtung des Stahls 42CrMo4*, PhD thesis, Universität Karlsruhe, 2005.

- [55] P. MONK, *Finite Element Methods for Maxwell's Equations*, Oxford University Press, USA, 2003.
- [56] I. MÜLLER, *Thermodynamics*, Pitman, 1985.
- [57] J. C. NÉDÉLEC, *Mixed finite elements in R^3* , Numerische Mathematik, 35 (1980), pp. 315–341.
- [58] ———, *A new family of mixed finite elements in R^3* , Numerische Mathematik, 50 (1986), pp. 57–81.
- [59] J. ORLICH, A. ROSE, AND P. WIEST, *Atlas zur Wärmebehandlung der Stähle*, vol. 3, Verlag Stahleisen, Düsseldorf, 1973.
- [60] J. OSTROWSKI, *Boundary Element Methods for Inductive Hardening*, PhD thesis, Eberhard-Karls-Universität zu Tübingen, 2003.
- [61] *pdelib2*. <http://www.wias-berlin.de/software/pdelib/>. last checked: 19.12.2013.
- [62] H.-J. PETER, *Das induktive Randschichthärten mit dem Zweifrequenz-Simultan-Verfahren (SDF-Verfahren) - Anwendung und Erfahrungen*, HTM Härtereitechnische Mitteilungen, 59 (2004), pp. 119–125.
- [63] D. A. PORTER AND K. E. EASTERLING, *Phase Transformations in Metals and Alloys, 2nd edition*, Taylor & Francis, 1992.
- [64] J. PRÜSS, *Maximal regularity for evolution equations in L^p -spaces*, Conferenze del Seminario di Matematica dell'Università di Bari, 285 (2003), pp. 1–39.
- [65] F. RICHTER, *Physikalische Eigenschaften von Stählen und ihre Temperaturabhängigkeit*, Stahleisen-Sonderberichte 10, 1983.
- [66] O. SCHENK AND K. GÄRTNER, *PARDISO – User Guide Version 4.1.2*.
- [67] ———, *On fast factorization pivoting methods for sparse symmetric indefinite systems*, Electronic Transactions on Numerical Analysis, 23 (2006), pp. 158–179.
- [68] D. SCHLESSELMANN AND B. NACKE, *Anwendungen der numerischen Simulation des induktiven Randschichthärtens*, Elektrowärme International, 71 (2013), pp. 89–94.
- [69] A. SCHMIDT AND K. G. SIEBERT, *Design of adaptive finite element software: The finite element toolbox ALBERTA*, Springer LNCSE Series 42, 2005.
- [70] J. SCHÖBERL, *A posteriori error estimates for Maxwell equations*, Mathematics of Computation, 77 (2008), pp. 633–649.
- [71] J. SCHÖBERL AND S. ZAGLMAYR, *High order Nédélec elements with local complete sequence properties*, COMPEL: The International Journal for Computation and Mathematics in Electrical and Electronic Engineering, 24 (2005), pp. 374–384.

- [72] M. SCHWENK, *Entwicklung und Validierung eines numerischen Simulationsmodells zur Beschreibung der induktiven Ein- und Zweifrequenzrandschichthärtung am Beispiel von vergütetem 42CrMo4*, PhD thesis, Karlsruher Institut für Technologie (KIT), 2012.
- [73] W. SCHWENK AND H.-J. PETER, *Anwendungen des Zweifrequenz-Simultan-Verfahrens zum induktiven Randschichthärten*, Elektrowärme International, (2002), pp. 13–18.
- [74] W. R. SCHWENK, *Simultaneous Dual-Frequency Induction Hardening*, Heat Treating Progress, (2003), pp. 35–38.
- [75] *SEW 310: Physikalische Eigenschaften von Stählen*, Stahl-Eisen-Werkstoffblätter des Vereins Deutscher Eisenhüttenleute, Verlag Stahleisen, Düsseldorf, 1992.
- [76] H. SI, *TetGen: A quality tetrahedral mesh generator and a 3D Delaunay triangulator (Version 1.5 — User's Manual)*, Tech. Rep. 13, Weierstrass Institute for Applied Analysis and Stochastics, 2013.
- [77] H. J. SIEBER, *Bestimmung der Permeabilität und ihrer Rückwirkung auf die Energieübertragung beim induktiven Erwärmen*, Rheinisch-Westfälische Technische Hochschule Aachen, 1978.
- [78] J. SIMON, *Compact sets in the space $L^p(0, T; B)$* , Annali di Matematica Pura ed Applicata, 146 (1986), pp. 65–96.
- [79] P. SOLIN, K. SEGETH, AND I. DOLEZEL, *Higher-order finite element methods*, CRC Press, 2003.
- [80] B. SUHR, F. FRERICHS, I. HÜSSLER, AND M. WOLFF, *Evaluation of models for martensitic transformation and trip via comparison of experiments and simulations*, Materialwissenschaft und Werkstofftechnik, 40 (2009), pp. 460–465.
- [81] *Thermo-Calc*. <http://www.thermocalc.com>. last checked: 19.12.2013.
- [82] F. TRÖLTZSCH, *Optimale Steuerung partieller Differentialgleichungen*, Vieweg, 2005.
- [83] R. VERFÜRTH, *A Posteriori Error Estimation Techniques for Finite Element Methods*, Oxford University Press, 2013.
- [84] F. WEVER, A. ROSE, AND J. ORLICH, *Atlas zur Wärmebehandlung der Stähle*, vol. 1, Verlag Stahleisen, Düsseldorf, 1961.
- [85] E. WRONA, *Numerische Simulation des Erwärmungsprozesses für das induktive Randschichthärten komplexer Geometrien*, PhD thesis, Universität Hannover, 2005.
- [86] S. ZAGLMAYR, *High Order Finite Element Methods for Electromagnetic Field Computation*, PhD thesis, Johannes Kepler Universität, 2006.

- [87] M. X. ZHANG AND P. M. KELLY, *The morphology and formation mechanism of pearlite in steels*, *Materials Characterization*, 60 (2009), pp. 545–554.
- [88] O. C. ZIENKIEWICZ AND J. Z. ZHU, *A simple error estimator and adaptive procedure for practical engineering analysis*, *International Journal for Numerical Methods in Engineering*, 24 (1987), pp. 337–357.